BACHELORARBEIT

SEARCH FOR THE W′ BOSON IN THE LEPTON PLUS MISSING TRANSVERSE MOMENTUM CHANNEL USING THE CMS RUN-3 2022 DATASET AT $\sqrt{s}$ = 13.6 TeV

von

MIRAC NOYAN OEZDEMIR

vorgelegt der

FAKULTAET FUER MATHEMATIK, INFORMATIK UND NATURWISSENSCHAFTEN DER RWTH AACHEN UNIVERSITY

im Oktober 2023

angefertigt am

III. PHYSIKALISCHEN INSTITUT A

unter

INSTITUTSLEITER: Prof. Dr. rer. nat. Thomas Hebbeker

bei

ERSTGUTACHTERIN: Dr. rer. nat. Kerstin Hoepfner

ZWEITGUTACHTER: apl. Prof. Dr. rer. nat. Oliver Pooth

Abstract

This thesis presents the search for a new heavy vector boson in the lepton plus neutrino channel. The data is from the Run-3 2022 era F and G dataset from proton-proton collisions at a center-of-mass energy of 13.6 TeV, with an integrated luminosity of 20.7 fb^{-1}. The acquired data is compared to the Standard Model background, which has a similar signature to the decay of a possible W' boson. The focus in this thesis lies on the electron and muon channels. Neutrinos are not reconstructable using the CMS detector; thus, a quantity called missing transverse momentum is used for indirect reconstruction.

Furthermore, signal studies on the W' signal samples have been conducted. The signal efficiencies in the electron and muon channels are provided for the eras F and G in 2022, along with a study on the effects of the different coupling ratios of the SSM W' boson to the SM W boson at varying W' signal masses. At a low coupling ratio, the transverse mass distribution has a sharp on-shell Jacobian peak, with rising off-shell production at high masses or high coupling ratios. Also, the impact of the kinematic selection on the Standard Model background and signal distributions has been presented. The kinematic selection reduces the background contribution and improves the extraction of the signal in the high-mass region.

Using the transverse mass as the discriminating variable in this analysis, currently, no significant deviations in the low-energy region are observed.

Zusammenfassung

Diese Arbeit präsentiert die Suche nach einem neuen schweren Vektorboson im Endzustand mit einem Lepton und Neutrino. Die Daten stammen aus dem Jahr 2022 und wurden während des Run-3 in den Äras F und G gesammelt. Dabei handelt es sich um Proton-Proton-Kollisionen mit einer Schwerpunktsenergie von 13.6 TeV und einer integrierten Luminosität von 20.7 fb^{-1}. Die aufgezeichneten Daten werden mit dem Hintergrund des Standardmodells verglichen, der eine ähnliche Signatur aufweist wie der Zerfall des theoretischen W' Bosons. Diese Arbeit konzentriert sich auf den Elektron- und den Muon-Kanal. Die Neutrinos können nicht mit dem CMS-Detektor rekonstruiert werden, daher wird der fehlende Transversalimpuls als Hilfsgröße verwendet, um diese indirekt zu bestimmen.

Des Weiteren wurden Signalstudien mit den Signalsätzen des W'-Bosons durchgeführt. Die Signaleffizienz im Elektron- und Muon-Kanal für die Äras F und G im Jahr 2022 wurde berechnet, zusammen mit einer Untersuchung des Einflusses variabler Kopplungsstärken des SSM W'-Bosons im Vergleich zum SM W-Boson in Bezug auf verschiedene W'-Massen. Bei einem niedrigen Kopplungsverhältnis weist die transversale Massenverteilung einen scharfen Jacobi-Peak auf der Massenschale auf, wobei die Produktion außerhalb der Massenschale bei hohen Massen oder hohen Kopplungsverhältnissen ansteigt. Zusätzlich wurde der Einfluss der kinematischen Selektion auf den Standardmodellhintergrund und die Signalverteilungen untersucht. Die kinematische Selektion reduziert den Standardmodellhintergrund und verbessert die Signalextraktion in der Region mit hohen Energien.

Unter Verwendung der transversalen Masse als diskriminierende Variable, sind derzeit keine signifikanten Abweichungen in der Niedrigenergie-Region erkennbar.

Contents

1 Introduction

In the dynamic and ever-evolving domain of particle physics, the pursuit of knowledge takes one to the very fabric of the universe. The current Standard Model (SM) has proven remarkably successful in explaining three fundamental forces: electromagnetism, the weak nuclear force, and the strong nuclear force. Its precision and predictive power have allowed it to account for a wide range of observed phenomena. However, the SM, while a powerful framework, is not without its limitations. Technological advancements have enabled the investigation of fundamental matter constituents with unprecedented precision. These technological leaps have uncovered intriguing hints of physics beyond the boundaries of the Standard Model. A notable example is the phenomenon of neutrino oscillations [1], which challenges established SM principles. As a result, these discoveries have spurred the development of theoretical frameworks that extend beyond the boundaries of the Standard Model. Testing these theories Beyond the Standard Model (BSM) is a way of discovering new physics.

As the Large Hadron Collider (LHC) at CERN entered its Run-3 phase in 2022, operating at a unprecedented center-of-mass energy of 13.6 TeV and accompanied by an integrated luminosity of 20.7 fb^{-1} for the eras F and G [2], a unique opportunity arose to investigate the nature of the W′ boson and its significance in advancing the understanding of the subatomic world. The W′ boson is a counterpart to the well-known SM W boson [3, 4, 5, 6]. The search for the W′ boson is important, because it tests the SM for completeness in high-mass resonances. The acquired experimental data is compared to the expectations in order to find deviations from the SM predictions. The main topic of this thesis is to study the decay of the W′ boson into a muon and neutrino or an electron and neutrino, using the acquired data from the Compact Muon Solenoid (CMS) experiment at the LHC and different signal selection criteria.

In sec. 2 the theory behind this study is explained by introducing the standard model of particle physics and the Sequential Standard Model (SSM). A solid grasp of these models is crucial as it lays the necessary foundation for the analyses undertaken in this thesis. The specifications of the CMS experiment and the detector components are presented in sec. 3. In the following sec. 4, the used data and simulated samples for this thesis are shown. The key concepts of the strategy that are employed to perform the data to background comparison are described in sec. 5. In sec. 6 the impact of different coupling ratios on the signal of the W′ boson is investigated, followed by the resulting distributions shown in sec. 7.

2 Theory and physics models

This section serves as a short introduction to the domain of elementary particles, that is necessary for understanding the analysis procedure given in the next sections. The Standard Model (SM) and the Sequential Standard Model (SSM), which serves as an extension of the Standard Model by adding new heavy gauge bosons, the W' and Z', are introduced. This section alone does not cover the topic in great detail, but it offers a short overview of the groundwork for this thesis. The couplings for these bosons are mainly assumed to be SM-like with their masses being the only free parameter [7]. The particle properties mentioned in this section are mainly taken from [8, 9].
This thesis uses natural units ($\hbar = c = 1$) and charges are expressed in terms of the elementary charge e. That means that energy, momenta and masses are given in eV (electron volts), with $1\,\mathrm{eV} = 1.602 \times 10^{-19}\,\mathrm{J}$.

2.1 The Standard Model

	generation (for leptons/quarks) interaction (for bosons)	symbol	name	mass	charge
leptons	1	e^-	electron	0.511 MeV	-1
		ν_e	electron neutrino	< 1.1 eV	0
	2	μ^-	muon	105.66 MeV	-1
		ν_μ	muon neutrino	< 0.19 MeV	0
	3	τ^-	tau	1776.86 MeV	-1
		ν_τ	tau neutrino	< 18.2 MeV	0
quarks	1	u	up	2.16 MeV	+2/3
		d	down	4.67 MeV	-1/3
	2	c	charm	1.27 GeV	+2/3
		s	strange	93.4 MeV	-1/3
	3	t	top	172.69 GeV	+2/3
		b	bottom	4.18 GeV	-1/3
bosons	electromagnetic	γ	photon	$< 1 \times 10^{-18}$ eV	0
	weak	Z^0	Z	91.19 GeV	0
		$W^\pm$	W	80.38 GeV	± 1
	strong	g	gluon	0	0

Table 2.1: The properties of each elementary particle, except the Higgs boson, are shown in this table.

The Standard Model of particle physics is currently the most precise description of the elementary particles. It describes 3 out of 4 fundamental forces in the universe (weak, electromagnetic, strong). Each force is mediated by an exchange particle, and the leptons and quarks can only interact with other particles using these exchange particles that carry the forces. The fourth fundamental force is gravity, for which, unlike the other forces, no mediating particle has been found yet. According to Einstein's theory of relativity, gravity is not a typical force, but more a geometric theory, and therefore, a property of space-time itself [10].
The elementary particles are stratified into two fundamental categories: fermions, characterized

by their half-integer intrinsic angular momentum, the spin, and bosons, distinguished by their integer spins. The table 2.1 lists some of the properties of the SM particles that are currently known.

2.1.1 Matter particles

The fermions are further divided into leptons and quarks with each being further subdivided into three generations. The former are participants in the electromagnetic and weak interactions, while the latter participate in the strong, electromagnetic, and weak forces. The lepton neutrinos only interact using the weak nuclear force because of their neutral charge, in contrast to the electron, the muon, and the talon, which, due to their charge, also participate in the electromagnetic interaction.
The particle masses increase with each generation. The only stable generation is the first. Every other particle decays either into a neutrino, an electron, or up and down quarks.
The first generation of quarks consists of up and down quarks, the second generation of charm and strange quarks, and the third generation of top and bottom quarks. The 6 SM quarks can also be further divided by charge: 3 have a charge of $+\frac{2}{3}$, and the remaining 3 have a charge of $-\frac{1}{3}$.
For the leptons, there is a similar arrangement. Each generation consists of a lepton with its corresponding neutrino. The 6 leptons can be divided into groups of 3, taking into account that the 3 lepton neutrinos have no charge, while their corresponding particles have a charge of -1.
In the SM, each particle also has an antiparticle with the same properties except for an opposite charge. For example, an electron's antiparticle is an anti-electron, or positron, with the same mass and spin but with a charge of $+1$.

2.1.2 Interactions

The bosons, often denoted as mediators or carriers of the fundamental forces, include the photon, which carries the electromagnetic force, the $W^{\pm}$ and Z^0 bosons, the intermediaries of the weak force, and the gluons, mediators of the strong nuclear force. The weak force mediators can change particle identities. An example of this is the β^- decay of a neutron into a proton under the emission of an electron and electron antineutrino. All force mediators have spin 1 and are therefore called vector bosons.
Moreover, the discovery of the Higgs boson in 2012 [11] paved the path to unraveling the mechanism by which particles acquire their masses. The Higgs boson has a mass of 125.25 GeV, a spin and charge of 0, and is consequently called a scalar boson.

2.2 The Sequential Standard Model

Even though the standard model seems complete, anomalies emerge from the experimental results. The standard model predicts massless neutrinos, yet neutrino oscillations have been observed from solar neutrinos [1]. This indicates that neutrinos do indeed have a non-zero mass. Also, gravity is not included in the Standard Model, which implies that it is incomplete. Therefore, the Sequential Standard Model was developed as a guiding framework for the exploration of new particles that lie beyond the purview of the SM. The SSM unveils the W' boson, a particle similar to the W boson but with a higher mass [12]. The Feynman graph of the production and decay of the W' is shown in fig. 2.1.

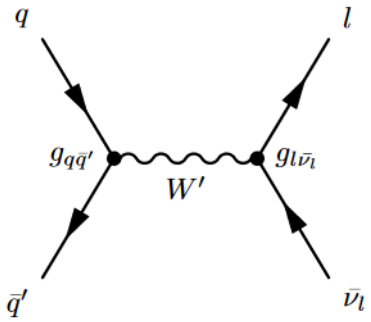

Figure 2.1: Feynman graph of the production and decay in the lepton channel. One can interchange the incoming and outgoing particles with their corresponding antiparticles, but one also must interchange the direction of the arrows.

Given its higher mass compared to the W boson, it is mainly produced off-shell, with a Jacobian peak at the mass of the W′ boson. The production via the $t\bar{b}$ channel is also allowed, due to the higher mass, in contrast to the W boson production, which results in a branching fraction of 8.5% for each one of the leptonic channels. The leptonic channels consist of the final state with a lepton (electron, muon, tau) and a corresponding lepton antineutrino. The hadronic decay modes are based on the Cabibbo–Kobayashi–Maskawa matrix [13]. The final states consist of a quark with charge $\frac{2}{3}$ and an anti-quark with charge $\frac{1}{3}$, where the both quarks can be exchanged with their corresponding antiparticles.

2.2.1 Varying the coupling strength

The W′ boson's coupling strength is usually assumed to be SM-like [7], but it can also be varied. The different couplings for the W′ boson are considered in a quantity called the coupling ratio, $g_{W'}/g_W$, which relates the W′ coupling to the W boson's coupling. Depending on the ratio the signal shape, the peak width and the amount of off-shell produced W′ bosons, will change. This happens, because a process with the W′ boson will, be less or more likely for lower or higher coupling ratios compared to a W boson, due to its dependence on coupling ratio. The transition matrix element, which is a factor determining the probability of a process, is proportional to the square of the coupling when calculating it. This holds also when computing the decay width.

3 CMS Experiment

The beginning of this section introduces the Large Hadron Collider (LHC), followed by a description of the CMS detector. The upgrades made to the CMS detector for Run-3 are also highlighted. This is followed by a summary of the data acquisition process and the reconstruction of physics objects using the CMS Particle-Flow algorithm.

3.1 The Large Hadron Collider

The CMS experiment is located at CERN, a research institute near Geneva, at the border of France and Switzerland. The CMS detector is one of the four main experiments of the LHC, currently the largest particle accelerator, with a circumference of 26.7 km. The main characteristic of a particle accelerator is the center-of-mass energy. For symmetric, circular colliders, like the LHC, the center-of-mass energy is given by $\sqrt{s} = 2E_{beam}$. The $\sqrt{s}$ for the LHC Run-3 is 13.6 TeV. The primary colliding particles are protons, but heavy ion collisions also take place for approximately one month a year with a lower center-of-mass energy. The acceleration and focusing of the beam are achieved by superconducting dipole and quadrupole magnets inside an ultra-high vacuum (UHV).

Previously, the main accelerator was the Large Electron-Positron Collider (LEP), which operated from 1989 to 2000. It was dismantled around 2001 to make space for building the LHC, which re-used the LEP tunnel. A main advantage of the LHC is that, in contrast to LEP, less energy is lost due to bremsstrahlung. Given two particles having the same velocity, the ratio between their energy loss due to bremsstrahlung in a synchrotron is proportional to m^{-4}. This means that for protons, the energy loss due to bremsstrahlung is less by a factor of $\left(\frac{m_p}{m_e}\right)^4 \approx 10^{13}$.

The LHC has a chain of particle accelerators that are utilized as pre-accelerators to increase the particle energies before being injected into the main accelerator. Examples include the linear particle accelerator, Linac4, which creates hydrogen ions H^- with an energy of 160 MeV; the Proton Synchrotron Booster (PSB), which strips two electrons, leaving only the proton; the Proton Synchrotron (PS), where the protons are accelerated to 26 GeV; and finally, the Super Proton Synchrotron (SPS). After reaching an energy of 450 GeV in the SPS, the protons are injected into the main accelerator, and the energy of each beam is increased to 6.8 TeV. The colliding proton bunches are then detected at four detectors: ATLAS (A Toroidal LHC Apparatus), LHCb (LHC-beauty), ALICE (A Large Ion Collider Experiment), and CMS (Compact Muon Solenoid). The accelerator complex is shown in fig. 3.1.

The instantaneous luminosity is the number of detected events per unit time and area. High luminosity accelerators can acquire more events resulting in more statistics in analyses. The instantaneous luminosity can be calculated using this formula for all collisions at a circular accelerator

$$L = \frac{N_1 N_2 N_b f}{4\pi\sigma_x\sigma_y}. \tag{3.1}$$

Here N_1 and N_2 are the number of particles that are in a bunch, N_b is the number of bunches f is the frequency of the bunch crossings and $\sigma_{x/y}$ are the transverse spread of the bunches, where one usually assumes a gaussian shape. The new upgrade to a center-of-mass energy of 13.6 TeV allows the LHC to continuously run on an instantaneous luminosity of $L = 2 \times 10^{34}\,\mathrm{cm}^{-2}\,\mathrm{s}^{-1}$ [16]. Integrating this over the run-time gives the integrated luminosity, which, for Run-3 2022 era F and G, lies at 20.7 fb^{-1}. The total cumulative luminosity for Run-3 is shown in fig. 3.2.

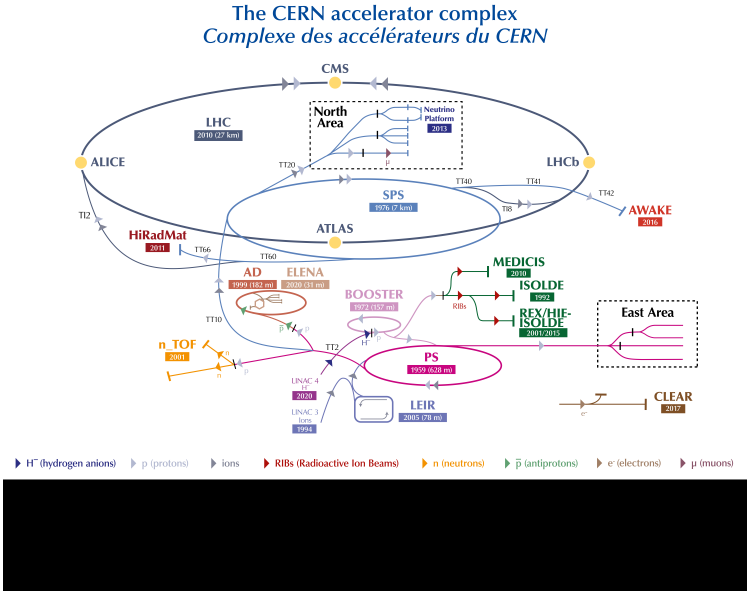

Figure 3.1: Overview of the LHC complex. The initial year of operation for the detectors and accelerators with the circumferences are also given [14].

3.2 CMS detector

CMS is a general-purpose detector, capable of reconstructing many particles except for neutrinos. It has cylindrical structure and weighs over 14,000 tons. Its height is 15 m, and its length is 28.7 m. As the name suggests, it is especially accurate at detecting muons. The solenoid magnetic field has a strength of 3.8 T. It consists of a barrel and an endcap region to detect particles at high velocities that have a steep angle relative to the beam axis after collision. It has an onion-like structure with multiple layers. From the inside out, there are the silicon trackers, the crystal electromagnetic calorimeter (ECAL), the hadron calorimeter (HCAL), the superconducting solenoid, and the muon chambers with the steel return yokes. The apparatus is shown in fig. 3.3. The z-axis goes along the shaft, while the y-axis direction points vertically upwards, and the x-axis points radially to the center of the LHC.

Given its cylindrical symmetry, one can define the pseudorapidity η as $-\ln\left[\tan\left(\frac{\theta}{2}\right)\right]$. This quantity is Lorentz-invariant and provides a measure of velocity. Higher η values correspond to higher velocities, indicating a steeper angle between the particle's trajectory and the beam axis.

To measure the angular separation between two particles in the $\eta - \phi$ plane, a cone radius R is defined as $\Delta R = \sqrt{(\Delta\phi)^2 + (\Delta\eta)^2}$, where $\Delta\eta$ is the difference in pseudorapidity for two particles, and $\Delta\phi$ is their difference in azimuth angle.

Another important quantity is the transverse mass M_T, which, for a two-body decay into a lepton and neutrino, is defined as:

$$M_T = \sqrt{2p_T^l p_T^\nu \left(1 - \cos\left[\Delta\phi\left(l, \nu\right)\right]\right)}. \tag{3.2}$$

Here, p_T is the transverse momentum in the x-y-plane, and $\Delta\phi$ is, as mentioned earlier, the difference in azimuth angle. Neutrinos, due to their interaction using only the weak force, are almost always undetected. Therefore, a new quantity called MET, missing E_T, was introduced. It calculates the undetected amount of transverse energy and azimuth angle by summing up the

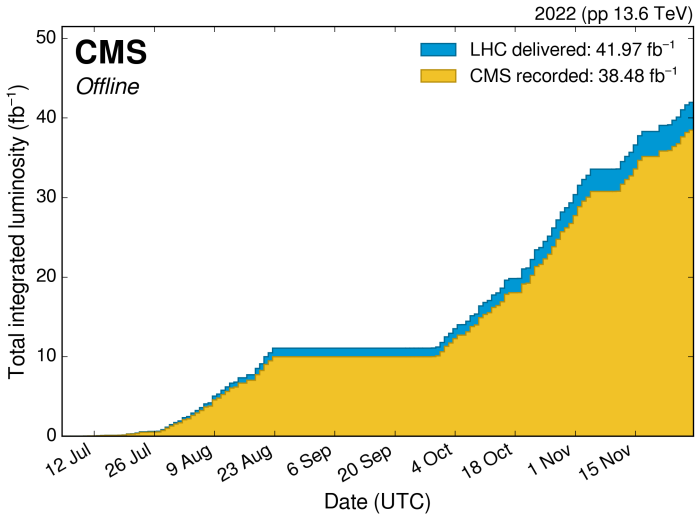

Figure 3.2: Total integrated luminosity for the year 2022 of Run-3 per day [15].

negative momentum vectors of all particles in an event. In this context, momentum and energy are used interchangeably due to the high center-of-mass energy.

3.3 Layers of the CMS detector

The information for this section about the composition of the CMS detector is primarily sourced from [18], with additional details regarding the Run-3 upgrades obtained from [19].

3.3.1 Tracker System

The silicon tracker system is used in the precise measurement of particle trajectories and also primary and secondary vertex reconstruction. The tracker consists of several layers of silicon detectors, including the pixel detector and the silicon strip tracker. The pixel detector is made up of 100 x150 µm^2 modules, which in total comprise approximately 66 million channels. The silicon strips have a size of 80 x180 µm^2, which roughly equals 9.6 million channels.
For Run-3, upgrades have been implemented in the tracker system to improve its performance. One upgrade is the installation of the Phase-2 Pixel Detector, which features an additional inner layer for improved tracking and vertexing capabilities. Also, due to radiation aging, the innermost tracker layer was replaced. These upgrades enhance the ability of the CMS detector to precisely measure the trajectories of charged particles.

3.3.2 Electromagnetic Calorimeter (ECAL)

The ECAL is designed to measure the energy of particles that participate in the electromagnetic interaction produced in particle collisions. It is composed of around 76.000 lead tungstate crystals, which produce scintillation light when particles deposit energy within them. Lead tungstate has high density and is radiation-resistant while still being finely granulated. The scintillation light is detected by silicon avalanche photodiodes (APDs) in the barrel and by vacuum phototriodes (VPTs) in the endcap region. This is then used to measure the energy of the incident

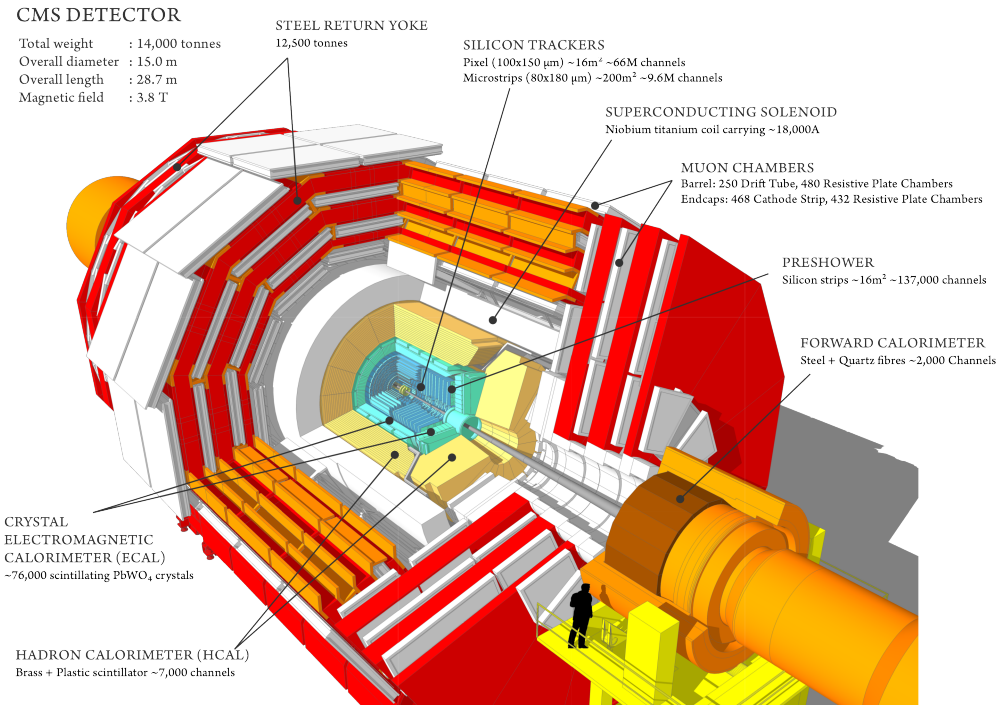

Figure 3.3: View of the CMS detector. The beam axis (or z-axis) is the is aligned with the pipe and the interaction point of the bunches is highlighted with a yellow point at the detector center [17].

particles. For instance, the electrons are detected in the ECAL.

3.3.3 Hadronic Calorimeter (HCAL)

The HCAL is responsible for measuring the energy of hadrons, which are particles composed of quarks, as well as other particles that interact via the strong nuclear force. The HCAL uses brass and plastic scintillator materials to absorb the energy of these particles and convert it into detectable signals. Like in the ECAL, diodes are used to detect the scintillation light. It can measure particles up to $|\eta| < 5$, thanks to a barrel HCAL (HB), an endcap HCAL (HE), and a forward HCAL (HF).
In the HCAL, the old hybrid photodiodes (HPDs) were replaced with silicon photomultipliers (SiPMs), which have a higher photon detection efficiency, insensitivity to magnetic fields, and better radiation tolerance. Also, the readout electronics were upgraded to have finer granularity and higher data quality.

3.3.4 Superconducting Solenoid Magnet

The superconducting solenoid magnet is one of the most distinctive features of the CMS detector. It creates a magnetic field that allows the detector to precisely measure the momenta of charged particles along with the charge of the particle. The magnet consists of superconducting niobium-titanium coils and produces a field strength of about 3.8 T. Also, the steel return yokes ensure that almost only the muons reach the muon chambers because only muons and neutrinos can pass through the yokes.

3.3.5 Muon System

The Muon System is the outermost component of the CMS detector, and it is designed to identify and measure muons. Muons are penetrating particles that can traverse other detector parts, like the two calorimeters and the steel return yokes. In the barrel, drift tubes (DT) and resistive plate chambers (RPCs) are used for muon detection, whereas in the endcap region, cathode strip chambers (CSCs), also together with RPCs, are used.
In preparation for Run-3, the CMS muon system has received upgrades to improve its performance. This includes the installation of new gas electron multiplier (GEM) detectors in the forward region and improvements in the trigger and readout systems.

3.3.6 Data acquisition

A two-tier trigger system is used in the CMS experiment for data-taking. The first tier (L1) consists of custom hardware processors that use the information from the calorimeters and muon detectors to select events with a fixed latency of 4 µs [20, 21, 22]. The second tier (HLTs) is composed of a processor farm that runs a version of the full event reconstruction software, optimized for fast processing. However, due to the large number of bunch crossings every 25 ns, an effect called pileup lowers the ability to store the data provided by the detector. There is an average number of approximately 46 collision bunches per crossing [15], which reduces the efficiency of primary vertex reconstruction and time resolution. The L1 rate of accepting events has been close to 100 kHz, and the HLTs rate of accepting events has been around 1 kHz.

3.3.7 Reconstruction of Physics Objects in CMS

For offline event reconstruction and the identification of physics objects, the CMS Particle-Flow (PF) algorithm was developed [23, 24]. It utilizes information from all parts of the detector to properly reconstruct events with a low misidentification rate. It works in three steps. First, the information from all detector components is analyzed independently. In the second step, the information is combined, and in the third step, the results are interpreted to allow for pileup mitigation and to quantify the momenta and angles of the reconstructed particles.
The primary vertex of the pp interaction is defined as the vertex with the largest reconstructed p_T^2 value of all physics objects. The energy of electrons is reconstructed by combining primary vertex information from the tracker, compatible energy from the ECAL cluster, and the corresponding sum of the energy of all bremsstrahlung photons that are consistent with the electron track. The photon energies are acquired from the ECAL measurement. The energies from neutral hadrons are determined by combining the ECAL and HCAL measurements. The energy of charged hadrons is obtained by combining the momentum measurement of the tracker with suitable ECAL and HCAL deposits, which are response function corrected for the hadronic showers from the calorimeters. Finally, muon energies are measured by obtaining the curvature of the track in the magnetic field. The charge of a particle can also be measured by the curvature of the track, depending on whether the particle curves to the "left" or the "right".
The most final states in particle collisions are jets. They are narrow cones that contain multiple hadrons and other particles that result from the hadronization of a gluon or a quark. When a top quark decays into a bottom quark, it emits a W boson which can further decay into a muon or an electron. This final state can be reconstructed as a W′ event, as it has the same signature. Therefore the jets can be further subdivided according to their contents. For example, a so-called "b-jet" is a jet that originates from a b-quark.

4 Data and background samples

This section introduces the data hierarchy at CMS and presents the data and simulated samples used for this analysis.

4.1 Data hierarchy

The data recorded by the CMS detector is organized into a hierarchy of formats. Each format contains the same set of events but with varying levels of information. The format that contains the raw, unprocessed data directly from the detector is called the RAW format [25, 26]. The RECO format, on the other hand, contains data in which physics objects like muons or electrons have already been reconstructed. However, it is typically not used for most analyses due to its large event size, of the order of megabytes per event. The AOD (Analysis Object Data) format [27] is a refined version of the RECO format, with a reduced event size, typically of the order of hundreds of kilobytes per event. Further filtering of the AOD format results in miniAOD samples, which have an even smaller event size, typically on the order of tens of kilobytes per event [28]. For this analysis, nanoAOD samples were used, which currently have the smallest event size, typically of the order of kilobytes per event, making them suitable for data analysis [29].

4.2 Data samples

The analysis described in this thesis is based on a partial dataset from 2022. The CMS data is typically organized into eras, for example, to account for updated detector conditions [30]. This simplifies the management of large datasets. The ReReco for the eras A to E is currently ongoing, to account for the aforementioned detector conditions. Additionally, in early September 2022, a water leakage issue resulted in the discovery of a hole in the positive side of the ECAL endcap (EE+), leading to the deactivation of approximately 7% of the EE+ [31]. Therefore, the 2022 dataset has further been divided into two distinct periods: pre-EE and post-EE, where post-EE encompasses the eras E, F and G, referring to the time after the occurrence of the ECAL endcap water leakage incident. This analysis specifically uses the eras F and G, following the recommendation from the Physics Performance Data (PPD) group.

Era	**Run Range**	**Integrated Luminosity in** fb^{-1}
F	360332-362180	17.6
G	362350-362760	3.1
		= 20.7

Table 4.1: The luminosity and run range for each era is shown in this table. Taken from [30].

Lepton	DAS path
Electron	/EGamma/Run2022X-PromptNanoAODv11_v1-v2/NANOAOD
Muon	/Muon/Run2022X-PromptNanoAODv11_v1-v2/NANOAOD

Table 4.2: The DAS dataset paths for the electron and muon channel are shown in this tabular [32]. The X stands for the era (F or G).

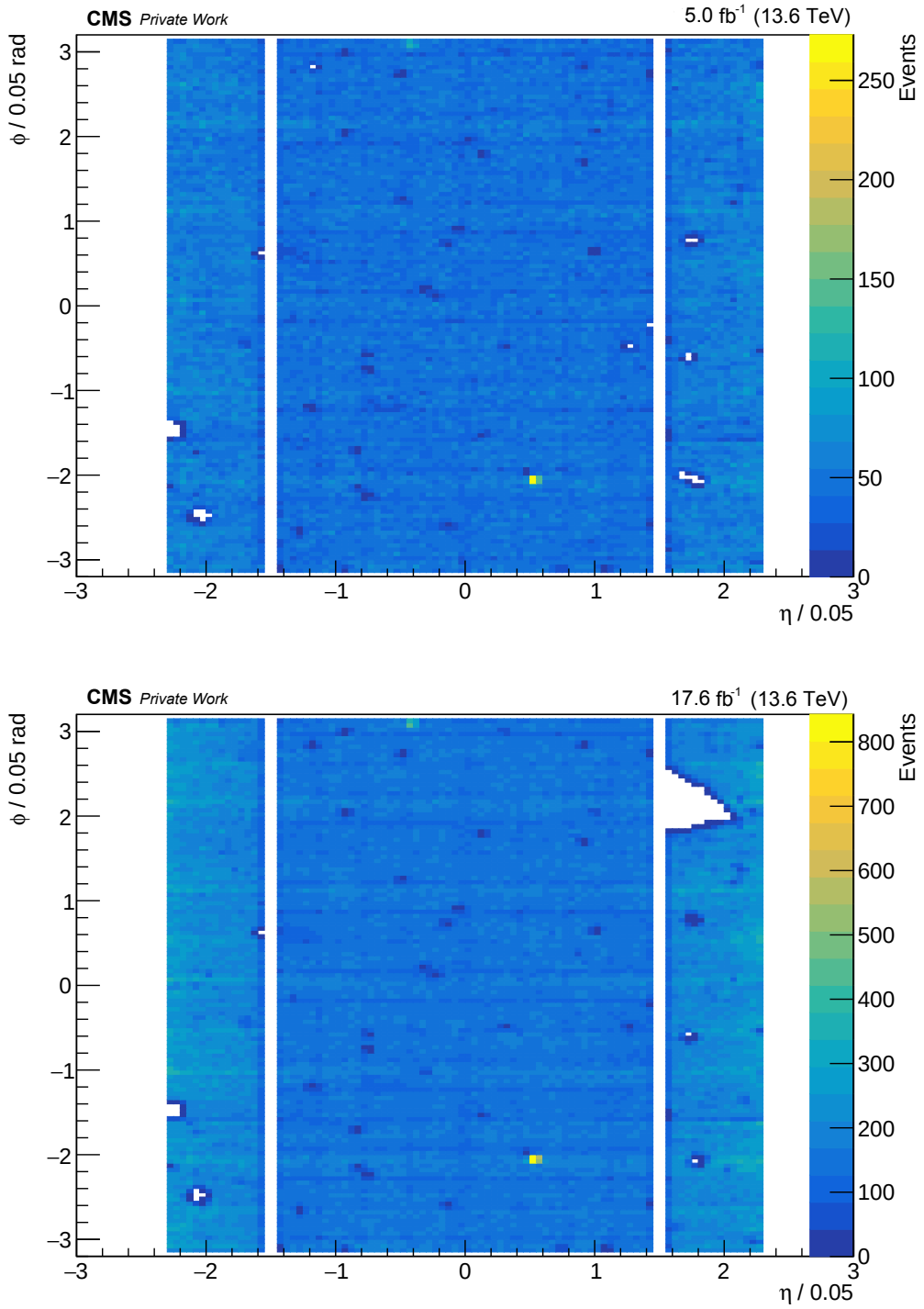

Figure 4.1: In this figure is the $\eta - \phi-$ plane for era C (top) and era F (bottom) shown. The hole can be seen in the era F for positive η and ϕ. The other holes that are also present in both plots are known and are not a consequence of the leakage. The distribution is shown after applying the preselection, that is introduced in sec. 5.

The location of the EE+ hole is approximately around $\eta = 2$ and $\phi = 2$, which can be seen in fig. 4.1. For comparison reasons, the sample plot from era C (pre-EE) is also provided.

The dataset paths for the CMS Data Aggregation System (DAS) are given in the table 4.2. CMS stores files that define which luminosity sections, in which runs, are considered of 'good quality' and should be processed for data analysis in a JSON format. The Golden JSON file used to analyze the 2022 data can be found here [33, 34, 35]. It filters events that are not certified. The run ranges and integrated luminosities for the eras F and G are given in table 4.1.

4.3 Simulated samples

In order to search for new physics is the recorded data is compared to simulated Monte Carlo (MC) samples of SM processes. This involves utilizing processes with identical final states or those that may be mistaken for them as background due to misreconstruction. Simulated samples contain information at two levels. The first is the generator (GEN) level, which provides details about particle's properties without reconstruction effects. The second is the reconstructed (reco) level, where GEN-level particles have been processed using Geant4 [36], to simulate realistic detector response. These samples may differ in terms of event numbers or cross-sections. A higher cross-section indicates that a process is more likely to occur for a given luminosity. The MC samples are normalized to an integrated luminosity of $1\,\mathrm{pb}^{-1}$. To achieve this, the MC samples are reweighted by a factor of

$$w = \frac{\sigma \cdot \mathcal{L}}{N_{MC}}, \tag{4.1}$$

where $\mathcal{L}$ represents the luminosity of the data, and N_{MC} is the total number of events in an MC sample.
The MC samples are generated using different generators. This analysis used samples that are generated with various MC generators: Pythia8 [37], aMC@NLOFXFX [38], POWHEG [39, 40], and MadGraph [41]. These samples originate from different perturbation orders, encompassing leading order (LO), next-to-leading order (NLO), and next-to-next-to-leading order (NNLO).
To adapt cross sections between different accuracy orders, a k-factor is employed. The k-factor is defined as the ratio of a higher-order cross section to a lower-order cross section ((N)NLO to (N)LO), denoted as

$$k = \frac{\sigma_{(N)NLO}}{\sigma_{(N)LO}}. \tag{4.2}$$

It is worth noting that k-factors can also be mass or energy binned, implying different k-factors for various masses or energies. However, no k-factors for the samples are applied, since they are not available yet.
Additionally, some MC samples can be categorized into binned and bulk samples. Binned samples are divided into bins based on a certain quantity, such as the generator-level mass, invariant mass of two particles, or transverse momentum. On the other hand, bulk samples are not binned and are inclusive, encompassing processes for all three lepton flavors.

4.3.1 Background samples

In this section, the used background samples in this analysis are presented. All samples have the CP5 tune [42] and have been produced with the NNPDF31_nnlo_as_0118 PDF set in Run-3 [43]. Details regarding the cross sections for each process and the specific binnings can be found in the Appendix, in the table A.1. The number of events in each background sample can be found in [44].

W boson: The most dominant background is the SM $W \to l + \nu$, where $l = e, \mu, \tau$, because this decay has the same signature as the W' boson decay. The samples are binned in W-mass and generated with Pythia8 at LO.

Top Quark: This inclusive background has the second highest contribution to the total background. It models the dileptonic decay of $t\bar{t} \to 2l + 2\nu$. This final state can be reconstructed as a $l + \vec{p}_T^{miss}$ final state when both neutrinos and the second lepton are undetected. It is generated using PowHeg and Pythia8 at NLO and is not binned; therefore, it is a bulk sample.

Diboson: Inclusive WW, WZ or ZZ bulk samples are generated using Pythia8 at LO. Also an exclusive $ZZ \to 2l + 2\nu$ sample is generated using PowHeg and Pythia8 at NLO. Here, the W and Z bosons can decay into a lepton with a neutrino and jets which results into a similar final state as just lepton+neutrino. Another possible final state originates from the $WZ \to l + \nu + 2\nu$ process, which can be reconstructed as a $l + \nu$ final state with the remaining two neutrinos being undetected.

QCD: This is the most dominant process at the LHC. The quantum chromodynamics (QCD) jets can be misidentified as leptons, at low transverse momentum, and even if jets behave differently than leptons, due to the high cross section of this process some events are misreconstructed. The samples are binned in p_T and generated using Pythia8 at LO.

Drell-Yan ($Z/\gamma \to ll$): The decay products of the DY process are two electrons or muons. These samples are binned in mass of the invariant dilepton mass and generated at NLO using PowHeg and Pythia8. In addition to binned samples, an inclusive DY process with a final state consisting of two leptons and two jets is included. One of the leptons can be undetected and therefore, be misreconstructed as a neutrino, which would result in the $l + \vec{p}_T^{miss}$ final state.

4.3.2 Signal samples

SSM W' signal samples were generated for the both electron and the muon channel. These samples specifically contain the W' decay and are generated at the leading order using Pythia8. In the table 4.3 is a list for Run-2 and Run-3 signal samples. To account for NNLO corrections, the default PDF set NNPDF31_nnlo_as_0118_mc_hessian_pdfas [45] was used to calculate a k-factor utilizing FEWZ [46, 47]. This k-factor was then applied to the cross sections. The cross section of the samples are given in table 4.3. Each signal sample contains approximately 37 000 events.
The primary discriminating variable in this analysis is the transverse mass, denoted as M_T, which was introduced in the previous section. It has been found that the transverse mass distribution provides the cleanest signature, exhibiting a Jacobian peak in the tail of the off-shell spectrum (see fig. 4.2) [48]. This peak corresponds to the mass of the W' signal sample. High-mass samples have a suppressed on-shell production. Consequently, these samples contain a higher number of off-shell produced W' bosons. The decay of the W' boson in both the electron and muon channels follows a two-body decay with back-to-back kinematics in the center-of-mass frame. Due to the high mass of the W' boson, one also expects back-to-back kinematics in the laboratory frame, combined with a p_T / p_T^{miss} ratio of roughly 1. Additionally, the distribution is isotropic in the ϕ- and ϕ^{miss}-plane and features a slight peak centered around 0 in the η-distribution.

Non-SSM coupling samples were also produced, covering coupling ratios of 0.01, 0.1, 1.0, 2.0, 3.0, and 5, utilizing Madgraph and Pythia8. The coupling ratio in the decay vertex determines the amount of on- or off-shell produced W' bosons.

Table 4.3: Cross sections at LO and NNLO with the corresponding k-factor for the W' boson at different signal sample masses at $\sqrt{s} = 13\,\text{TeV}$ and $\sqrt{s} = 13.6\,\text{TeV}$. Taken from [46] and [49].

Run	$M_{W'}$ [GeV]	σ_{LO} [pb]	σ_{NNLO} [pb]	k-factor	Generator
Run-2	200	975.057	1118.70	1.1473	pythia
	400	94.72416	109.46380	1.1556	pythia
	600	21.89561	25.82947	1.1797	pythia
	800	7.27776	8.73379	1.2001	pythia
	1000	2.95282	3.59797	1.2185	pythia
	1200	1.35782	1.66306	1.2248	pythia
	1400	0.68	0.84114	1.2370	pythia
	1600	0.36218	0.452153	1.2484	pythia
	1800	0.20204	0.2544	1.2592	pythia
	2000	0.11681	0.149093	1.2764	pythia
	2200	0.06951	0.0888327	1.2780	pythia
	2400	0.04237	0.054461	1.2854	pythia
	2600	0.02637	0.0340433	1.2910	pythia
	2800	0.01673	0.0216548	1.2944	pythia
	3000	0.01081	0.0141527	1.3092	pythia
	3200	0.00712	0.00920079	1.2923	pythia
	3400	0.00478	0.00614738	1.2861	pythia
	3600	0.00327	0.00418057	1.2785	pythia
	3800	0.0023	0.00289792	1.2600	pythia
	4000	0.00164	0.0020971	1.2787	pythia
	4200	0.0012	0.00148246	1.2354	pythia
	4400	0.0009	0.00109604	1.2178	pythia
	4600	0.0007	0.000828743	1.1839	pythia
	4800	0.00055	0.000640294	1.1642	pythia
	5000	0.00044	0.000523933	1.1908	pythia
	5200	0.00035	0.000405361	1.1582	pythia
	5400	0.00029	0.000330796	1.1407	pythia
	5600	0.00024	0.000273824	1.1410	pythia
	5800	0.00020	0.000229364	1.1468	pythia
	6000	0.00018	0.000203436	1.1302	pythia
Run-3	200	960.2319	1106.384	1.189900	madgraph-pythia
	400	98.66777	115.9101	1.222662	madgraph-pythia
	600	23.66002	28.20430	1.246987	madgraph-pythia
	1000	3.369363	4.112692	1.289603	madgraph-pythia
	1600	0.441491	0.555177	1.350808	madgraph-pythia
	2000	0.148275	0.189790	1.391784	madgraph-pythia
	2600	0.035468	0.046407	1.449781	madgraph-pythia
	3000	0.015056	0.019882	1.480140	madgraph-pythia
	3600	0.004737	0.006262	1.499118	madgraph-pythia

Table 4.3 – Continued

Run	$M_{W'}$ [GeV]	σ_{LO} [pb]	σ_{NNLO} [pb]	k-factor	Generator
Run-3	4000	0.002402	0.003148	1.488228	madgraph-pythia
	4600	0.001006	0.001289	1.443194	madgraph-pythia
	5000	0.000618	0.000779	1.407399	madgraph-pythia
	5600	0.000332	0.000411	1.363941	madgraph-pythia
	6000	0.000232	0.000284	1.344642	madgraph-pythia
	6600	0.000143	0.000174	1.324484	madgraph-pythia

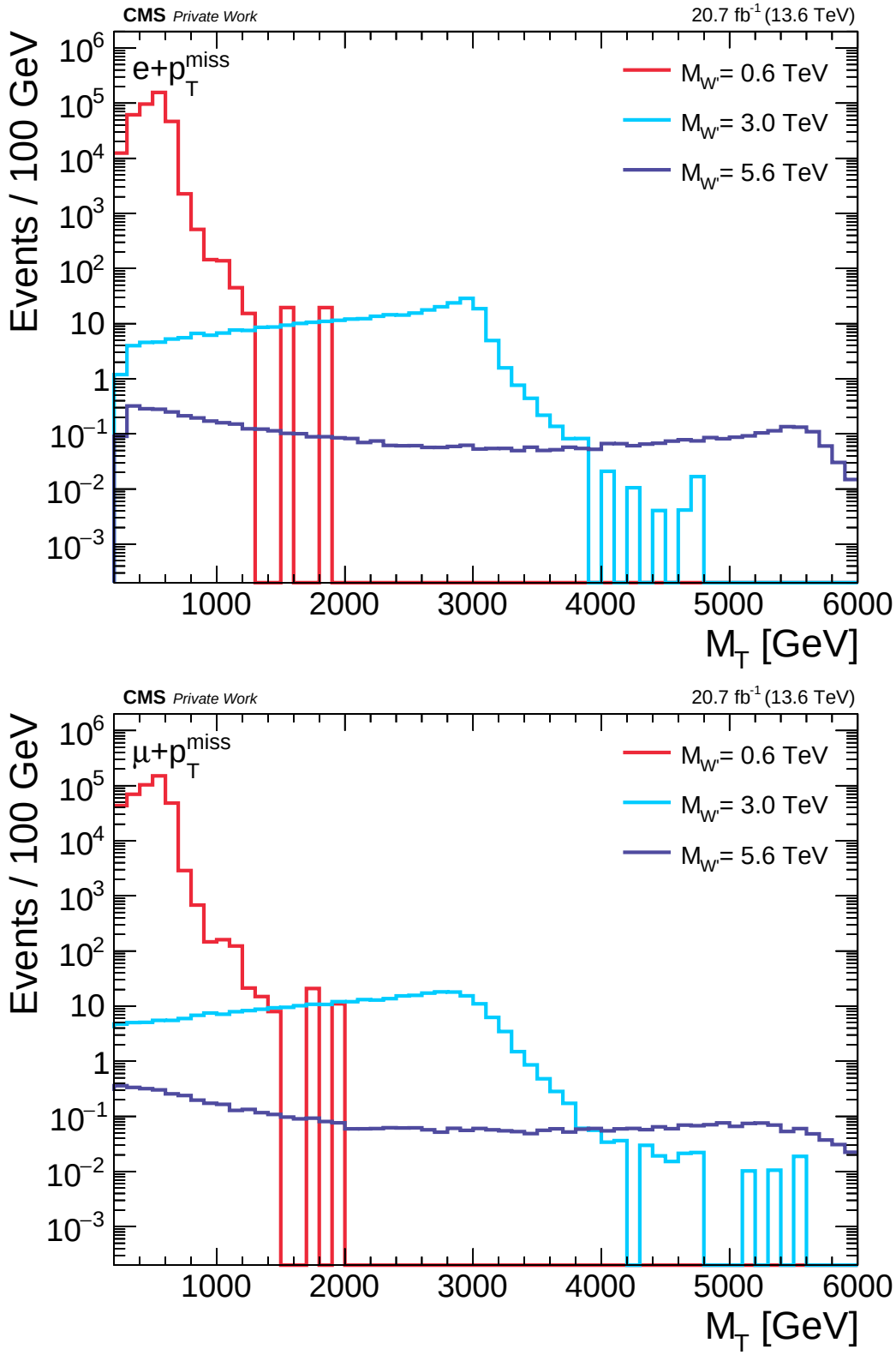

Figure 4.2: Reconstructed transverse mass distributions for a W′ boson decay in the electron channel (top) and in the muon channel (bottom). The signal samples have a W′ mass of 600 GeV, 3000 GeV and 5600 GeV. It is visible that for low-mass samples there is a sharp Jacobian peak with a tendency for rising off-shell for higher mass samples. The peak in the electron channel is sharper, because the ECAL has a better energy resolution for higher energies than the muon chambers' momentum resolution. This results in a sharper p_T distributions in the electron channel.

5 Event selection and reconstruction

In this section, the selection criteria for event reconstruction and event filtering are introduced, and the reasoning behind the cuts used in the analysis is presented. The Run-3 analysis strategy mainly follows Run-2 [49]. An additional requirement that the event must contain at least one well-reconstructed primary vertex (PV) [50] is imposed in the analysis.
Furthermore, two kinematic (analysis) cuts are applied in both channels after the object selection, that is introduced in the next subsections. They consist of a p_T / p_T^{miss} and a $\Delta\phi$ cut. It accounts for the balance in momentum and the back-to-back kinematics. The ratio of momenta is required to be $0.4 < p_T / p_T^{miss} < 1.5$, and the difference in the azimuth angle to be $\Delta\phi > 2.5 \approx 0.8\pi$. The kinematic cuts are identical for the electron and muon channels.
Since the recommendations for Run-3 are preliminary, no p_T^{miss} filters are currently used in this analysis.

5.1 Electron channel

In the electron channel, the high energy electrons are identified using the high energy electron positron identification (HEEP ID). The details on the HEEP ID are given in table 5.1.

Variable	**Barrel**	**Endcap**
E_T	$> 35\,\text{GeV}$	$> 35\,\text{GeV}$
$\lvert\eta\rvert$ range	$\eta_{SC} < 1.4442$	$1.566 < \eta_{SC} < 2.5$
isEcalDriven	$= 1$	$= 1$
$\Delta\eta_{in}^{seed}$	< 0.004	< 0.006
$\Delta\phi_{in}$	< 0.06	< 0.06
H/E	$< 1/E + 0.05$	$< 5/E + 0.05$
full 5x5 $\sigma_{i\eta i\eta}$	n/a	< 0.03
full 5x5 E^{2x5}/E^{5x5}	> 0.94 OR $E^{1x5}/E^{5x5} > 0.83$	n/a
EM + Had Depth 1 Isolation	$< 2 + 0.03 \cdot E_T + 0.28 \cdot \rho$	$< 2.5 + 0.28 \cdot \rho$ for $E_T < 50$ else $< 2.5 + 0.03 \cdot (E_T - 50) + 0.28 \cdot \rho$
Track Isol: Trk Pt	< 5	< 5
Inner Layer Lost Hits	$<= 1$	$<= 1$
$\lvert d_{xy}\rvert$	$< 0.02\,\text{mm}$	$< 0.05\,\text{mm}$

Table 5.1: Selection criteria for HEEP ID v7.0 [51].

E_T: The total energy deposit from the electron in the ECAL is multiplied by $\sin\theta$ to get the transverse energy of the electron. The angle θ is measured by the innermost layer of the tracker system.

η_{SC}: The pseudorapidity measured by a supercluster (SC) in the ECAL is denoted as η_{SC}. A supercluster is a cluster of crystals in the ECAL.

***isEcalDriven*:** When reconstructed via the PF algorithm, an electron does not need to be detected in the ECAL. This variable guarantees that the electron is found in the ECAL.

$\Delta\eta_{in}^{seed}$ *and* $\Delta\phi_{in}$: The absolute value of the difference in η and ϕ, that are measured in the tracker system and the ECAL's SC.

H/E**:** This is the ratio of the total hadronic energy H to the energy deposited by the electron in the ECAL inside a cone of radius 0.15 centered at the electron's track.

$full\ 5x5\ \sigma_{i\eta i\eta}$**:** A measure of spread in the pseudorapidity in units of crystals, in 5x5 block centered around the electron's seed crystal.

$full\ 5x5\ E^{2x5}/E^{5x5}$**:** The ratio of energy deposited around the seed crystal in a 2x5 (or 1x5) array to the 5x5 array.

$EM + HadDepth1Isolation$**:** This is used to account for jets that are misidentified as electrons mainly from the QCD background. EM is the sum of all transverse energies with $E_T > 0.08\,\text{GeV}$ inside a cone of radius 0.3 around the electron inside the ECAL. Had Depth 1 is the energy deposition in a cone of radius 0.15 to 0.3 around the position of the electron inside the HCAL. These two energies are summed and related to the electron's transverse energy E_T and the mean energy density per unit area ρ.

$TrackIsol : TrkPt$**:** Inside a cone of 0.3 around the electron's track, while excluding an inner cone of radius 0.04, the sum of all transverse momenta must not exceed 5 GeV to suppress electrons originating from jets.

$InnerLayerLostHits$**:** This is the number of lost hits from trackers that did not send a signal in the electron's reconstructed trajectory. It reduces the influence of pair-produced electrons.

d_{xy}**:** Radial distance between the reconstructed PV and the trajectory measured in the inner tracker system. This is used to reduce the impact of cosmic ray leptons such as muons or electrons.

The two triggers, HLT_Photon200 and HLT_Ele115_CaloIdVT_GsfTrkIdT, were combined using a logical OR in the electron channel [52, 53, 54]. These two triggers select either a single electron with a reconstructed $E_T > 115\,\text{GeV}$ or $E_T > 200\,\text{GeV}$ in the ECAL. The Photon200 trigger utilizes the information from the electromagnetic shower in the ECAL. The Ele115 trigger uses the energy threshold together with informations from the tracker to reconstruct electrons. In comparison to Run-2, the Ele115 trigger combined with the p_T and the p_T^{miss} cuts are new, where the lower threshold is improving reconstruction in the low-energy region. The HEEP ID, together with a $|\eta| < 2.3$ cut and the triggers, form the preselection cut for the electron channel.
A second lepton veto is also implemented to reduce contributions from dileptonic decays like a Z decay into two leptons, where both are reconstructed as leptons and not only a single lepton, resulting in DY background. It consists of rejecting events with electrons and muons with a $p_T > 25\,\text{GeV}$ and if they are identified with a loose ID for muons or HEEP ID for electrons.
To account for the top quark background at low energies, a p_T cut is placed, accepting only events where the leading electron has a momentum of $> 130\,\text{GeV}$. This momentum cut also removes potentially mismodelled low energy regions. Also, since a balance in momentum between the lepton and neutrino is expected, a cut is placed requiring $p_T^{miss} > 120\,\text{GeV}$. The preselection cut combined with the second lepton veto, the p_T cut, and the p_T^{miss} cut comprise the electron object (or quality) cut.
Afterwards are the aforementioned kinematic (analysis) cuts applied. The selection criteria in the electron channel are shown in table 5.2.

Cut	Sub-cut	Details
Object (Quality) cuts	Preselection	HLT_Photon200 OR HLT_Ele115_CaloIdVT_GsfTrkIdT is HEEP==1 AND $\|\eta\| < 2.3$
	2nd lepton veto	events with second lepton (e or μ) with $p_T > 25\,\text{GeV}$ & identified with loose ID for muons and HEEP ID for electrons are rejected
	p_T^e-cut	$p_T^e > 130\,\text{GeV}$
	p_T^{miss}-cut	$p_T^{miss} > 120\,\text{GeV}$
Kinematic (Analysis) cuts	p_T^e / p_T^{miss}-cut	$0.4 < p_T^e / p_T^{miss} < 1.5$
	$\Delta\phi$-cut	$\Delta\phi > 2.5$

Table 5.2: Selection criteria in the electron channel.

5.2 Muon channel

The muon channel does not have a nanoAOD variable similar to the HEEP ID for electron, therefore each selection criteria is applied separately. The details on the muon preselection cut without the triggers are given in table 5.3.

Variable	Cut
$\|d_{xy}\|$	$< 0.02\,\text{mm}$
$\|d_z\|$	$< 0.5\,\text{mm}$
$\|\eta\|$	< 2.4
σ_{p_T} / p_T	< 0.3
Muon_tkRelIso	< 0.1
Muon_highPurity	$= 1$
Muon_highPtId	$= 2$
b-quark veto	$nJet > 6$ OR b-tagging discriminant > tight WP

Table 5.3: Preselection criteria for the muon channel (Muon-ID). The triggers are not included here. The working point for the b-quark veto can be found in [55].

d_z**:** This is the impact parameter in the z-direction, similar to d_{xy}.

σ_{p_T} / p_T**:** The relative uncertainty on the reconstructed transverse momentum is required to be less than 30%.

*Muon_tkRelIso***:** Inside a cone of radius 0.3 the sum of all transverse momenta, except the muons, has to be less than 10%, to suppress muons originating from jets.

*Muon_highPurity***:** This requires mainly good impact parameters with a high significance in them. It also asks for a good χ^2/n_{dof} for the track. This variable ensures that muons with an unreasonably high reconstructed momentum are rejected if they don't pass this requirement [49, 56].

*Muon_highPtId***:** This selection is used to have the best reconstruction of high p_T muons ($p_T >$ 200 GeV) track parameters, while not using external information in the event. The chosen working point is that of a global *highPt* muon. The other WP would be that of a tracker *highPt* muon, which is included in the global *highPt* muon. The tracker highPt working point is used for a better reconstruction of boosted Z events [57].

b − quark veto: This veto is applied to reject muons where the leading jet has been tagged as originating from a b-quark according to the deepJet algorithm or with more than five jets in one event. This also suppresses the top background, because the top-quark is likely to decay into a b-quark.

To complete the muon preselection cut, three triggers combined using a logical OR are used. The HLT_Mu50 trigger being the main path, and adding the HLT_HighPtTkMu100 and HLT_CascadeMu100 trigger, being the reference paths [58, 59].
Like in the electron channel, a second lepton veto is applied, with the only difference being that in the muon channel, the electron is identified using the loose WP of the *cutBased* ID [50]. The p_T-cut in the muon channel has a threshold of 53 GeV. No p_T^{miss}-cut is applied in the muon channel to account for the lower p_T threshold. Similar to the electron channel, the preselection-cut together with the second lepton veto and the p_T-cut form the muon object (or quality) cut. The kinematic (analysis) cuts are the same as for the electron channel. The selection criteria in the muon channel are shown in table 5.4.

Cut	Sub-cut	Details
Object (Quality) cuts	Preselection	in table 5.3
	2nd lepton veto	events with second lepton (e or μ) with $p_T > 25\,\text{GeV}$ & identified with loose ID are rejected
	p_T^{μ}-cut	$p_T^{\mu} > 53\,\text{GeV}$
Kinematic (Analysis) cuts	p_T^{μ}/p_T^{miss}-cut	$0.4 < p_T^{\mu}/p_T^{miss} < 1.5$
	$\Delta\phi$-cut	$\Delta\phi > 2.5$

Table 5.4: Selection criteria in the muon channel.

6 Signal studies

This section is dedicated to the study of the signal efficiencies for Run-3 and the impact of different coupling ratios on the W′ signal. The first part of this section presents the signal efficiencies in both channels and compares them to the Run-2 results. The third part investigates the effect of increasing or decreasing the coupling ratio and its impact on the W′ signal M_T distribution. For simplicity, the coupling ratio called coupling this chapter. The variable for the coupling is called kR, inspired by the name of the nanoAOD coupling samples [60]. The selection criteria for the electron channel are given in table 5.2 and the muon channel in table 5.4, respectively.

6.1 Signal efficiencies

The signal efficiency shows the effect of the selection criteria on the signal. For Run-2 it is calculated by multiplying the geometrical acceptance by the efficiency ε of the kinematic selection and the trigger thresholds. In this analysis is the total efficiency ε defined as the product of the object selection efficiency ϵ_1 by the kinematic selection efficiency ϵ_2. The kinematic selection efficiency is the ratio of events that pass the object selection over the events that pass the object and kinematic selection. Therefore is ε the ratio of events that pass all selection requirements over the total number of events in the signal sample. The error-bars in the efficiency graphs in fig. 6.1 and fig. 6.2 are statistical uncertainties.
This efficiency is dependent on the W′ boson mass and typically has a "banana-shape" behaviour. The signal efficiency is lower at low masses, because of the trigger and transverse momentum thresholds. Most of the Jacobian peak is being cut, resulting in lower signal efficiency. This behaviour can be seen in fig. 6.1 and fig. 6.2. In the muon channel the signal efficiency in the low-mass region is higher because of the lower transverse momentum threshold. The muon selection roughly accept events with $M_T > 100\,\text{GeV}$, while the electron selection criteria only from $M_T > 200\,\text{GeV}$ for Run-3 and $M_T > 400\,\text{GeV}$ for Run-2.
The increase in the signal efficiency for the electron channel compared to Run-2 is shown in fig. 6.1 for 3 cases. First, the efficiency graph taken from the Run-2 Analysis Note (AN), then Run-3 selection and the Photon200 trigger with and without the Ele115 for Run-2 samples and, also Run-3 cuts and triggers for Run-3 samples. The lower momentum thresholds, due to the newly developed Ele115 trigger, recover most of the previously rejected on-shell events for the low-mass samples. The transverse mass distribution for high-mass samples have a high off-shell production of W′ bosons, shown in fig. 4.2. Using the Ele115 trigger and lower momentum thresholds for p_T^e and p_T^{miss} in the electron channel, the low-energy off-shell events can also be recovered resulting into an increase in signal efficiency for the high-mass samples. The Run-3 efficiency flattens out more for high-mass samples compared to Run-2. This will improve the W′ boson search at higher energies using the current exclusion limit in the electron channel for its mass [49].
One can also observe the shift of the peak in the efficiency graph from the electron channel towards higher masses in Run-3 compared to Run-2. The highest efficiency for Run-2 was approximately 72.1% (at 2200 GeV) [49]. In Run-3, it is $\approx$ 76.6% (at 2600 GeV) (see fig. 6.1). The higher center-of-mass energy has an impact on the peak due to the increased phase-space, enabling the production of high-mass particles which shift the peak towards higher masses. The electron channel's signal efficiency at 6000 GeV in the Run-2 AN is $\approx$ 44.5%. The efficiency at 6000 GeV for the electron channel using Run-2 samples without the Ele115 trigger is $\approx$ 47.2%. When including the Ele115 trigger for the Run-2 samples the efficiency rises to $\approx$ 53.3%. Com-

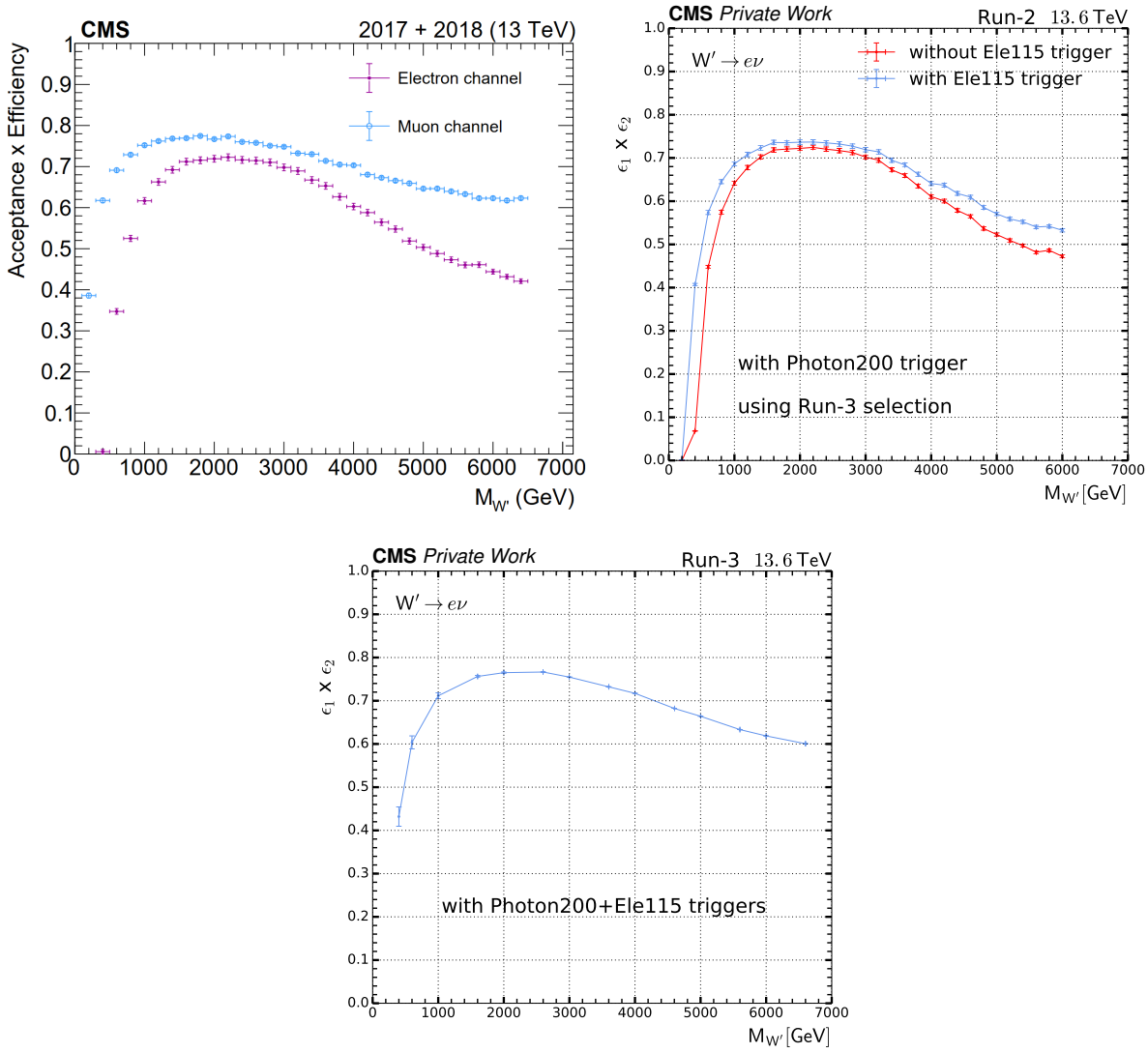

Figure 6.1: In this figure are the signal efficiencies in the electron channel for Run-2 (top) and Run-3 (bottom) samples presented. The top left graph shows the signal efficiencies for the electron and muon channel using the Run-2 selection. It was taken from this AN [49]. The top right figure shows the graph of the signal efficiency of Run-2 signal samples using the Run-3 selection with and without the Ele115 trigger. The bottom graph displays the signal efficiency using the full Run-3 selection presented in table 5.2. The uncertainties in the graphs are only of statistical nature. The sample list is in the Appendix in table 4.3.

paring this with the efficiency for Run-3, $\approx$ 61.9%, one can see the impact of the new trigger path.

The muon channel's trigger threshold is roughly half of the electron channel's resulting in even larger efficiency for the low- and high-mass samples than the electron channel (see fig. 6.2). The highest efficiency was $\approx$ 77.4% (at 1800 GeV) for Run-2 [49, 61]. For Run-3 it shifted to $\approx$ 75.3% (at 1600 GeV) (see fig. 6.2). This originates from unrevised cuts for the muon channel, because most of the current cuts for the muon channel have already been used for Run-1 [4]. Also the b-tagging veto has not yet an official recommendation for the discriminant [55]. This results in

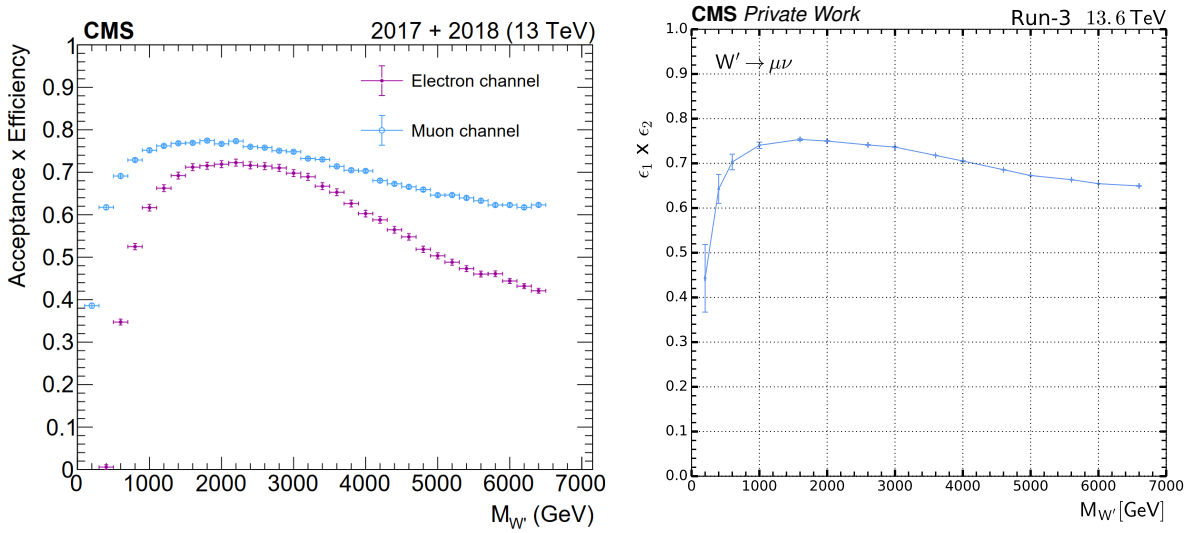

Figure 6.2: In this figure are the signal efficiencies in the muon channel. The left graphic again shows the Run-2 and the right graphic the Run-3 signal efficiency. The efficiency flattens out more in the high-mass region and with higher values for the low- and high-mass region. The Run-2 selection can be found in [49], while the Run-3 selection has been presented in table 5.4. The uncertainties in the graphs are only of statistical nature. The sample list is in the Appendix in table 4.3.

a deviation from the electron channel's efficiency increase compared to Run-2. Nonetheless, has the efficiency increased in the endpoints of the graph compared to Run-2. This is mainly because of the higher center-of-mass energy increasing the on-shell production and shifting the events in the acceptance region of the cuts. The signal efficiency at 6000 GeV for the muon channel in Run-2 is $\approx$ 62%, while for Run-3 it is at $\approx$ 65.4%.

6.2 SSM signal distributions

The SSM assumes a coupling of 1.0 for the W' boson with respect to the SM W boson. The expected signature of the W' boson decay in the lepton channel was mentioned in subsubsection 4.3.2. In fig. 6.3 (fig. 6.4) are the signal sample distributions for the electron (muon) channel for a coupling of 1.0 presented. Both figures display signal samples with three different W' masses: 1000 GeV, 3000 GeV, and 5000 GeV. The distributions are normalized to a luminosity of 20.7 fb^{-1}. The normalization procedure was also introduced in subsubsection 4.3.2. The same figure for the muon channel can be found in the Appendix in fig. 6.4, because both channels show similar behaviour. Differences in the distributions from both channels will be mentioned. The number of events decreases for signal samples with higher W' masses, but the shape of the ϕ, ϕ^{miss}, and η distributions remains consistent for all three masses. The ϕ and ϕ^{miss} distributions exhibit the expected azimuthal isotropy. In the electron channel, the η distributions show a cut between the barrel and endcap regions of the detector, which is incorporated into the HEEP ID (details can be found in table 5.1). Both pseudorapidity distributions are centered around roughly 0, and the number of events decreases as $|\eta|$ increases.

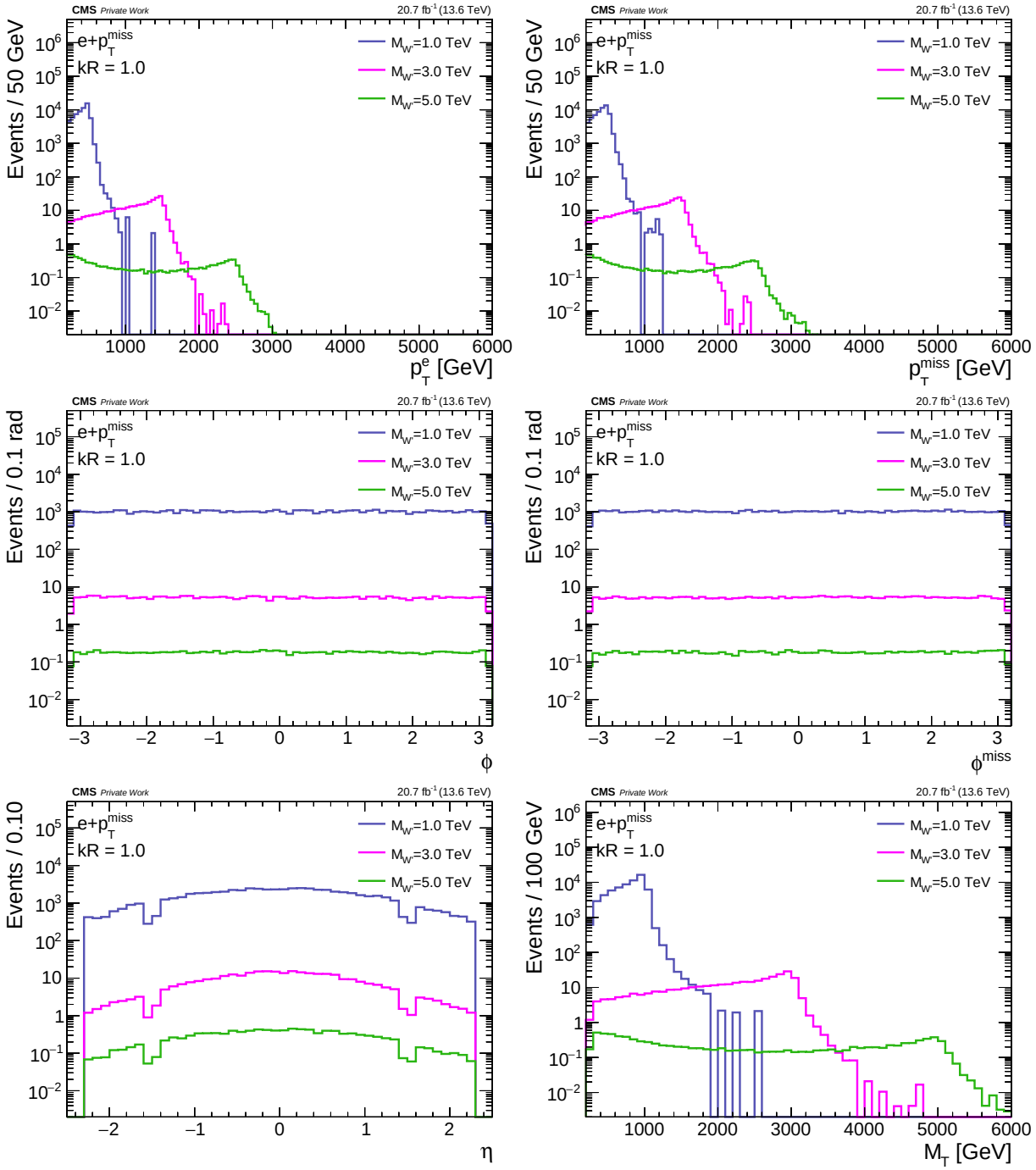

Figure 6.3: Distributions for p_T (top left), p_T^{miss} (top right), ϕ (middle left), ϕ^{miss} (middle right), η (bottom left), and M_T (bottom right) at a W′ signal sample mass of 1000 , 3000 , and 5000 GeV in the electron channel with a coupling of 1.0. The M_T distribution peaks at the W′ mass of the signal sample. The transverse momentum distributions Jacobian peak is located at half the W′ mass of the signal sample. The azimuth angle distributions are isotropic and the pseudorapidity distribution is centered around 0, as expected. The overlap in the barrel and endcap region has been cut out in the η distributions. The transverse mass distributions are similar to the distributions in fig. 4.2.

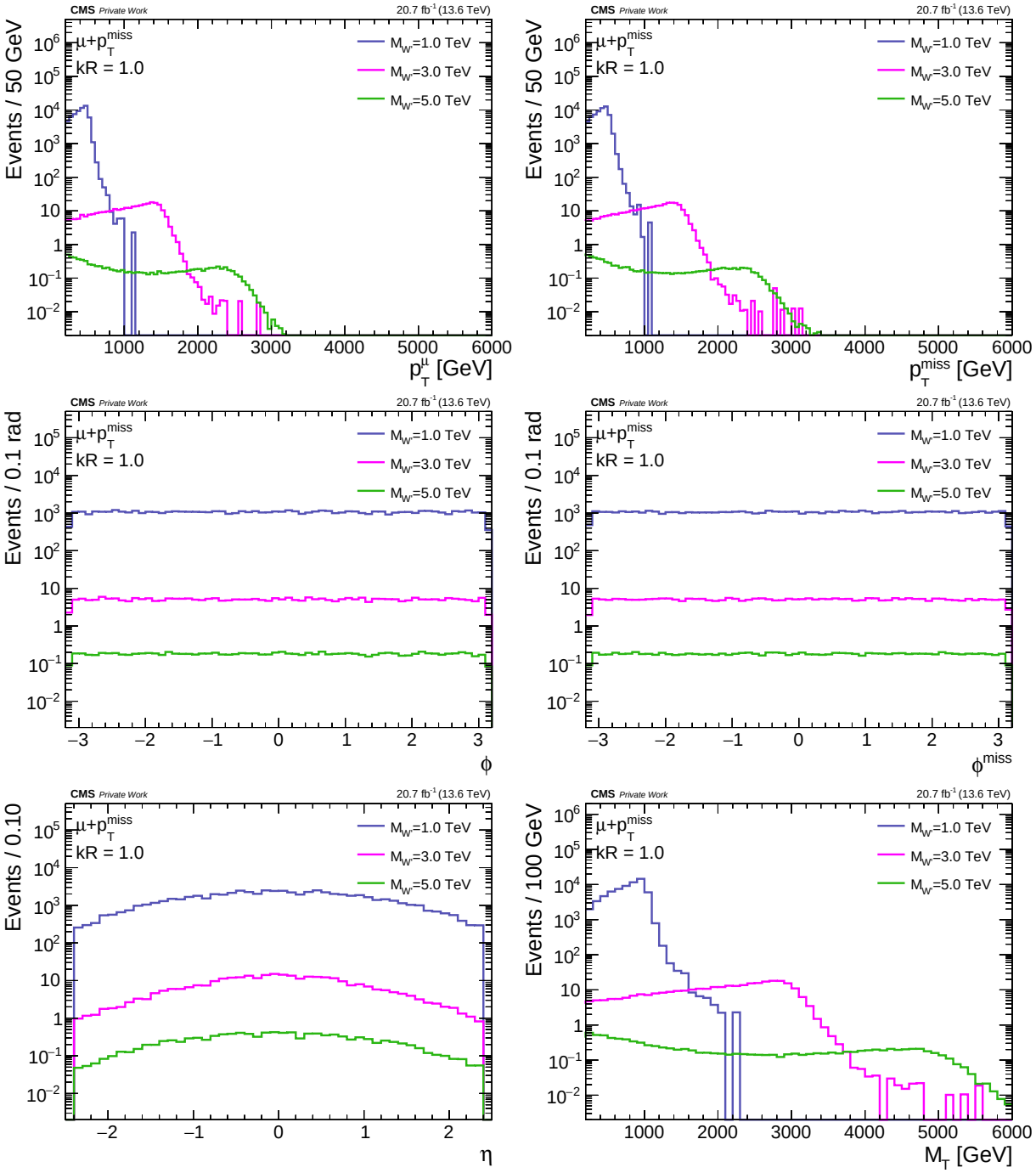

Figure 6.4: Distributions for p_T (top left), p_T^{miss} (top right), ϕ (middle left), ϕ^{miss} (middle right), η (bottom left), and M_T (bottom right) at a W' signal sample mass of 1000 , 3000 , and 5000 GeV in the muon channel with a coupling of 1.0. The distributions in the muon channel are similar to the distributions in the electron channel (see fig. 6.3).

The p_T and p_T^{miss} distributions indicate an increase in off-shell produced W′ bosons for higher W′ masses, while the low-mass samples exhibit a prominent on-shell peak. The x-value of the peak of both momentum distributions are at half the W′ signal sample mass. This means that the transverse momentum distribution of the 1000 GeV sample peaks at 500 GeV. When reconstructing the W′ mass using eq. (3.2), the on-shell (off-shell) production tendency of the 1000 GeV (5000 GeV) momentum distribution is inherited. This originates from the formula for calculating the transverse mass (see 3.2). The formula for the transverse mass can be approximated, for balance in p_T and back-to-back kinematics, to be $\approx 2 \cdot p_T^l$. This does not change the shape of the distribution, but stretches the x-axis by a factor of 2. This results in sharp on-shell M_T peaks for the 1000 GeV sample and an increased width of the 5000 GeV off-shell peak. The electron channel exhibits sharper transverse momentum and transverse mass peaks due to the higher energy resolution in the ECAL at high energies, as mentioned in fig. 4.2.

6.3 Varying coupling strengths

The preceded subsection studied the form of the kinematic distributions for the SSM W′ boson and assumed a coupling of 1. The variation of the coupling in the decay vertex (see fig. 2.1) is further investigated in this subsection. The coupling and the mass have a significant impact on the signal shape [62]. An increase in the W′ mass results into a higher decay width Γ. This also holds for higher couplings, making a process more likely. This can be verified by using the rules for feynman graphs and Fermi's golden rule [63].

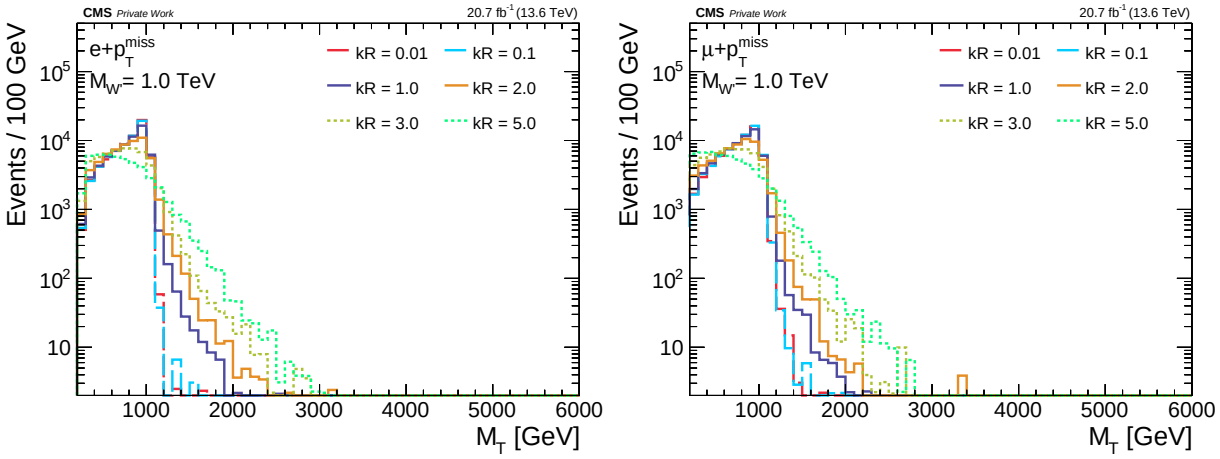

Figure 6.5: Transverse mass distributions for the electron (left) and muon channel (right), respectively. The plots have a signal samples mass of 1000 GeV. When increasing the coupling, the off-shell W′ boson production and the decay width increases. Both channels show similar event numbers. The distributions in the electron channel have sharper on-shell peaks for high-masses, due to higher energy resolution in the ECAL than the muon chambers.

The expected form of the kinematic distributions (p_T, p_T^{miss}, M_T, η, ϕ and ϕ^{miss}) have been mentioned in subsubsection 4.3.2. In fig. 6.5 is the shift from on-shell to off-shell visible for the 1000 GeV samples when increasing the couplings. Also the aforementioned increase in Γ for the high coupling sample can be seen. The peaks in the electron channel are sharper, due to the aforementioned higher energy resolution in the ECAL, for high energies, compared to the muon chambers. In fig. 6.8 are the other variables, such as the azimuth angle for transverse momentum of the lepton and the missing transverse momentum, for a signal sample mass of 1000 GeV in

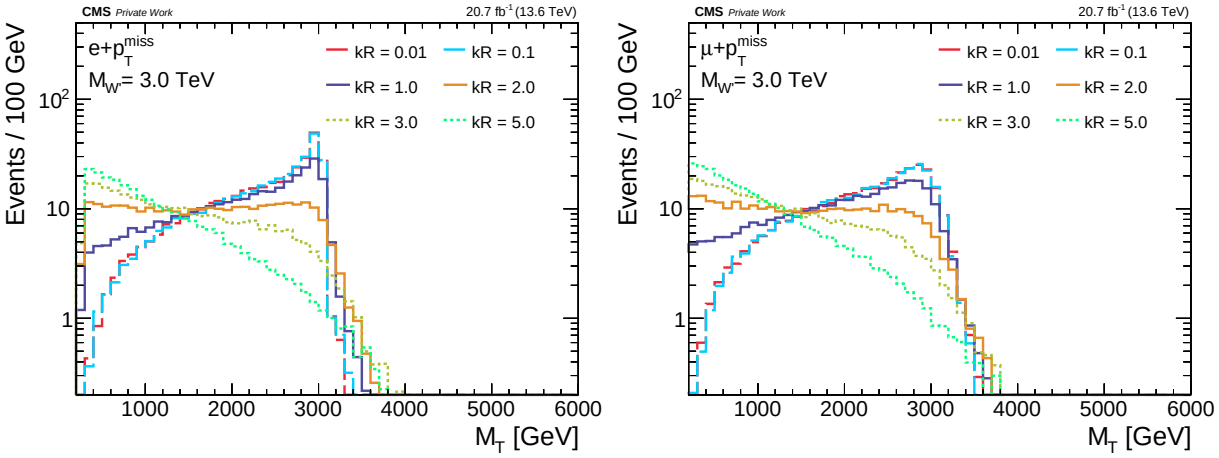

Figure 6.6: Transverse mass distributions for the electron (left) and muon channel (right), respectively. The plots have a signal samples mass of 3000 GeV. Compared to fig. 6.5, the decay width has increased for the same couplings. Similar to the sample mass of 1000 GeV, both channels show similar event numbers as well. The on-shell peaks in the electron channel are also sharper in this figure.

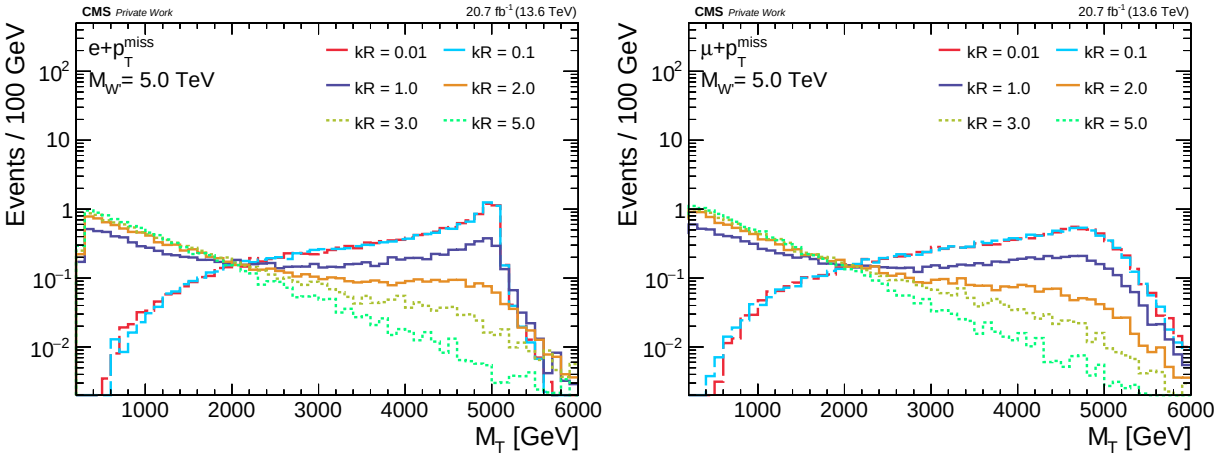

Figure 6.7: Transverse mass distributions for the electron (left) and muon channel (right), respectively. The plots have a signal samples mass of 5000 GeV. Again show both channel similar event numbers, with the electron channel's on-shell peaks being sharper.

the electron channel shown. The muon channel shows similar behaviour overall in fig. B.2 and is therefore not discussed here, but added in the Appendix. The momentum distributions also show a peak-shift from on-shell to off-shell production when increasing the coupling, similar to the transverse mass distributions. The peaks at the transverse momentum spectrum are at half the energy of the M_T distribution. This is consistent with the preceding subsection and the formula for M_T, given in eq. (3.2), with back-to-back kinematics. The ϕ and ϕ^{miss} distributions are isotropic for different couplings, as expected, because the W' decay has rotational symmetry. The η distribution is also, as expected, centered around 0, with a cut on the overlap between the barrel and endcap region for the electron channel.

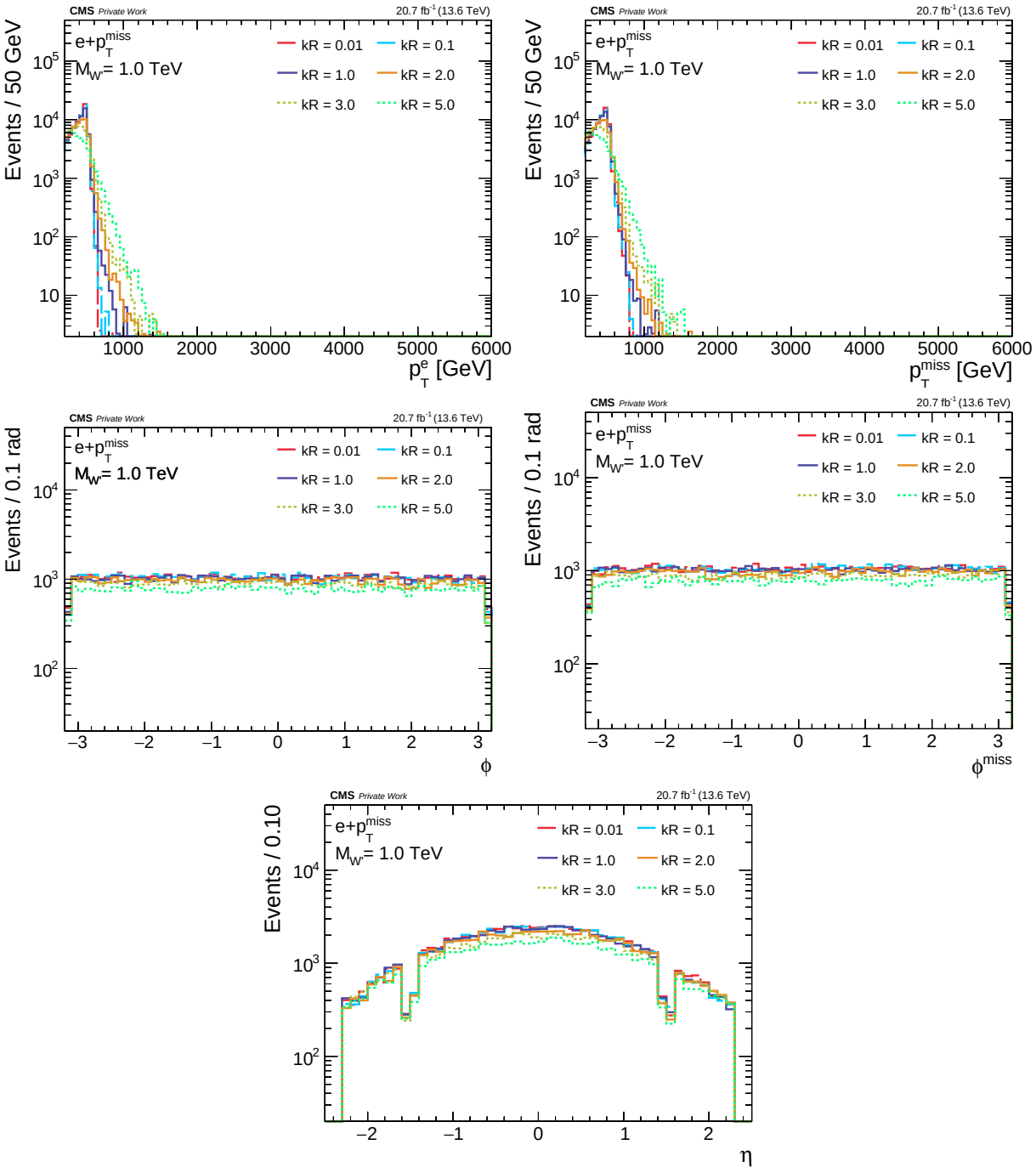

Figure 6.8: Distributions for p_T (top left), p_T^{miss} (top right), ϕ (middle left), ϕ^{miss} (middle right), and η (bottom) at a W′ signal sample mass of 1000 GeV in the electron channel with 6 different couplings. The transverse momentum distributions show similar behaviour like fig. 6.5. The azimuth angle distributions are isotropic and the pseudorapidity distribution is centered around 0, as expected.

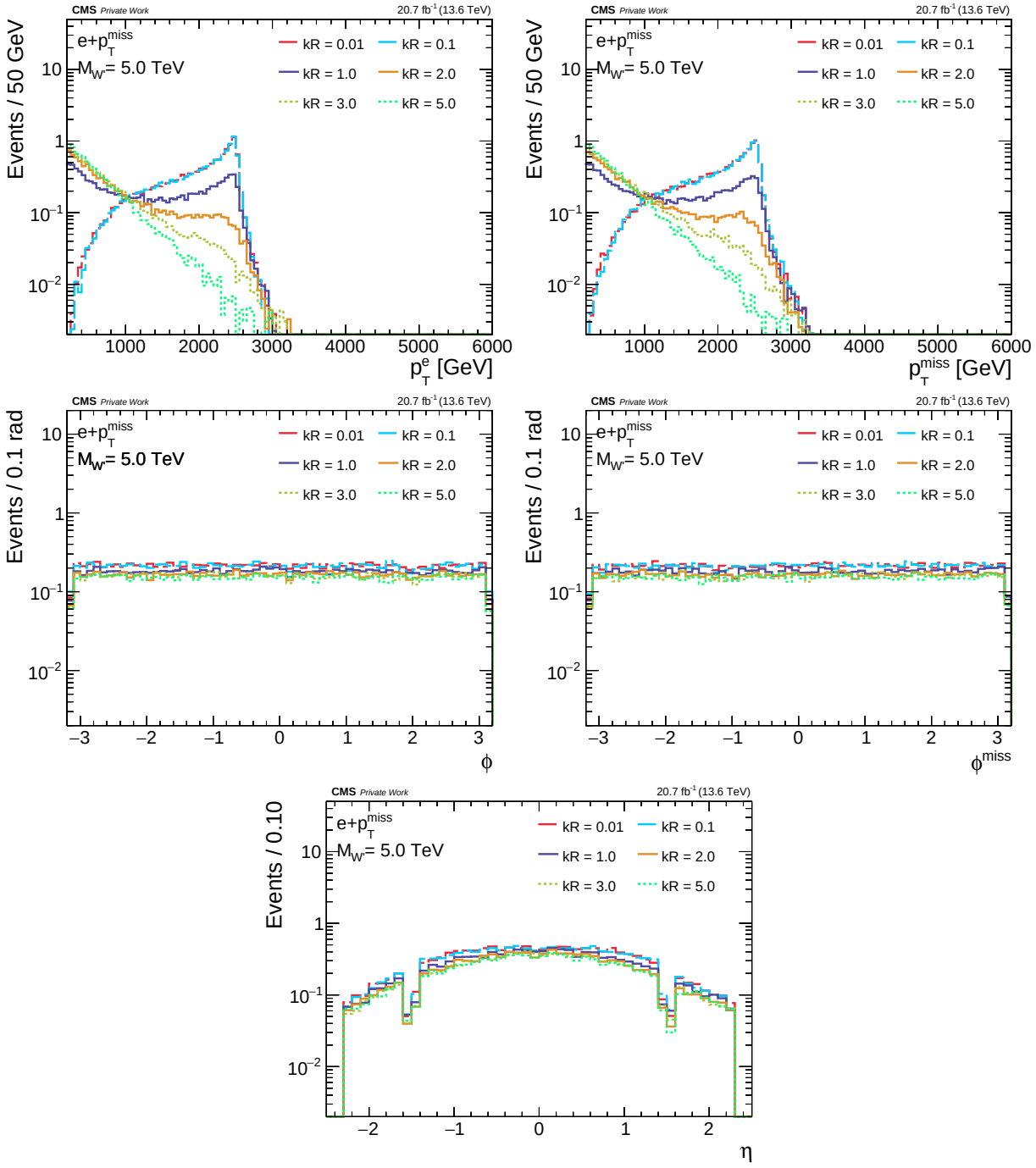

Figure 6.9: Distributions for p_T (top left), p_T^{miss} (top right), ϕ (middle left), ϕ^{miss} (middle right), and η (bottom) at a W′ signal sample mass of 5000 GeV in the electron channel with 6 different couplings. The number of events has decreased compared to fig. 6.8, due to a lower cross section. The transverse momentum distributions show similar behaviour like fig. 6.7. The azimuth angle and pseudorapidity distributions look downscaled compared to a signal sample mass of 1000 GeV.

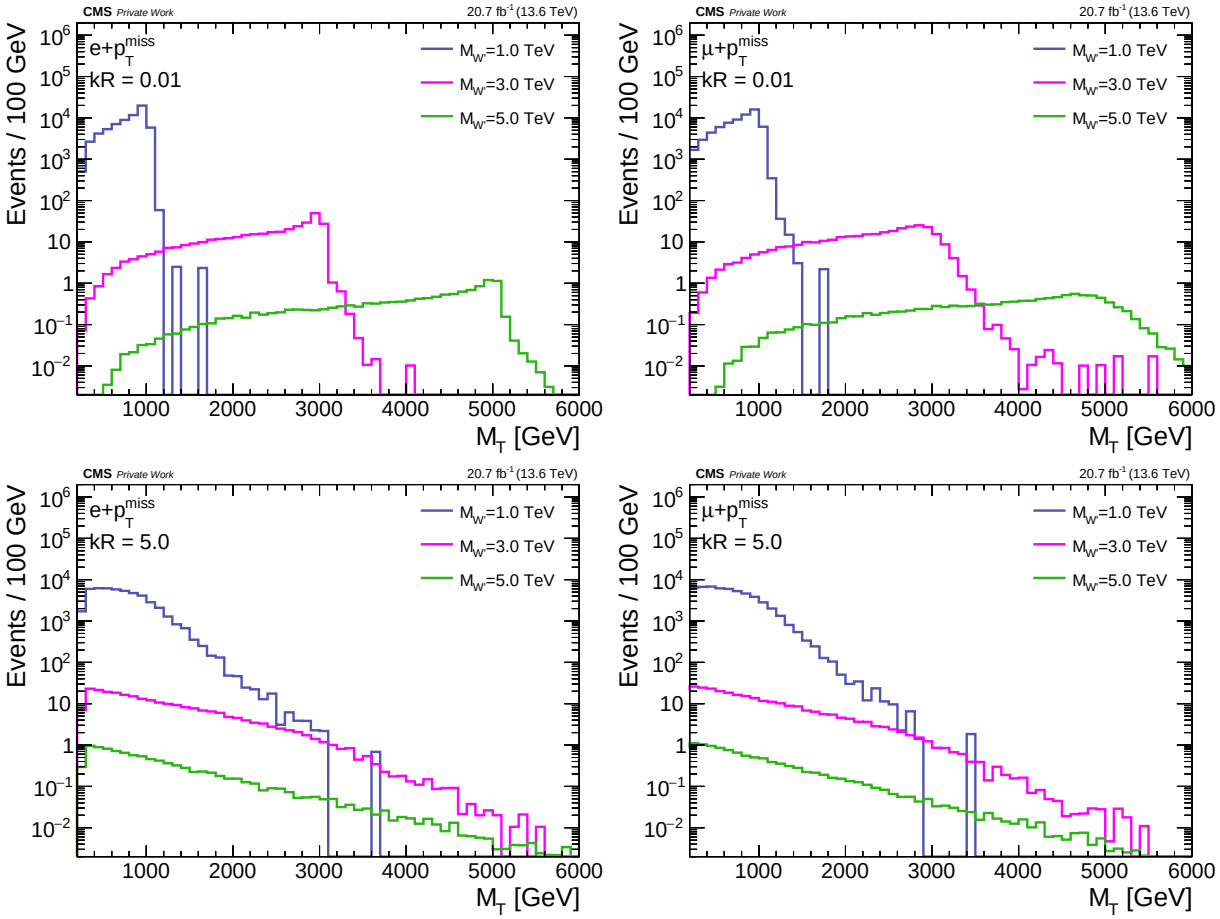

Figure 6.10: Transverse mass distributions for the electron (left) and muon channel (right), respectively. The plots in have a coupling of 0.01 (top) and 5.0 (bottom). The distributions in the electron channel have sharper peaks for high-masses and low couplings. The W′ boson is mainly on-shell produced for low couplings. The Jacobian peaks are smeared out for high couplings. The W′ bosons are rarely on-shell produced, with the peak only visible for a mass of 1000 GeV. This higher coupling is harder to detect, as most of the W′ boson production is not at its on-shell mass.

When additionally increasing the mass, as shown in fig. 6.6 and fig. 6.7, Γ becomes larger. Especially for the 5000 GeV sample are the different coupling histograms distinguishable. The change from mainly off-shell to mainly on-shell is not a uniform process, but primarily happens in the interval between a coupling of 0.1 and 1.0. For high couplings the Jacobian peak of the transverse mass distribution vanishes smearing out the signal. In fig. 6.9 are the other variables for a signal sample mass of 5000 GeV shown in the electron channel. Transverse momentum distributions show a similar trend as the transverse mass distribution. The transverse momentum peaks widths are larger for high couplings, with, like in fig. 6.8, a shift from on-shell to off-shell production between the couplings 0.1 and 1.0. The number of events has decreased compared to the distributions from the low-mass samples, because the samples are reweighted to the luminosity, with the high-mass samples having a lower cross section (see table 4.3). Nonetheless, the azimuth angle and pseudorapidity distributions are similar to the distributions in fig. 6.8. The ϕ, ϕ^{miss}, and η distributions show similar behaviour with a lower number of events, compared the 1000 GeV distributions. Other distributions for the other variables such as ϕ or η for the different

signal samples masses in both channels can be found in the Appendix in fig. B.1 to fig. B.4.
The coupling can also be held constant, while varying the sample mass. This is shown in fig. 6.10. The coupling in this figure is 0.01, while the transverse mass distributions for three different sample masses (1000 GeV, 3000 GeV and 5000 GeV) are presented. The low coupling decreases the probability of a process involving a W′ boson, therefore is the on-shell peak production becoming more dominant. The figs. 6.3 and 6.4 ($kR = 1.0$) and fig. 6.10 ($kR = 0.01$ and $kR = 5.0$) show the movement of the peaks from on-shell to off-shell. For the coupling of 5.0 is the peak not visible. The likelihood of a process involving a W′ boson has increased that it is mainly produced off-shell and not necessarily on-shell. The off-shell peaks for this high coupling are within the control background region for masses below 1500 GeV. It is harder to detect than a sharp on-shell resonance, as shown in fig. 6.10 for the coupling of 0.01. More distributions for all couplings can be found in the Appendix B from fig. B.5 to fig. B.14.

6.4 Impact of kinematic selection

The plots in this section include background simulation, which is stacked for different background types (see table A.1), and is represented with various colors. The figures additionally include signal distributions for two different W′ masses, which are shown using solid lines.
This section investigates the impact of the kinematic selection criteria on the SM background and the W′ signal. In fig. 6.11, there are distributions for the kinematic variables ($\Delta\phi$ and p_T^l / p_T^{miss}). The distributions are after applying the object selection criteria (see tables 5.2 and 5.4). The p_T^l / p_T^{miss} distributions peak at roughly 1, while the $\Delta\phi$ distributions peak at around π for the W′ signal, as expected. This results from the back-to-back kinematics and the balance in p_T in the W′ decay. Both channels exhibit the same behavior, with the electron channel having fewer background events than the muon channel, which is due to the higher trigger threshold. Most of the reconstructed signal events are within the p_T^l / p_T^{miss} interval of 0.4 to 1.5. Therefore, a selection criterion was applied that accepts events inside this p_T^l / p_T^{miss} range.
The resulting distributions are shown in fig. 6.12. The number of SM background events has decreased in both channels, especially in the muon channel. The QCD multijet and W background are mainly rejected by this selection criterion. Similarly to the p_T^l / p_T^{miss} selection, most of the signal events are not uniformly distributed but lie within a $\Delta\phi$ interval from 2.5 to π. This selection criterion is indicated by a vertical dotted line at $\Delta\phi = 2.5$.
The resulting p_T^l / p_T^{miss} distributions after the application of the cuts for both channels are shown in fig. 6.13. The QCD multijet background has significantly reduced in both channels, especially in the muon channel. The background events at the border of the p_T^l / p_T^{miss} interval have also reduced, making the peak of the distributions sharper around 1 in both channels.
Therefore, it can be concluded that the kinematic selection criteria are essential for the analysis. They significantly reduce the SM background contribution, while still accepting most of the W′ signal.

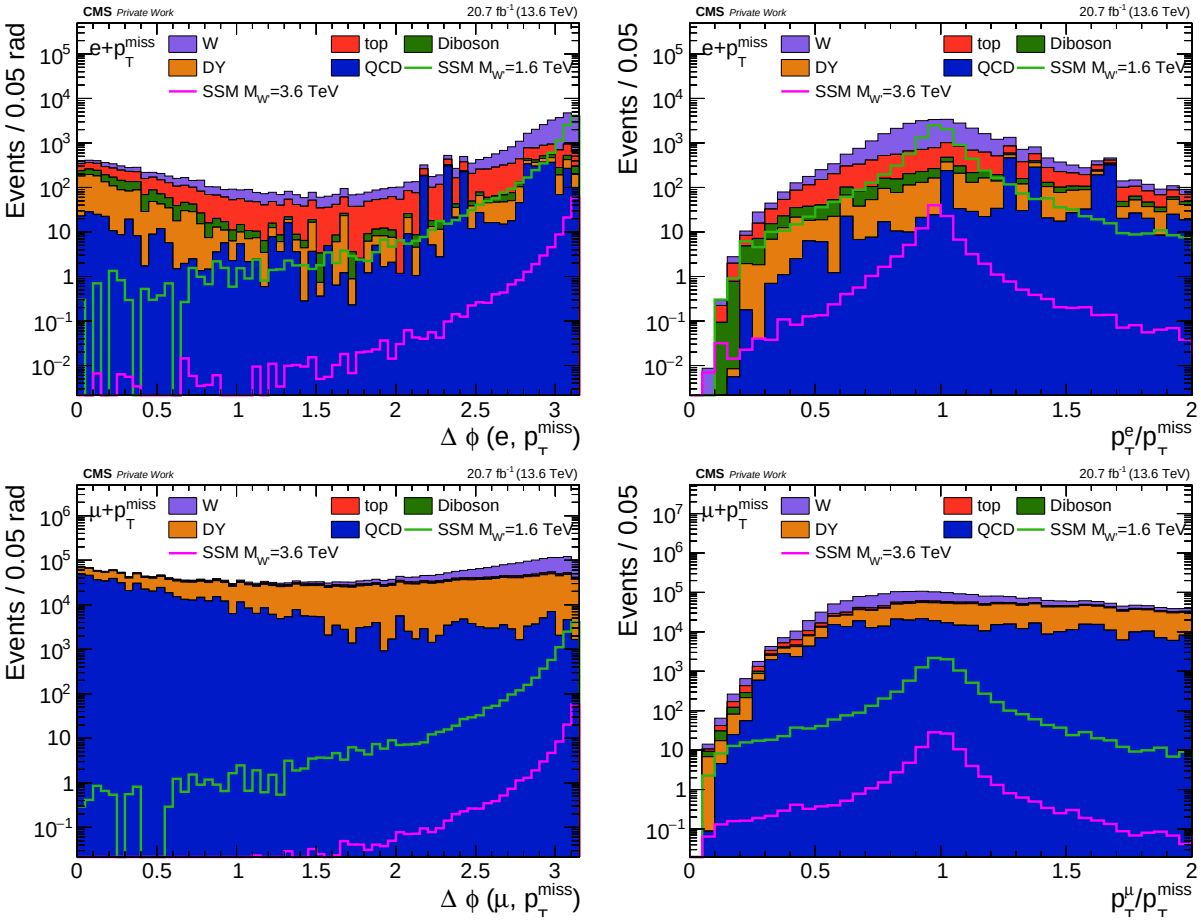

Figure 6.11: Distributions for $\Delta\phi$ (left) and p_T^l / p_T^{miss} (right) for the electron (top) and muon channel (bottom). The peak of the p_T^l / p_T^{miss} distribution is around 1. The electron channel has less background than the muon channel, due to the higher trigger threshold. When comparing the SM background to the signal sample distribution, it is visible that most of the signal lies within the interval from 0.4 to 1.5. The distributions are after the object selection, but before applying the kinematic selection criteria. A peak at roughly π in the $\Delta\phi$ distribution can be seen in both channels.

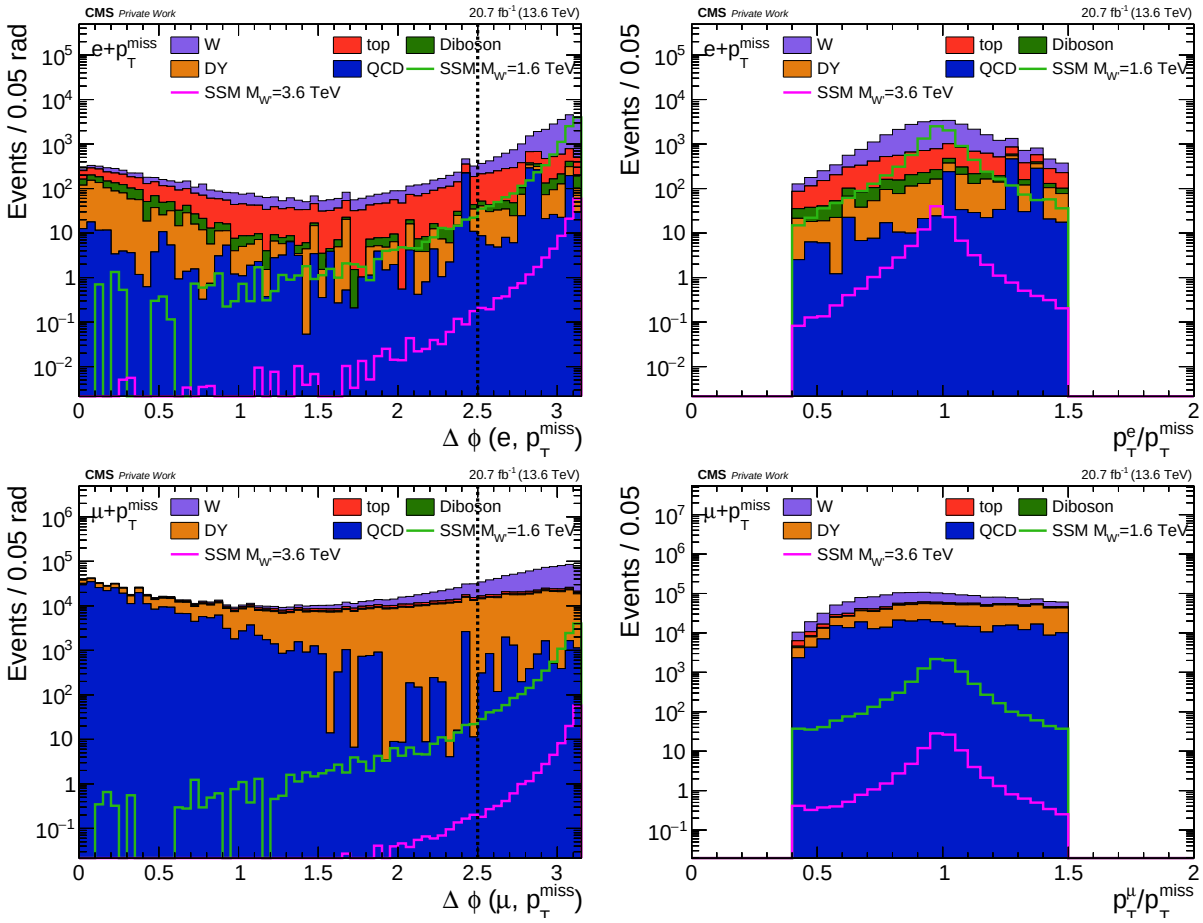

Figure 6.12: Distributions for $\Delta\phi$ (left) and p_T^l / p_T^{miss} (right) for the electron (top) and muon channel (bottom). The background contribution in the $\Delta\phi$ distributions decreased, due to the p_T^l / p_T^{miss} cut. This is especially visible in the muon channel. Similar to fig. 6.11, the signal sample events are not uniformly distributed, but are located within a $\Delta\phi$ interval of 2.5 to π. The $\Delta\phi$ cut is indicated by the vertical line at $\Delta\phi = 2.5$. The distributions are after the object selection with the p_T^l / p_T^{miss} cut applied (see tables 5.2 and 5.4).

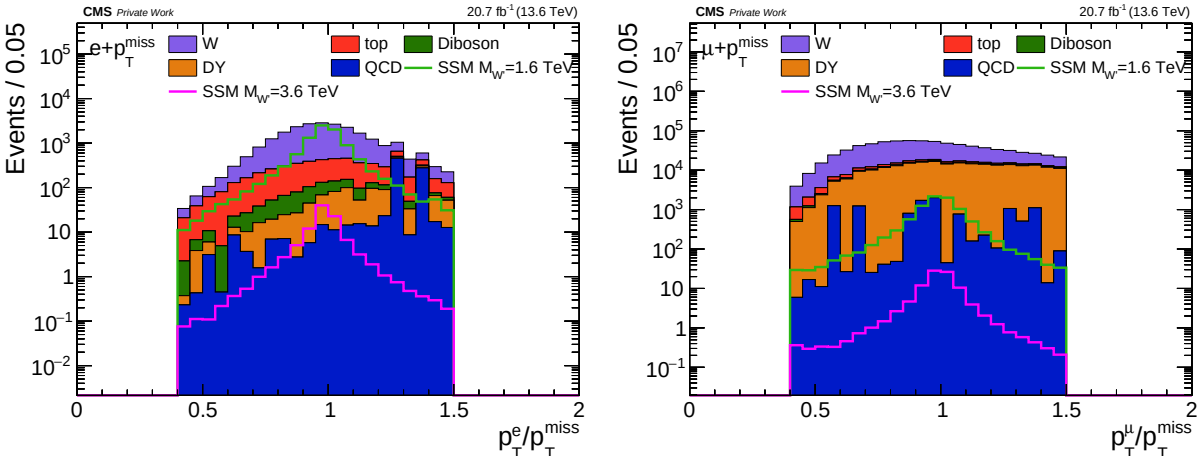

Figure 6.13: Distributions for p_T^l / p_T^{miss} for the electron (left) and muon channel (right). The background contribution in the p_T^l / p_T^{miss} distributions decreased, due to the $\Delta\phi$ cut. The ratio distribution has a sharper peak in both channels than in fig. 6.12, but is especially visible in the electron channel. The distributions are after applying all selection criteria.

7 Preliminary data to background comparison

7.1 Framework and pile-up

The CMS Collaboration has a software framework called CMSSW designed to support the data analysis and simulation needs of the CMS experiment [64]. Two versions of the CMSSW are utilized in this thesis. The first being CMSSW_12_4_10, that is used for creating event displays. The second version CMSSW_10_2_13 is used together with the "Three A Physics Analysis Software" (TAPAS) [65], to submit jobs to the computing grid using the Condor batch system. The analysis framework is written in C++ using ROOT [66], an object-oriented computer program and library developed by CERN for particle physics data analyses.
This section follows the structure of the figures from subsection 6.4. Additionally, is the data shown using black points which have statistical error-bars. The ratio plot, that can be found under each of the included plots, shows the ratio of data to simulated SM background. The ratio plots have a grey band around 0. Its meaning is introduced in the following subsection.
The effect of having multiple interactions per bunch crossing, due to the high instantaneous luminosity (see eq. (3.1)), is called pile-up. This is a result of a high number of protons in each bunch, leading to a mean value of 46 interactions per crossing [15, 67]. Pile-up can be divided into two categories: In-time pileup and Out-of-time pileup. In-time pileup refers to the additional proton-proton collisions that occur within the same bunch crossing as the primary interaction, whereas Out-of-time pileup refers to collisions that occur in bunch crossings preceding or following the bunch crossing containing the primary interaction. These additional interactions can influence the measurement of the primary event due to the finite response time of particle detectors. No official pile-up recommendation is available yet. Therefore, the pile-up was calculated privately [67, 68]. The simulated samples are then reweighted by a factor of

$$w_{PU} = \frac{N_{PV,data}}{N_{PV,MC}} \tag{7.1}$$

to make them comparable to the data. The number of PV per event for each data and MC is denoted as N_{PV}. An official pile-up recommendation and ReReco for the data along with re-processed MC samples would improve the pile-up reweighting. Also adding missing background samples for the on-shell W production and top quark, on top of the available background samples, will further enhance the background modelling.

7.2 Systematic uncertainties

Each scientific experiment has uncertainties, which can be divided into two groups. The first group consists of statistical uncertainties, which can be reduced by multiple measurements. In particle physics experiments, when dealing with event numbers (N), the statistical uncertainty is assumed to be a Poisson error ($\sqrt{N}$). The second group of uncertainties comprises systematic uncertainties, which are intrinsic properties of the experiment itself and cannot be reduced by repeating the measurement. Many uncertainties are not yet available for Run-3. Examples of these include the systematic uncertainties for pile-up, k-factors, and scale factors. The only available systematic uncertainty is currently the luminosity measurement uncertainty.

Luminosity: Following the Run-3 2022 recommendation, a systematic uncertainty of 2.2% is assumed on the luminosity measurement [68].

To evaluate the impact of these uncertainties, the relevant quantity would be shifted by the systematic uncertainty, up and down, with respect to the nominal weight, and the analysis is repeated. The unavailable systematic uncertainties are estimated on the basis of the Run-2 AN [49]. A short overview of the systematic uncertainties that should be considered in the analyses as soon as they become available, can be seen below. The uncertainties are summarized into group. The following gives the total uncertainty of the respective, followed by a description of the specific uncertainties inside that group.
The uncertainty on the unclustered energy is assumed to be 10% and uncertainty on the Jet Energy Corrections (JERCs) amounts to 5%. This results in a total estimated uncertainty of 15% for this group.

Jet Energy Scale: The measured jet energy has an uncertainty, which is accounted for by the Jet Energy Correction (JEC). It is provided by the JERC group and is η and p_T dependent. This uncertainty is not only important for the b-tagging in the muon channel but also propagates onto the p_T^{miss} quantity, as it is calculated as the negative sum of all energies in an event.

Jet Energy Resolution: The Jet Energy Resolution (JER) depends on the same quantities as JEC. Details on the JEC and JER calculations and values can be found in [69, 70, 71].

Unclustered Energy: The unclustered energy comes from energy that is not connected to the reconstructed physics objects. The quadratic sum of the uncertainties on the quantities that are used to calculate the PF MET is used as the p_T^{miss} uncertainty.

The following group encompasses the object related uncertainties. Similar to Run-2, a total uncertainty of 5% is assumed on this group, containing the lepton energy scale and scale factor uncertainty. Additionally, the scale factors are currently not available yet.

Electron Energy Scale: This uncertainty is calculated by comparing data around the Z boson peak with simulations. Two uncertainty values are separately applied to the barrel and endcap region.

Muon Energy Scale: This uncertainty is calculated by the same method as the electron energy scale, together with a curvature study of the muon tracks in different η and ϕ regions [72].

Scale Factors: The scale factor uncertainty for the triggers in both channels is calculated using the Tag&Probe method with orthogonal datasets [73].

This group consists of a 5% uncertainty on the pile-up, 15% on the k-factor and 10% on the PDF+α_S, resulting in a total estimated uncertainty of 30%.

PDF+α_S uncertainty: The PDF and the strong coupling constant affect the amount of momentum carried by each quark and gluon inside a proton. The uncertainty in this propagates to the theoretical MC cross sections and affects the background normalization.

Pile-up: The reweighting of events in simulation is based on the pile-up differences between measured data and simulation. The uncertainty on the pile-up is evaluated by applying the pile-up reweighting on a kinematic distribution, using a minimum bias cross section and its associated uncertainty. This is followed by calculating the difference when shifting it both ways [74].

k-factor: The uncertainty on the k-factor originates from two different methods when combining QCD with electroweak cross sections. There are two approaches resulting in different values for the k-factor, an additive and a factorized approach [49]. The difference between both fits for the k-factor is taken as the uncertainty.

The total uncertainty, represented by the grey band in each distribution, is calculated as a square root of the sum of squares from three uncertainties: the statistical uncertainty, the estimated 50% uncertainty, and the 2.2% luminosity uncertainty.

7.3 Kinematic distributions

To identify deviations from the Standard Model background, we compare the acquired data with the simulated SM background for various distributions. The background samples have been introduced in sec. 4 and are given in table A.1. The distributions typically include the ϕ, and η distributions. The resulting distributions after the selection for ϕ are provided in fig. 7.1 for both the electron and muon channel, respectively. Both channels show the expected azimuthal isotropy in the SM background, as there is no preferred decay direction. The data shows a modulation in both channels originating from asymmetries in the CMS detector, which were also present in Run-2 AN figures [49]. A re-processing of the MC samples will improve the modelling of the detector asymmetries. Taking into consideration the impact of the missing samples for the electron channel, the data-to-MC comparison is acceptable. However, in the muon channel, a discrepancy exists between the data and MC, therefore, the ratio plot was produced with different ranges. This is primarily attributed to the lower transverse momentum threshold, which leads to the acceptance of more background events in the low-mass region. These low-energy events stem from the on-shell W peak. Subsequently, this leads to fewer background events compared to data, as the samples for the on-shell W peak are not yet available. The statistical uncertainties in the y-direction are relatively small, and are therefore, less visible in the plots.
The η distributions, shown in fig. 7.2, exhibit fewer events in the simulations compared to the data. In the electron channel, there is a shortage of high-pseudorapidity events, leading to a discrepancy in the endcap region between the data and MC simulations. In the muon channel, there is also a deficiency of high p_T events, but the impact of the missing on-shell W events is particularly evident, resulting in fewer events in the central region. Both distributions are centered around 0, indicating that the majority of events have roughly $p_T < 500\,\text{GeV}$. The ratio plot of the η distribution for the muon channel has different y-axis range in comparison to electron channel for the same reasons stated above. The statistical uncertainties along the y-axis cannot be seen, because they are, like in fig. 7.1, not large enough. The cut between the barrel and endcap region can be seen around $\eta \approx \pm 1.5$ for the electron channel. Most events are within the uncertainty band in the electron channel indicating correct background modelling. If the muon channel had a higher trigger threshold, the distributions would show similar behaviour. Because the statistical uncertainties along the y-axis are so small, they cannot be seen from the plot.

7.4 Final distributions

In fig. 7.4 and fig. 7.3, the distributions of the missing transverse momentum (p_T^{miss}) and lepton transverse momentum (p_T^l) are presented. The distributions are blinded for $p_T > 750\,\text{GeV}$. The region below the blinding is called the control region, whilst the region above it is called the signal region, as one expects the W' boson signal at high energies. Both channels show good

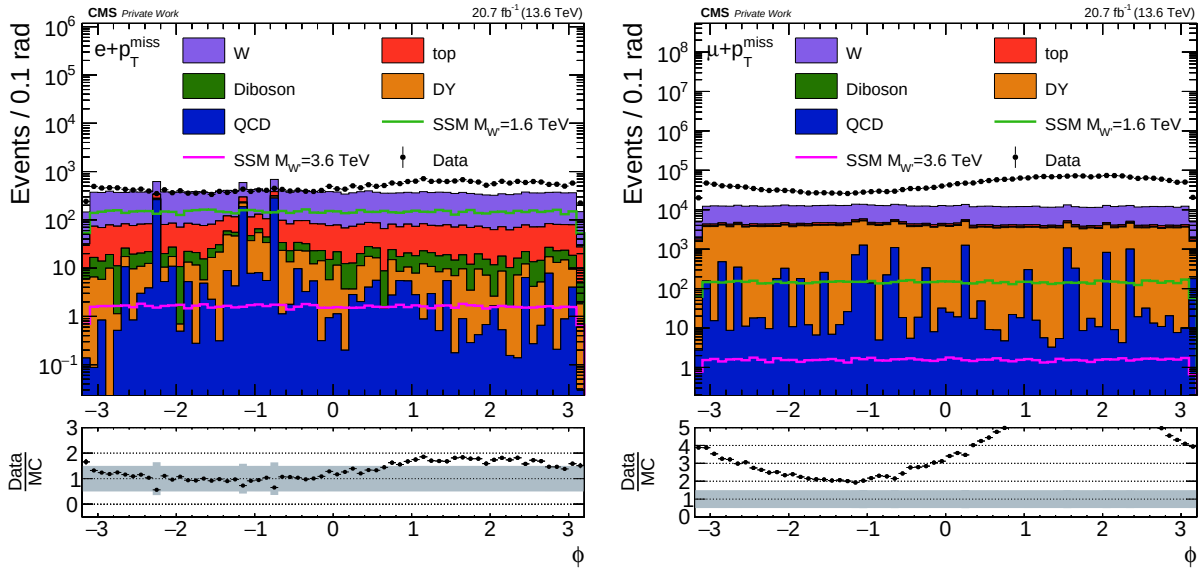

Figure 7.1: The ϕ distributions for both the electron (left) and muon channels (right). Both distributions exhibit azimuthal isotropy in the SM background, but there is a noticeable asymmetry in the data for both channels. This discrepancy, stemming from an asymmetry in the detector has been addressed in the Run-2 AN [49]. A re-processing of the MC samples will improve the detector modelling. The absence of the W+Jets sample has a particularly pronounced impact in the muon channel, resulting in an unequal number of events. Therefore, the ratio plot for the muon channel has a range from 0 to 5. The statistical uncertainties in the y-direction are not large enough and can not be seen.

agreement between data and simulation in both figures. The impact of the missing samples is visible in the first and second bins, especially in the muon channel. Most of the events are concentrated in the first bins, because the on-shell W+Jets events have a reconstructed mass until $p_T^l \approx 150\,\text{GeV}$. This results in high statistics in these low-energy bins. However, except for the disagreement in the first bins, both channels exhibit similar behavior and have a good data to MC ratio. Both channels have similar background contribution from the W, Drell-Yan, and diboson processes. The muon channel has more contribution from the QCD multijet background for the high-mass region and from the top quark in the low-mass region.

The final distribution for the main discriminating variable, the transverse mass, after applying all selection criteria and the pile-up reweighting is given in fig. 7.5. The transverse mass distribution is blinded for $M_T > 1500\,\text{GeV}$. The region below 1500 GeV is again called the control region, with the signal region being blinded. In both channels, there is an overfluctuation in the first mass bins, which was also visible in the transverse momentum histograms. However, the other data points show good agreement with the simulated background. The number of events decreases for the higher reconstructed transverse mass region.

The electron channel exhibits less contribution from the QCD multijet and top quark background. The most dominant background process is the W boson decay. In the muon channel, the data point in the 1400 GeV bin lies outside one standard deviation as indicated by the uncertainty band. The error bar also does not touch the band. However, this visible overfluctuation is within $1.76\,\sigma$. This was calculated with the formula for the compatibility of two data points

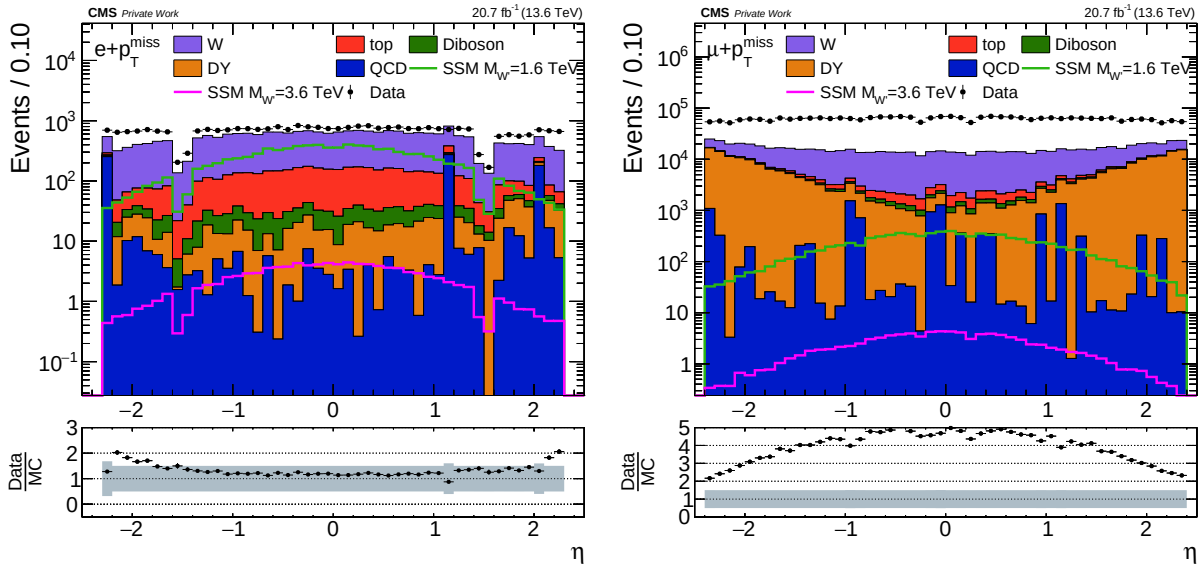

Figure 7.2: The η distributions for the electron (left) and muon channels (right). Both data distributions are centered around 0, as expected. However, there are fewer MC events compared to the data in both channels. This discrepancy can be attributed to the absence of the W+Jets sample in the simulations. In the electron channel, this absence affects the high-energy region, leading to a deficit of events. In contrast, in the muon channel, where on-shell W production is missing, events are notably absent, especially in the low-energy region. Nevertheless, the background distributions still exhibit the expected behavior.

with their respective uncertainties (see eq. (7.2)).

$$\text{deviation}/\sigma = \frac{|N_{data} - N_{MC}|}{\sqrt{\sigma^2_{N_{data}} + \sigma^2_{N_{MC}}}} \tag{7.2}$$

The $N_{data/MC}$ are the number of data or background events, respectively. The $\sigma_{N_{data/MC}}$ are their corresponding standard deviations, that encompass the statistical and systematic uncertainties. Therefore, this can be explained as originating from statistical fluctuations. It is possible that this could be corrected by including more background samples and, consequently, more events for higher reconstructed transverse masses.
In the electron channel, the highest M_T event below the blinding has an electron with a p_T of 774 GeV and a p_T^{miss} of 726 GeV. The difference in ϕ is 176.3°, which is approximately equal to 3.077 rad, as expected from the back-to-back kinematics. The event display of this $M_T = 1498$ GeV event is shown in fig. 7.6. It was recorded on November 27, 2022, during era G, with the run (event) number 362439 (1140043708) and in lumi section 529.
In the muon channel, the highest M_T event below the blinding features an electron with a p_T of 723 GeV and a p_T^{miss} of 751 GeV. The difference in ϕ is 179.3°, which is almost perfectly back-to-back, approximately equal to 3.129 rad. The event display of this $M_T = 1473$ GeV event is shown in fig. 7.7. It was detected on October 15, 2022, during era F, with the run (event) number 360393 (134873575) and in lumi section 66.

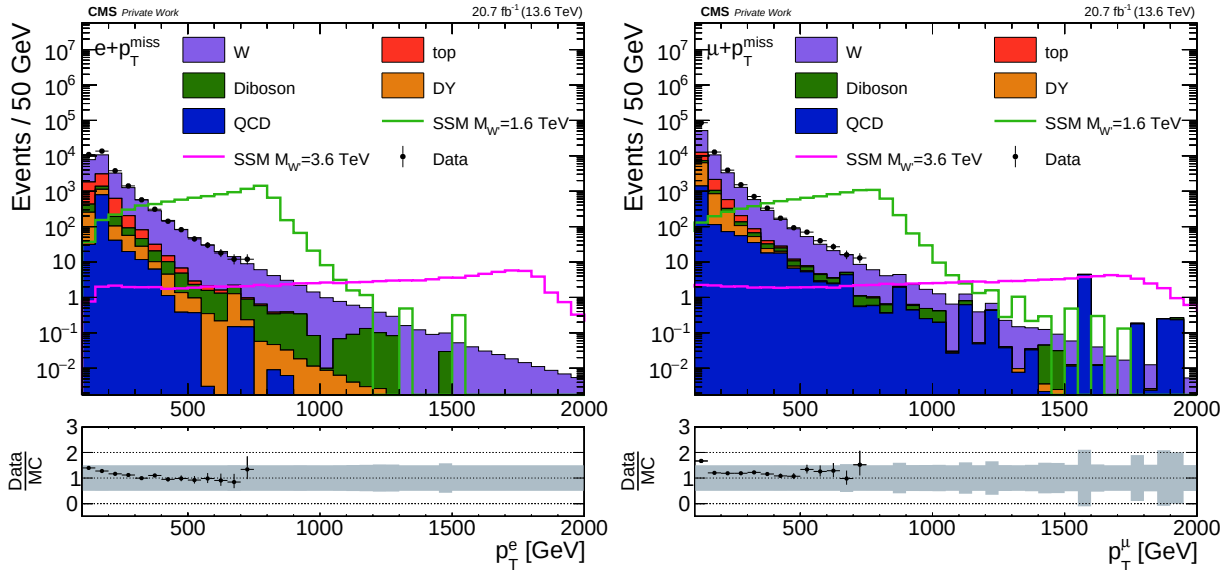

Figure 7.3: The p_T^l distributions for the electron (left) and muon channel (right). Both channels show good agreement between data to MC. The impact of the missing W+Jets sample is visible mainly in the first two bins. The muon channel has a higher number of events in the first bin due to the lower momentum threshold of 53 GeV. This results in the acceptance of the on-shell W peak at 80.38 GeV, whereas the electron channel has a momentum threshold of 130 GeV. The distributions are blinded for $p_T > 750$ GeV. The data to background ratio shows that the background was modelled correctly in the control region below the blinding.

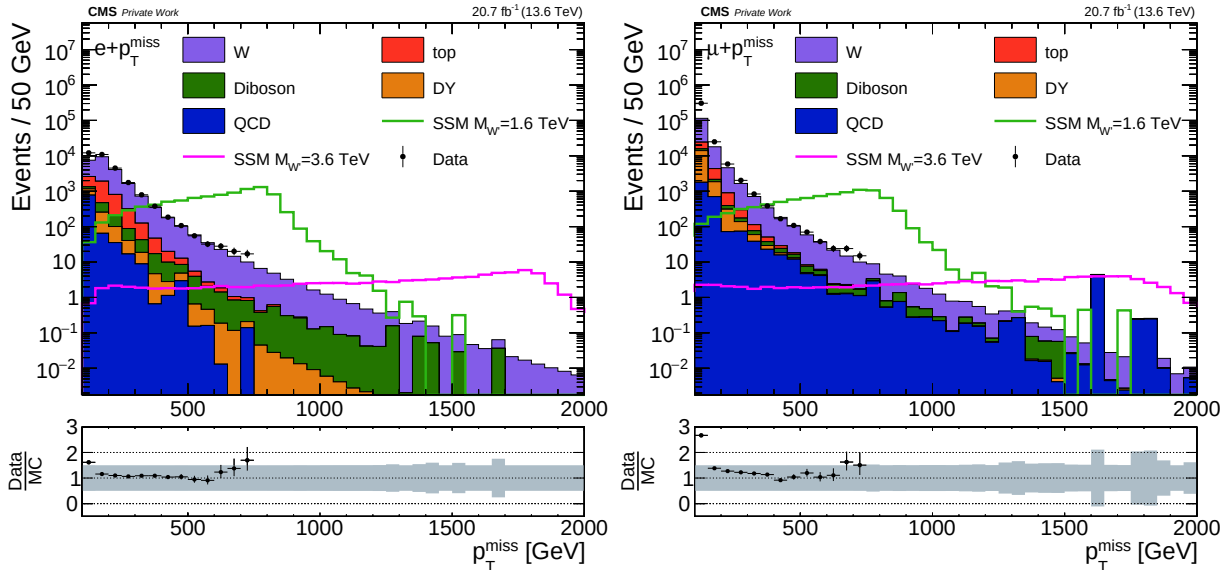

Figure 7.4: The p_T^{miss} distributions for the electron (left) and muon channel (right). The p_T^{miss} distributions are similar to the p_T^l distributions and also show good agreement in data to background with the exception of the first two bins. The distributions are blinded for $p_T > 750$ GeV. One expects the missing transverse momentum and the lepton momentum distributions to show similar behaviour, which is given when comparing this to fig. 7.3.

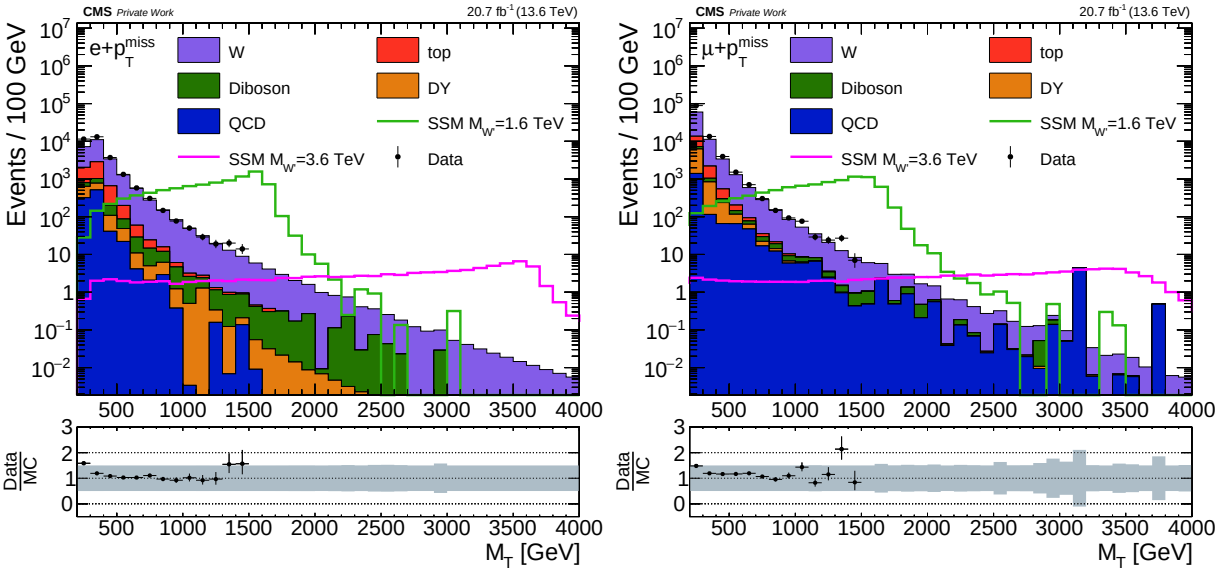

Figure 7.5: In this figure, the M_T distributions for the electron (left) and muon channels (right) are presented. As previously mentioned, the discrepancy in the first bin can be attributed to the absence of the W+Jets sample. Apart from this, there is no significant deviation observed in the control region. Both channels exhibit good agreement between the data and simulations. It is worth noting that the distributions are blinded for $M_T > 1500\,\text{GeV}$.

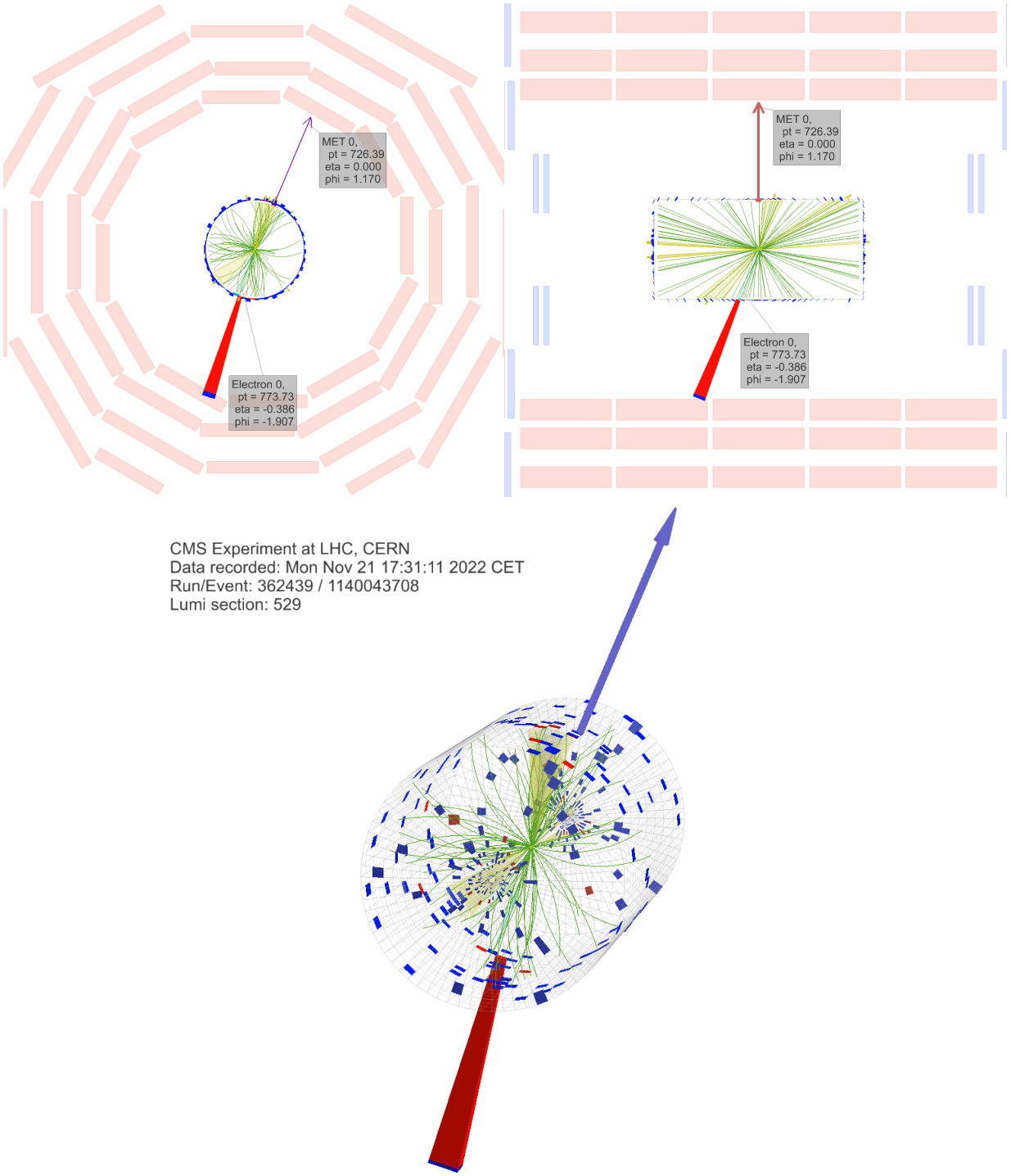

Figure 7.6: Event display of the highest M_T event below 1500 GeV in the electron channel at $M_T = 1498$ GeV. On the top left is a view in the $\rho - \phi-$ and on the top right in the $\rho - z-$plane. On the bottom is a three dimensional view of the event. Jets are colored yellow and the green lines are paths reconstructed from the inner tracker. The track of the electron is shown using a turquoise color. The energy deposit in the ECAL is shown with the red cone, whereas the missing transverse momentum is highlighted with a blue arrow.

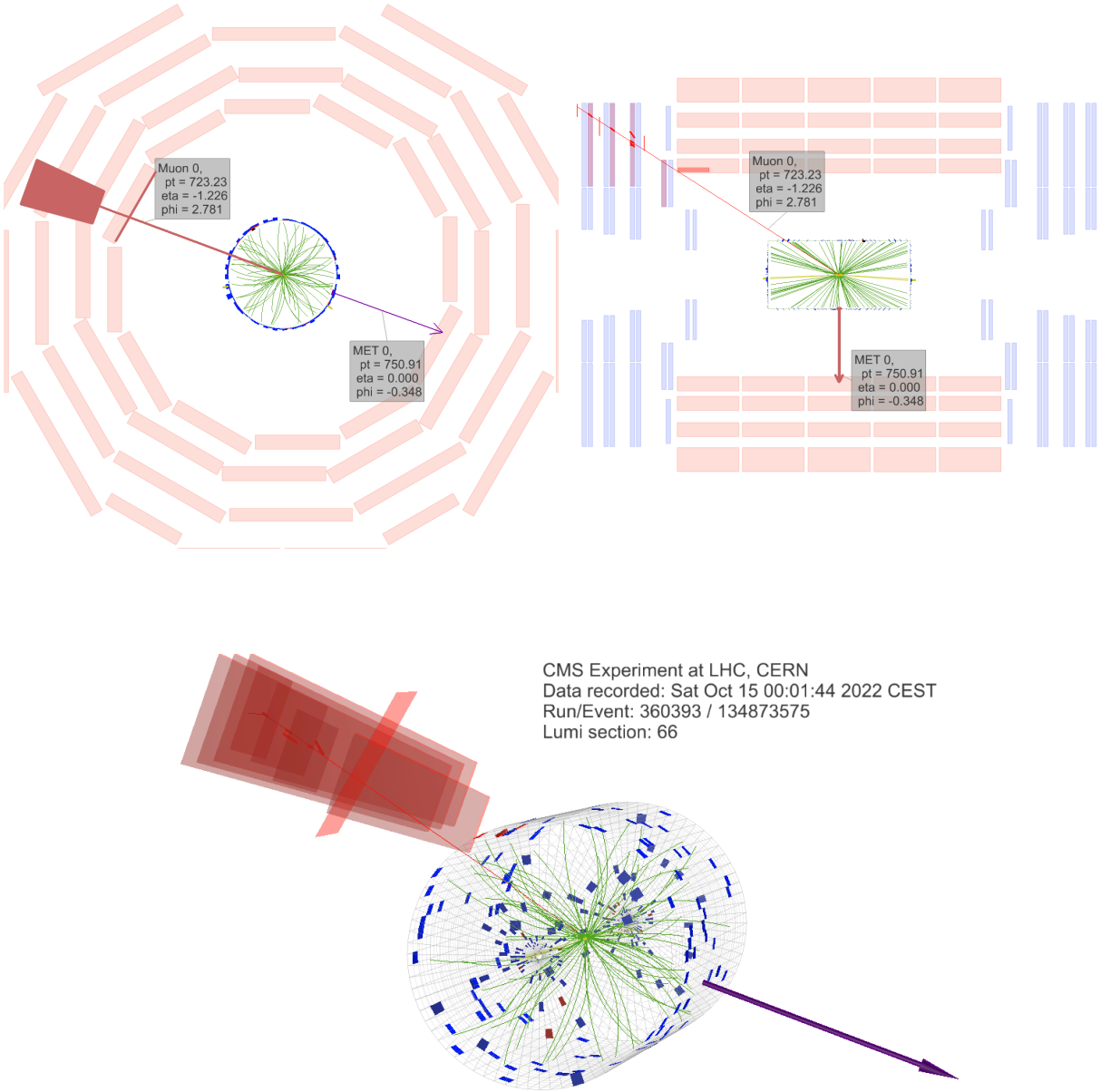

Figure 7.7: Event display of the highest M_T event below 1500 GeV in the muon channel at $M_T = 1473$ GeV. The path of the muon is shown using a red line, whereas the missing transverse momentum is highlighted with a purple arrow. The hits in the muon chambers are also visible in the $\rho - z$ view.

8 Summary

The analysis on the search for a new heavy W′ vector boson has been presented in this thesis. The focus of the performed analysis is on the final state with a lepton (electron or muon) and missing transverse momentum. A back-to-back topology between these two objects and balance in their respective momenta has been required. This analysis has been performed for the eras F and G of the Run-3 dataset recorded by the CMS collaboration in 2022, at an unprecedented center-of-mass energy of 13.6 TeV in proton-proton collisions. The analysed dataset corresponds to an integrated luminosity of 20.7 fb^{-1}. The benchmark interpretation is performed in terms of Sequential Standard Model. The analysis strategy mainly follows the Run-2 studies, however, various modifications have been applied. The analysis specific event selection and reconstruction has been introduced in great detail in this thesis.

First, signal studies have been conducted and described in this thesis. The signal studies encompass a new evaluation of the signal efficiencies in Run-3 and a study on the impact of varying the coupling ratio. Furthermore, the impact of the kinematic selection criteria have been presented. Events in the muon channel are triggered with a combination of three triggers. The HLT_Mu50, HLT_HighPtTkMu100, and HLT_CascadeMu100, which is the most efficient way of event selection for the final states with high-p_T muon. As for the electron channel, in addition to the single photon trigger that has been used for the Run-2 analysis, the Ele115 trigger has been added. Given that the Ele115 trigger has a lower transverse momentum threshold, this results in the extension of the low mass reach from $p_T^e = 240\,\text{GeV}$ to $p_T^e = 130\,\text{GeV}$. Subsequently, lowered threshold in the electron channel makes it possible to combine the results with the muon channel in future.

The signal efficiency in both channels has increased in the low- and high-mass region due to the higher center-of-mass energy for a theoretical, TeV scale, vector boson. Due to the newly added Ele115 trigger, the signal efficiency in the electron channel became comparable to the signal efficiency in the muon channel. It recovers the on-shell peak events for low-mass samples and off-shell events for high-mass samples. This has also increased the efficiency in the electron channel from 72.1% to 76.6%. The signal efficiency in the muon channel can be improved once the official b-tagging recommendations become available.

The study on the coupling ratios showed that an increase of the coupling ratio of the W′ boson results in a higher off-shell production of the vector boson. The decay width Γ and the likelihood of a process involving a W′ boson increases. When decreasing the coupling ratio, Γ and the likelihood of a process involving a W′ boson decreases. This results in mainly on-shell produced W′ bosons at high energies, as expected.

Also, the impact of the kinematic selection on the Standard Model background and signal distributions have been presented. The kinematic selection reduces the background contribution and improves the extraction of the signal in the high-mass region. A revision of the kinematic selection criteria can further improve the signal efficiency.

Additionally, a preliminary data to background comparison has been presented. The distribution for the main discriminating variable, the reconstructed transverse mass, is blinded for $M_T > 1500\,\text{GeV}$. The resolution of the M_T distribution is 100 GeV per mass bin. The unblinded data in the control region shows no significant deviation from the simulated background. The only overfluctuation is seen in the muon channel with a local significance of less than 1.76σ.

A Cross section tables and sample lists

Table A.1: Cross sections for the used simulated MC background samples. Taken from [44]

Background		σ [pb]	Order	Generator
W off-shell	WtoENu_M-100to200	177.4	LO	pythia8
	WtoENu_M-200to500	7.395	LO	pythia8
	WtoENu_M-500to1000	0.2553	LO	pythia8
	WtoENu_M-1000to2000	0.01593	LO	pythia8
	WtoENu_M-2000to3000	4.77e-04	LO	pythia8
	WtoENu_M-3000to4000	3.16e-05	LO	pythia8
	WtoENu_M-4000to5000	3.03e-06	LO	pythia8
	WtoENu_M-5000to6000	4.03e-07	LO	pythia8
	WtoENu_M-6000	1.06e-07	LO	pythia8
W off-shell	WtoMuNu_M-100to200	175.1	LO	pythia8
	WtoMuNu_M-200to500	7.423	LO	pythia8
	WtoMuNu_M-500to1000	0.254	LO	pythia8
	WtoMuNu_M-1000to2000	0.01586	LO	pythia8
	WtoMuNu_M-2000to3000	4.68e-04	LO	pythia8
	WtoMuNu_M-3000to4000	3.20e-05	LO	pythia8
	WtoMuNu_M-4000to5000	2.95e-06	LO	pythia8
	WtoMuNu_M-5000to6000	4.03e-07	LO	pythia8
	WtoMuNu_M-6000	1.05e-07	LO	pythia8
W off-shell	WtoTauNu_M-100to200	174.7	LO	pythia8-tauola
	WtoTauNu_M-200to500	7.485	LO	pythia8-tauola
	WtoTauNu_M-500to1000	0.2479	LO	pythia8-tauola
	WtoTauNu_M-1000to2000	0.01584	LO	pythia8-tauola
	WtoTauNu_M-2000to3000	4.82e-04	LO	pythia8-tauola
	WtoTauNu_M-3000to4000	3.11e-05	LO	pythia8-tauola
	WtoTauNu_M-4000to5000	2.97e-06	LO	pythia8-tauola
	WtoTauNu_M-5000to6000	4.09e-07	LO	pythia8-tauola
	WtoTauNu_M-6000	1.01e-07	LO	pythia8-tauola
Diboson	WW	80.23	LO	pythia8
	WZ	29.1	LO	pythia8
	ZZ	12.75	LO	pythia8
	ZZto2L2Nu	1.1341	NNLO	powheg-pythia8
Top	TTto2L2Nu	96.9	NLO	powheg-pythia8
DY	DYto2L-2Jets_MLL-50	6688	NLO	aMC@NLO-FXFX-pythia8
	DYto2E_MLL-50to120	2219	NLO	powheg-pythia8
	DYto2E_MLL-120to200	21.65	NLO	powheg-pythia8
	DYto2E_MLL-200to400	3.058	NLO	powheg-pythia8
	DYto2E_MLL-400to800	2.691e-01	NLO	powheg-pythia8
	DYto2E_MLL-800to1500	1.915e-02	NLO	powheg-pythia8
	DYto2E_MLL-1500to2500	1.111e-03	NLO	powheg-pythia8
	DYto2E_MLL-2500to4000	5.949e-05	NLO	powheg-pythia8
	DYto2E_MLL-4000to6000	1.558e-06	NLO	powheg-pythia8

Table A.1 – Continued

Background		σ [pb]	Order	Generator
DY	DYto2Mu_MLL-50to120	2219	NLO	powheg-pythia8
	DYto2Mu_MLL-120to200	21.65	NLO	powheg-pythia8
	DYto2Mu_MLL-200to400	3.058	NLO	powheg-pythia8
	DYto2Mu_MLL-400to800	2.691e-01	NLO	powheg-pythia8
	DYto2Mu_MLL-800to1500	1.915e-02	NLO	powheg-pythia8
	DYto2Mu_MLL-1500to2500	1.111e-03	NLO	powheg-pythia8
	DYto2Mu_MLL-2500to4000	5.949e-05	NLO	powheg-pythia8
	DYto2Mu_MLL-4000to6000	1.558e-06	NLO	powheg-pythia8
QCD	QCD_PT-120to170	445800	LO	pythia8
	QCD_PT-170to300	113700	LO	pythia8
	QCD_PT-300to470	7589	LO	pythia8
	QCD_PT-470to600	626.4	LO	pythia8
	QCD_PT-600to800	178.6	LO	pythia8
	QCD_PT-800to1000	30.7	LO	pythia8
	QCD_PT-1000to1400	8.92	LO	pythia8
	QCD_PT-1400to1800	0.8103	LO	pythia8
	QCD_PT-1800to2400	0.1148	LO	pythia8
	QCD_PT-2400to3200	0.007542	LO	pythia8

B More signal sample distributions

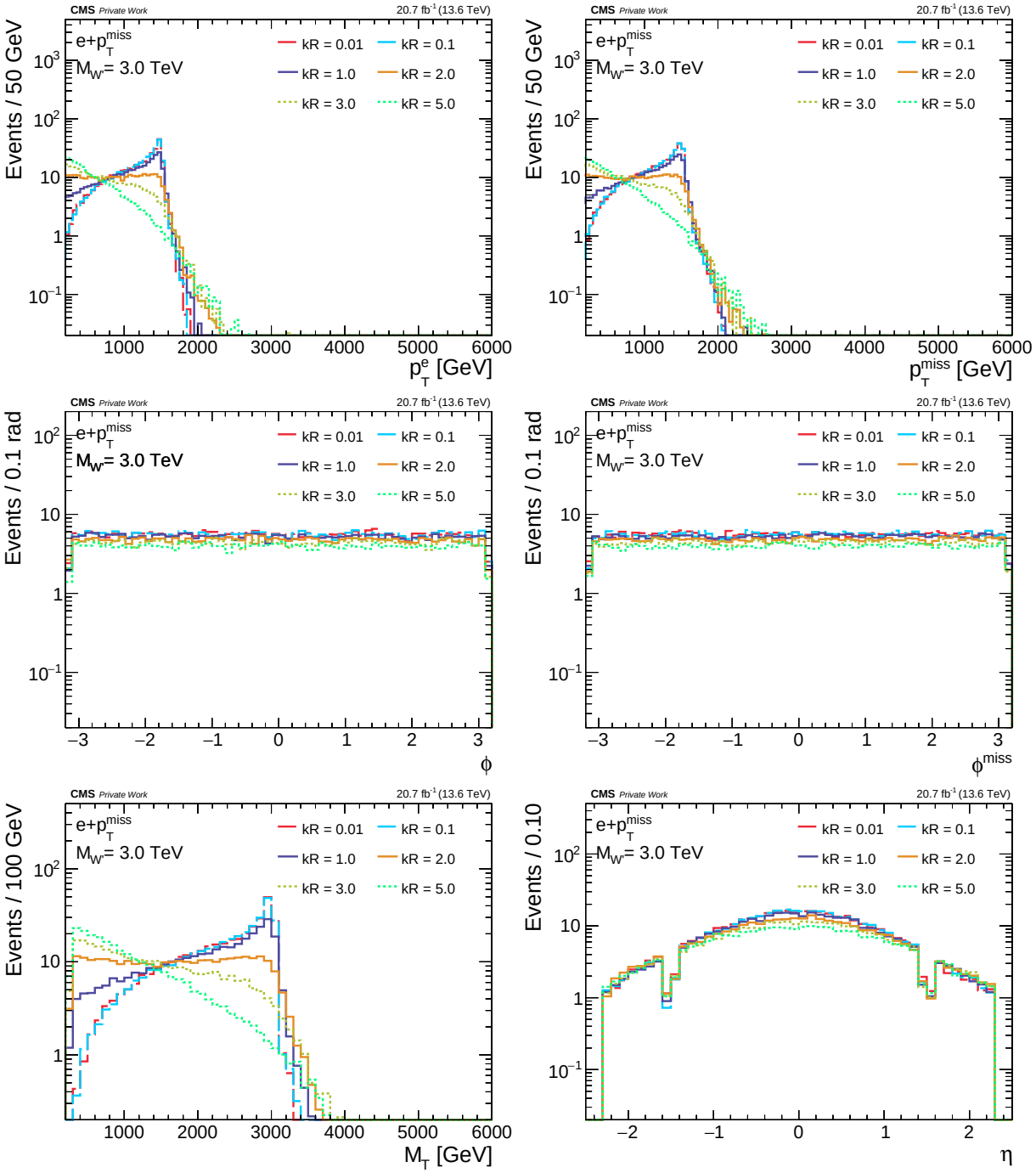

Figure B.1: Distributions for p_T (top left), p_T^{miss} (top right), ϕ (middle left), ϕ^{miss} (middle right), M_T (bottom left), and η (bottom right) at a W′ signal sample mass of 3000 GeV in the electron channel with 6 different couplings.

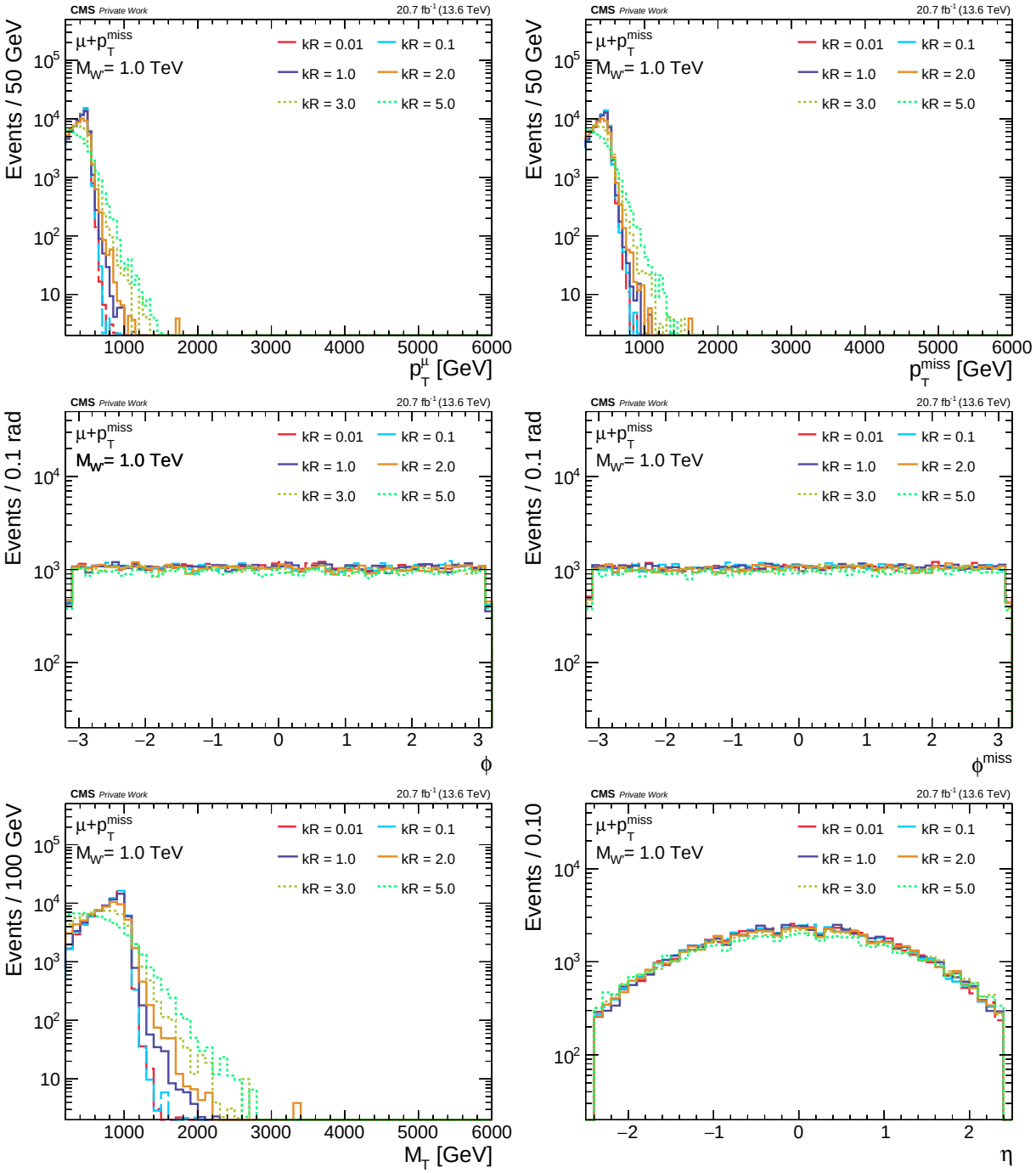

Figure B.2: Distributions for p_T (top left), p_T^{miss} (top right), ϕ (middle left), ϕ^{miss} (middle right), M_T (bottom left), and η (bottom right) at a W′ signal sample mass of 1000 GeV in the muon channel with 6 different couplings.

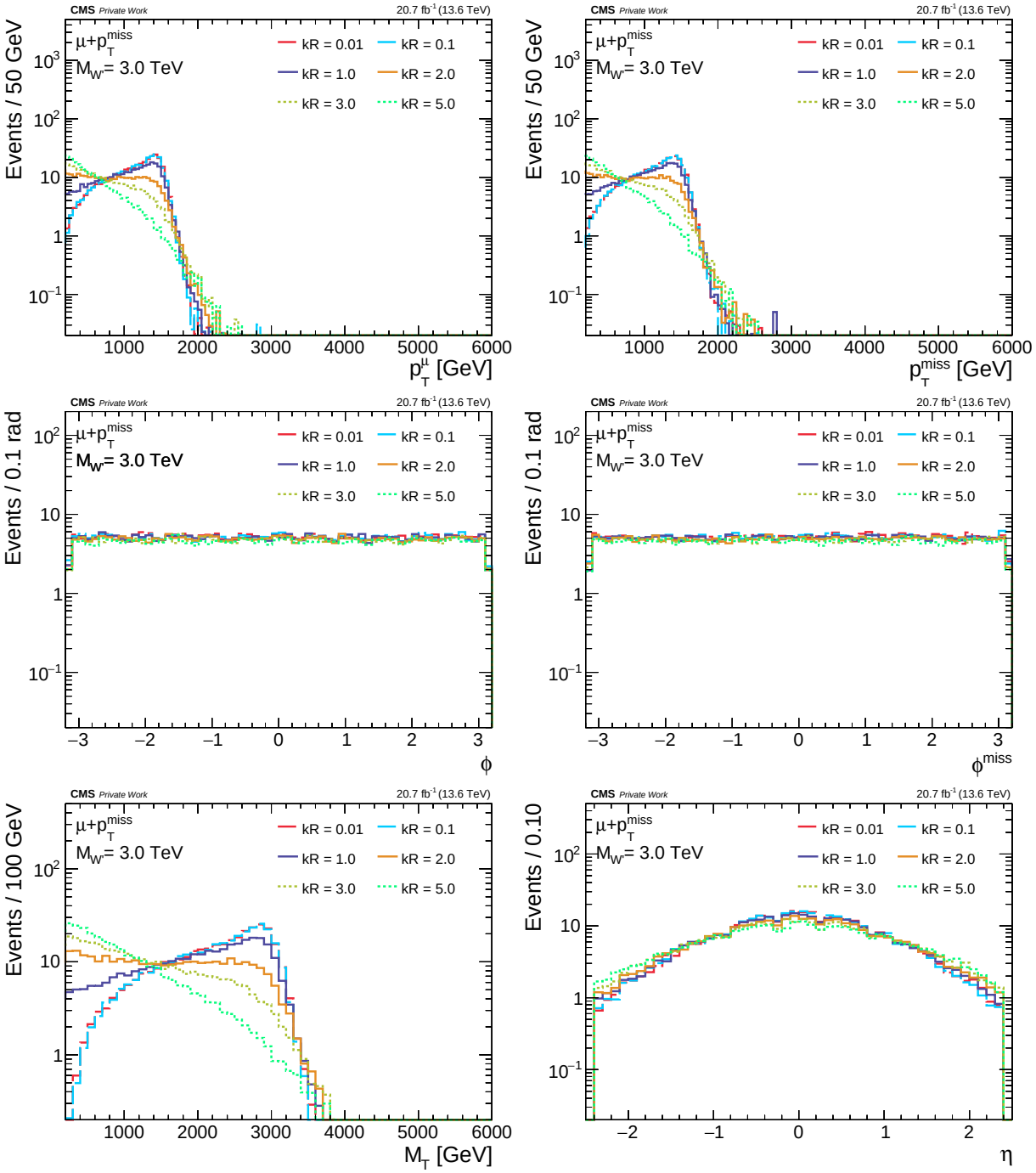

Figure B.3: Distributions for p_T (top left), p_T^{miss} (top right), ϕ (middle left), ϕ^{miss} (middle right), M_T (bottom left), and η (bottom right) at a W′ signal sample mass of 3000 GeV in the muon channel with 6 different couplings.

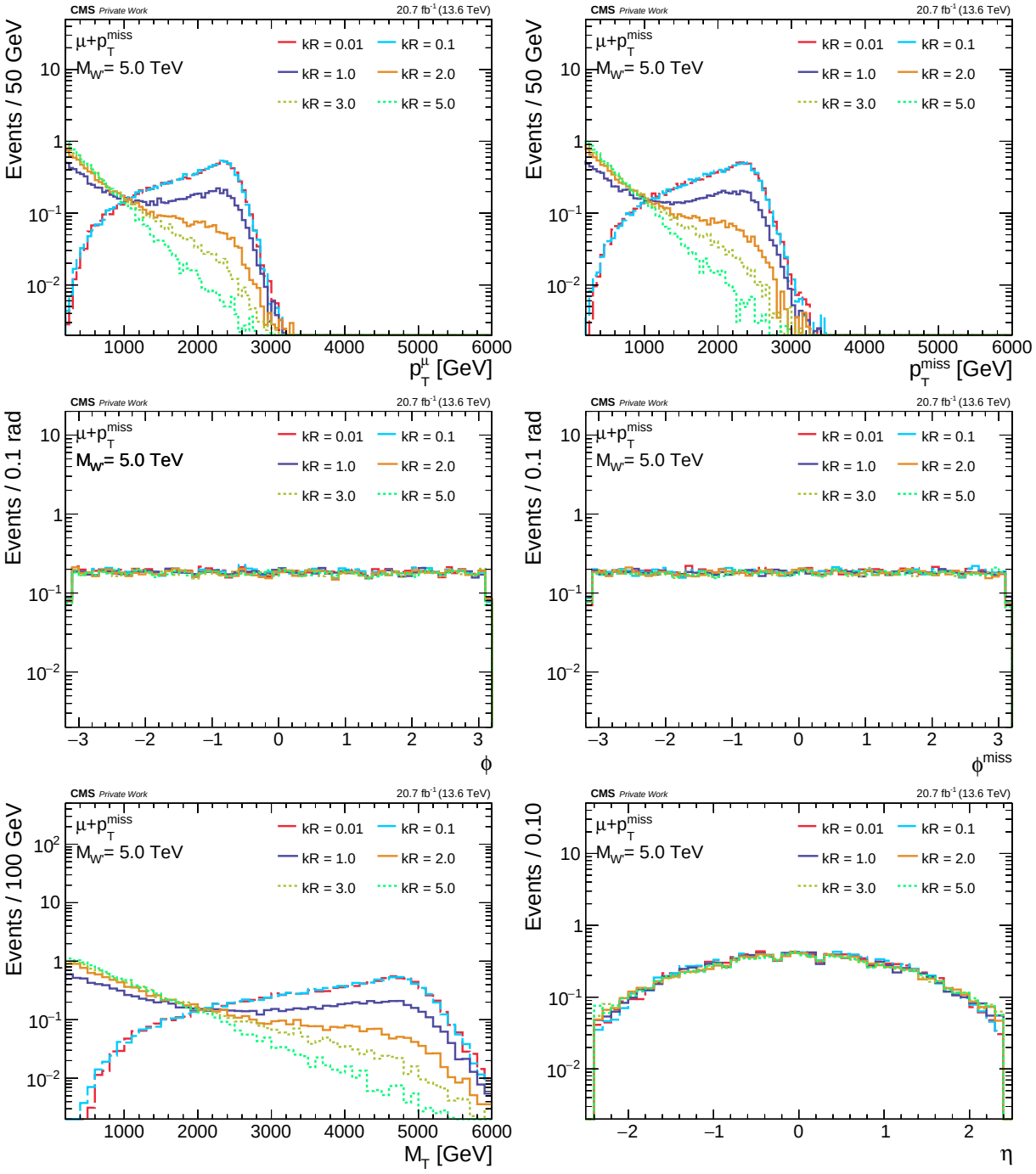

Figure B.4: Distributions for p_T (top left), p_T^{miss} (top right), ϕ (middle left), ϕ^{miss} (middle right), M_T (bottom left), and η (bottom right) at a W′ signal sample mass of 5000 GeV in the muon channel with 6 different couplings.

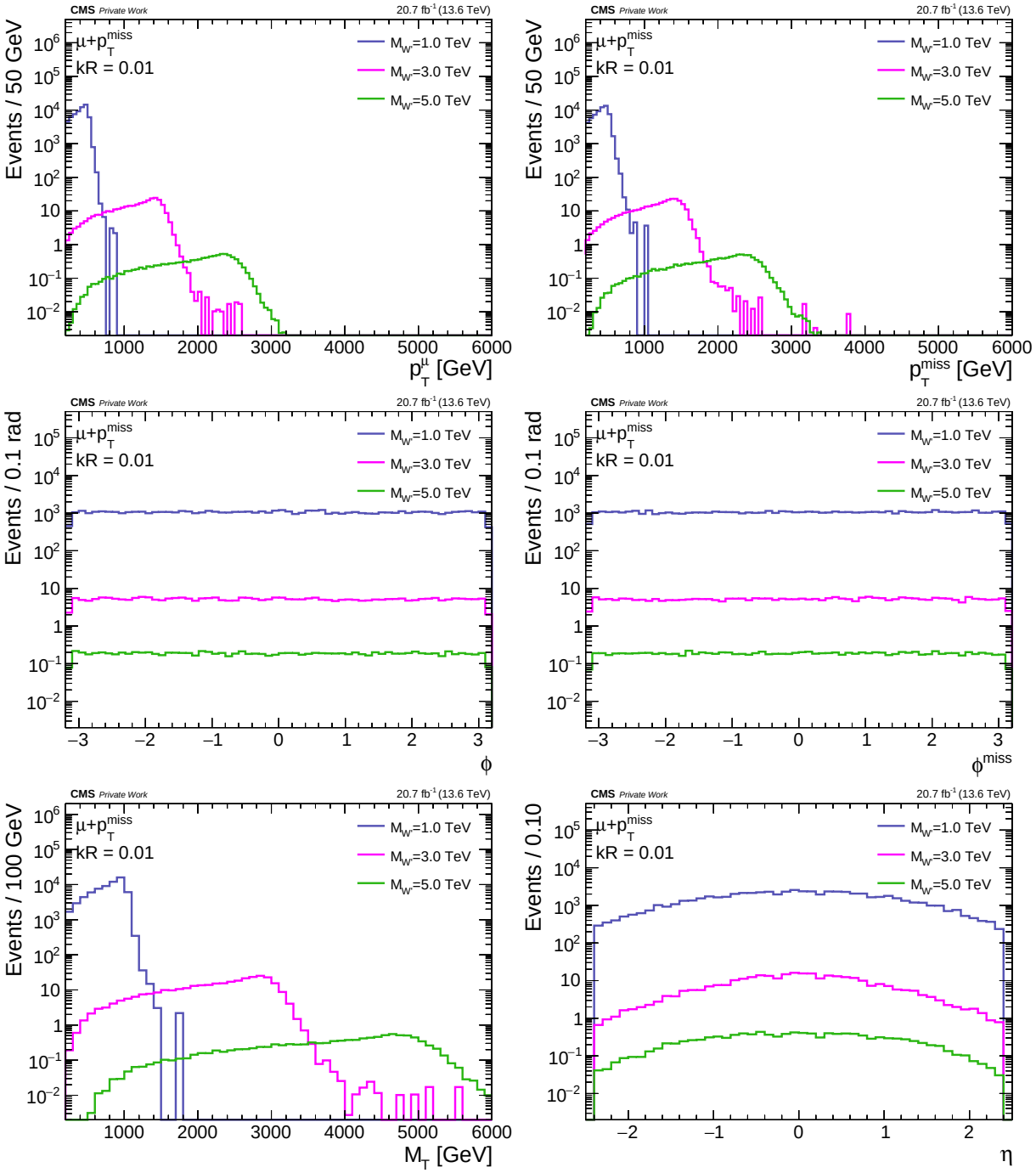

Figure B.5: Distributions for p_T (top left), p_T^{miss} (top right), ϕ (middle left), ϕ^{miss} (middle right), M_T (bottom left), and η (bottom right) at a coupling of 0.01 in the muon channel with 3 different W' signal sample masses (1000 GeV, 3000 GeV, and 5000 GeV).

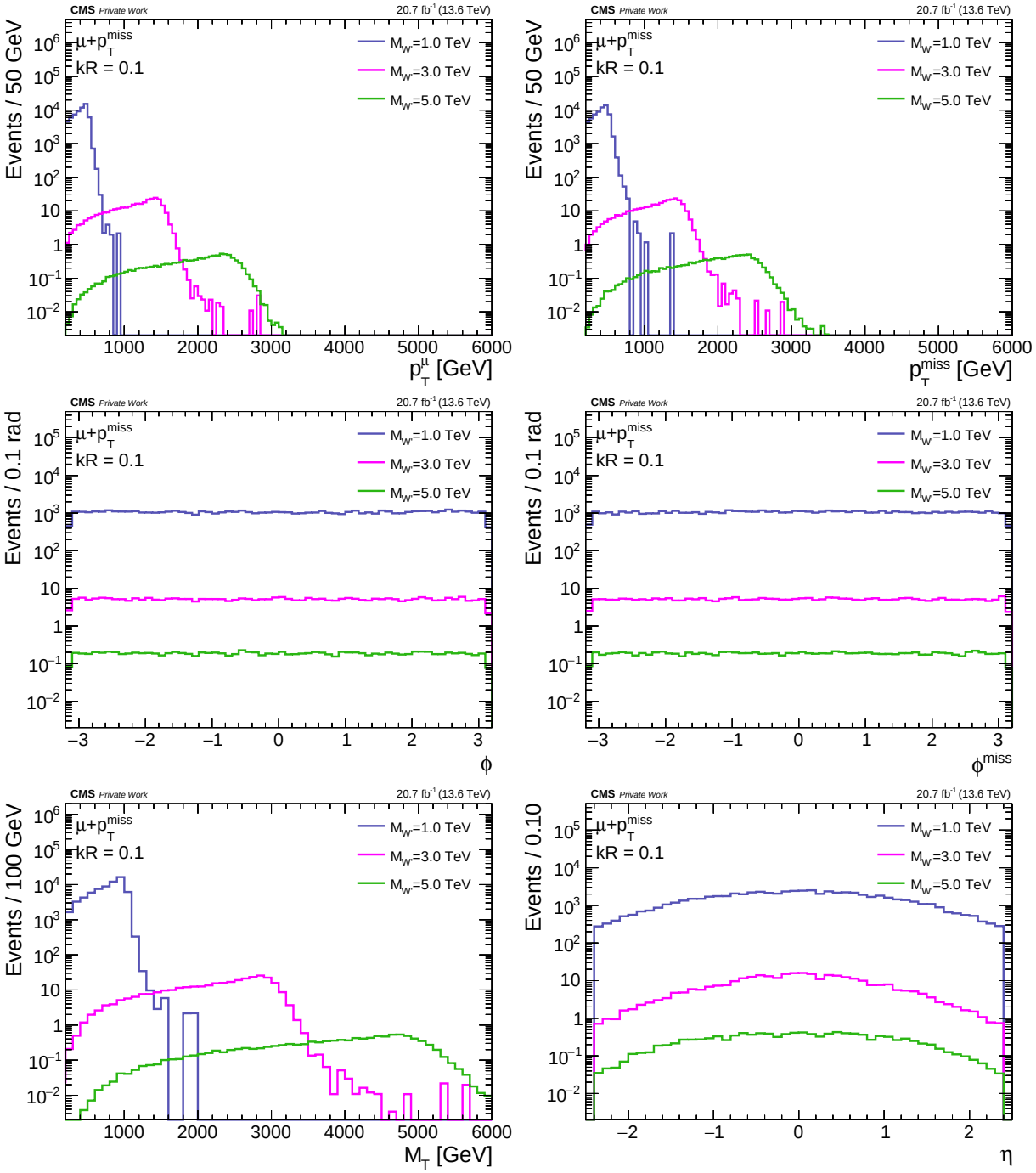

Figure B.6: Distributions for p_T (top left), p_T^{miss} (top right), ϕ (middle left), ϕ^{miss} (middle right), M_T (bottom left), and η (bottom right) at a coupling of 0.1 in the muon channel with 3 different W' signal sample masses (1000 GeV, 3000 GeV, and 5000 GeV).

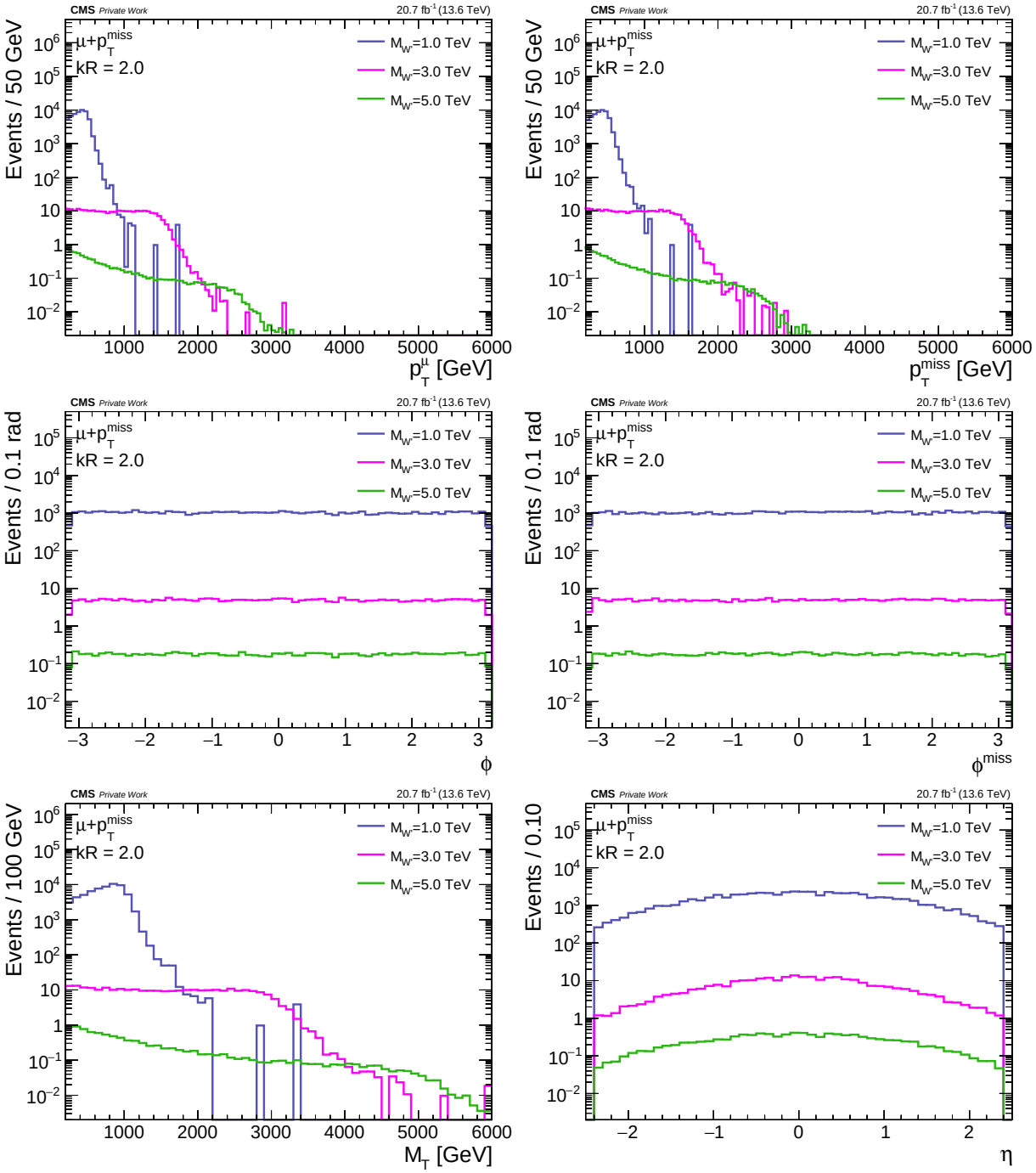

Figure B.7: Distributions for p_T (top left), p_T^{miss} (top right), ϕ (middle left), ϕ^{miss} (middle right), M_T (bottom left), and η (bottom right) at a coupling of 2.0 in the muon channel with 3 different W' signal sample masses (1000 GeV, 3000 GeV, and 5000 GeV).

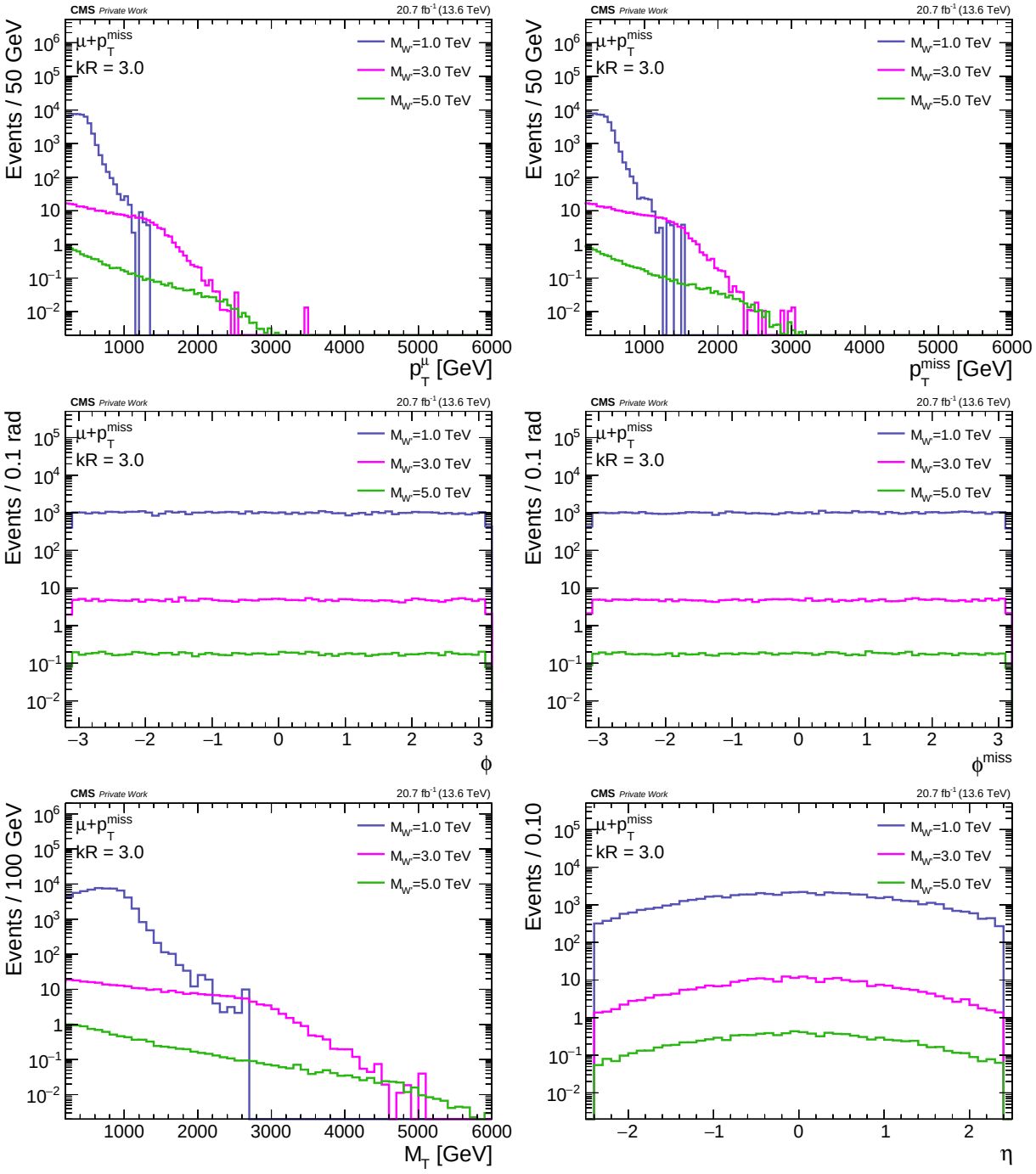

Figure B.8: Distributions for p_T (top left), p_T^{miss} (top right), ϕ (middle left), ϕ^{miss} (middle right), M_T (bottom left), and η (bottom right) at a coupling of 3.0 in the muon channel with 3 different W' signal sample masses (1000 GeV, 3000 GeV, and 5000 GeV).

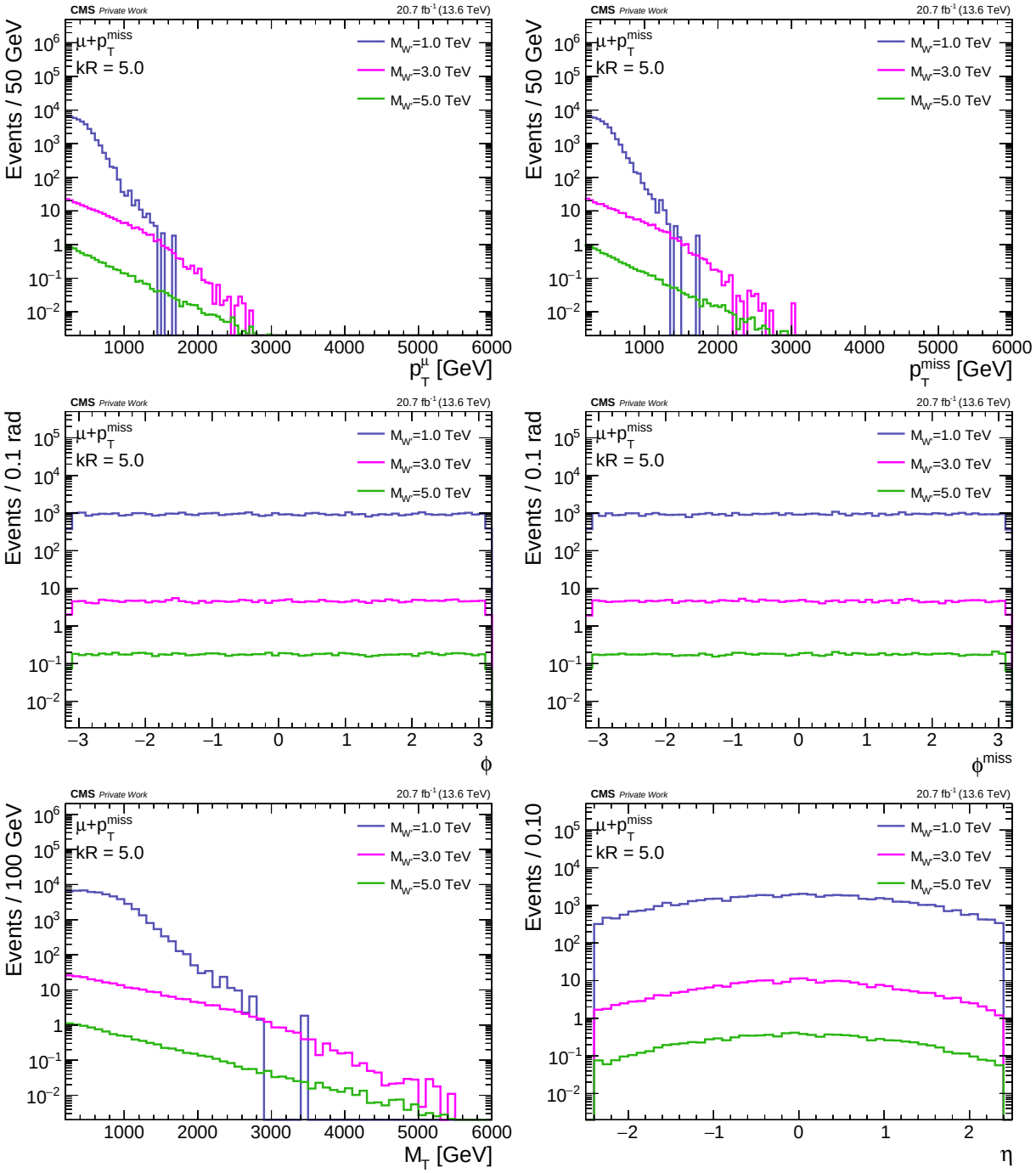

Figure B.9: Distributions for p_T (top left), p_T^{miss} (top right), ϕ (middle left), ϕ^{miss} (middle right), M_T (bottom left), and η (bottom right) at a coupling of 5.0 in the muon channel with 3 different W' signal sample masses (1000 GeV, 3000 GeV, and 5000 GeV).

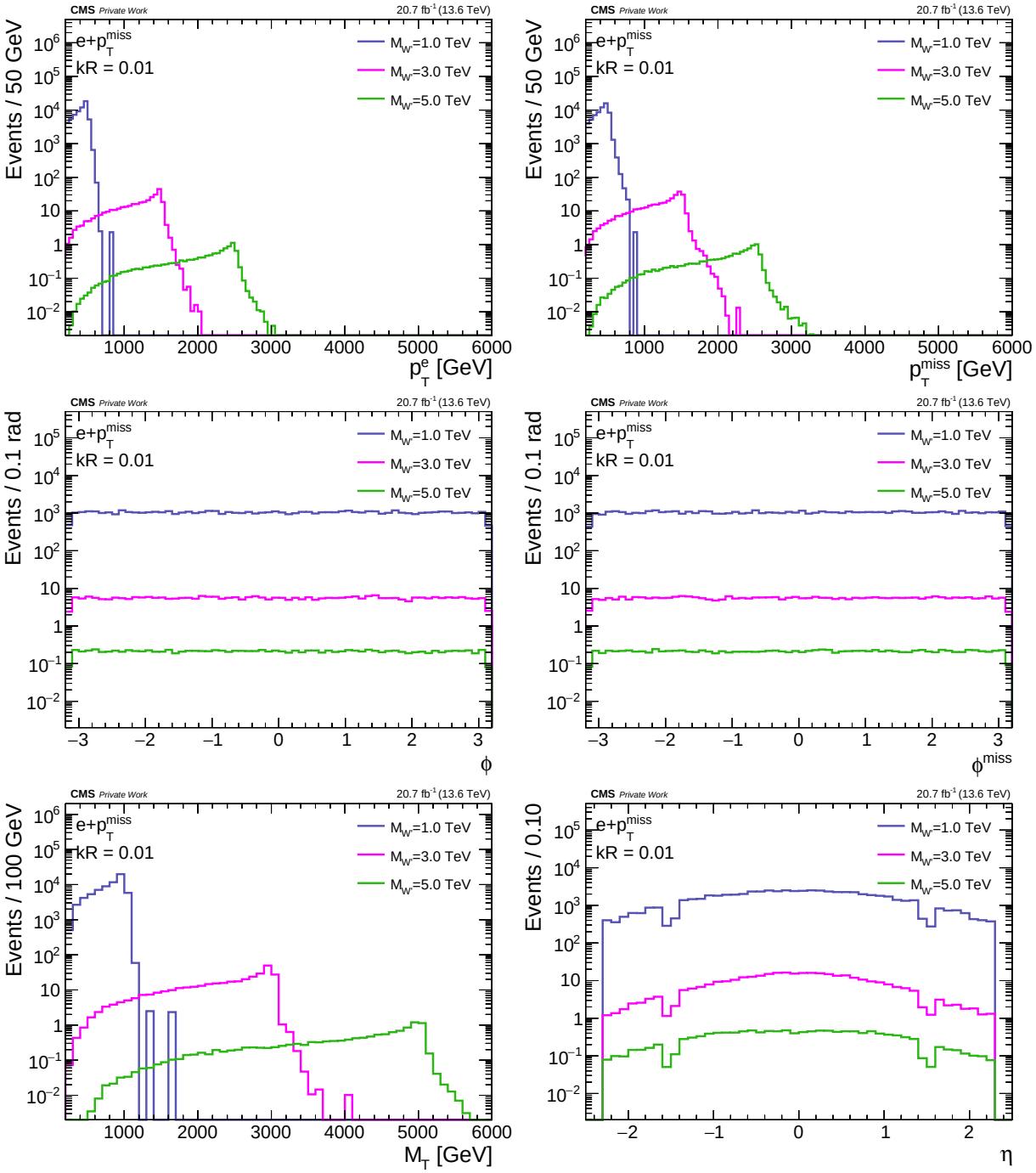

Figure B.10: Distributions for p_T (top left), p_T^{miss} (top right), ϕ (middle left), ϕ^{miss} (middle right), M_T (bottom left), and η (bottom right) at a coupling of 0.01 in the electron channel with 3 different W′ signal sample masses (1000 GeV, 3000 GeV, and 5000 GeV).

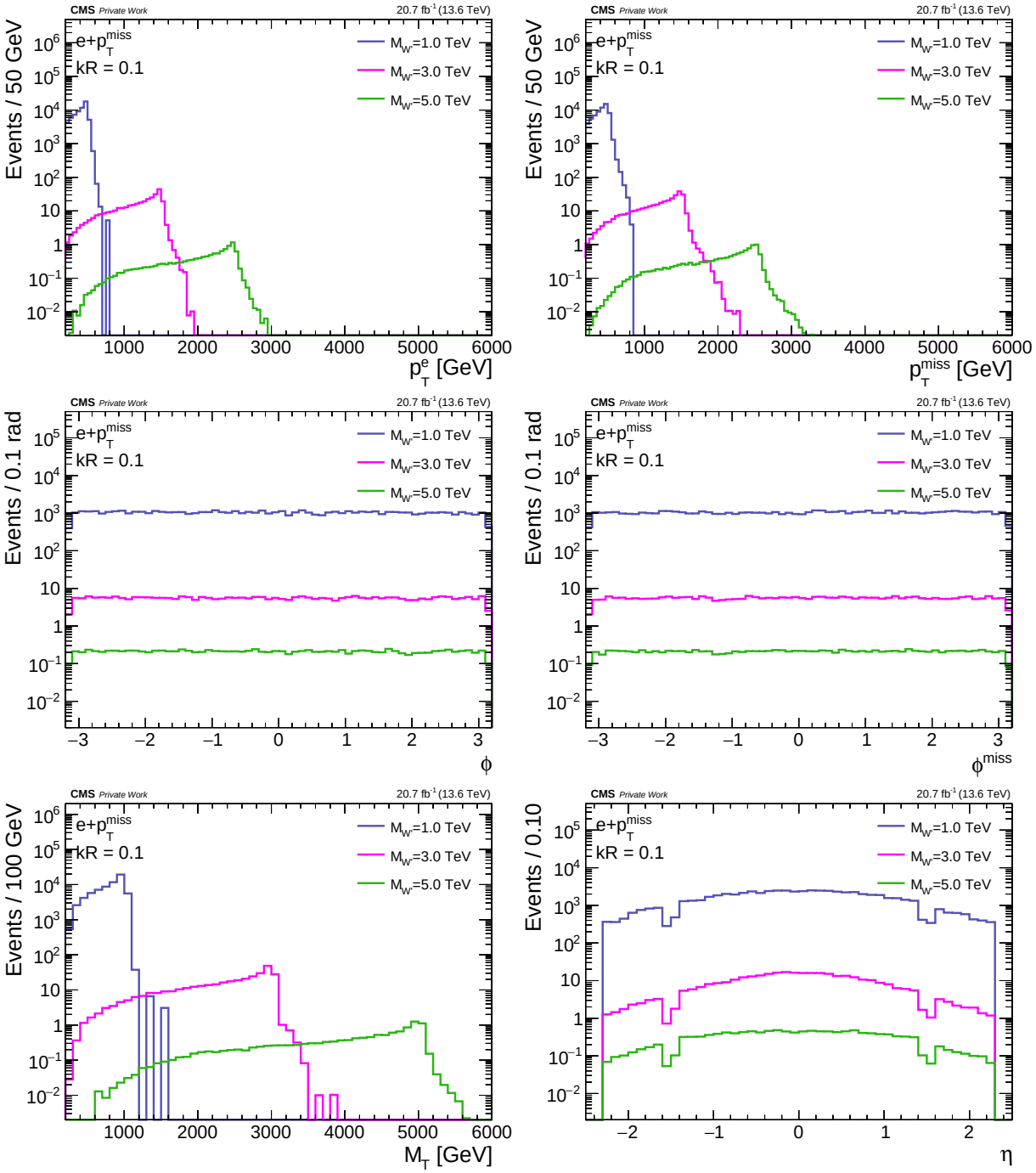

Figure B.11: Distributions for p_T (top left), p_T^{miss} (top right), ϕ (middle left), ϕ^{miss} (middle right), M_T (bottom left), and η (bottom right) at a coupling of 0.1 in the electron channel with 3 different W' signal sample masses (1000 GeV, 3000 GeV, and 5000 GeV).

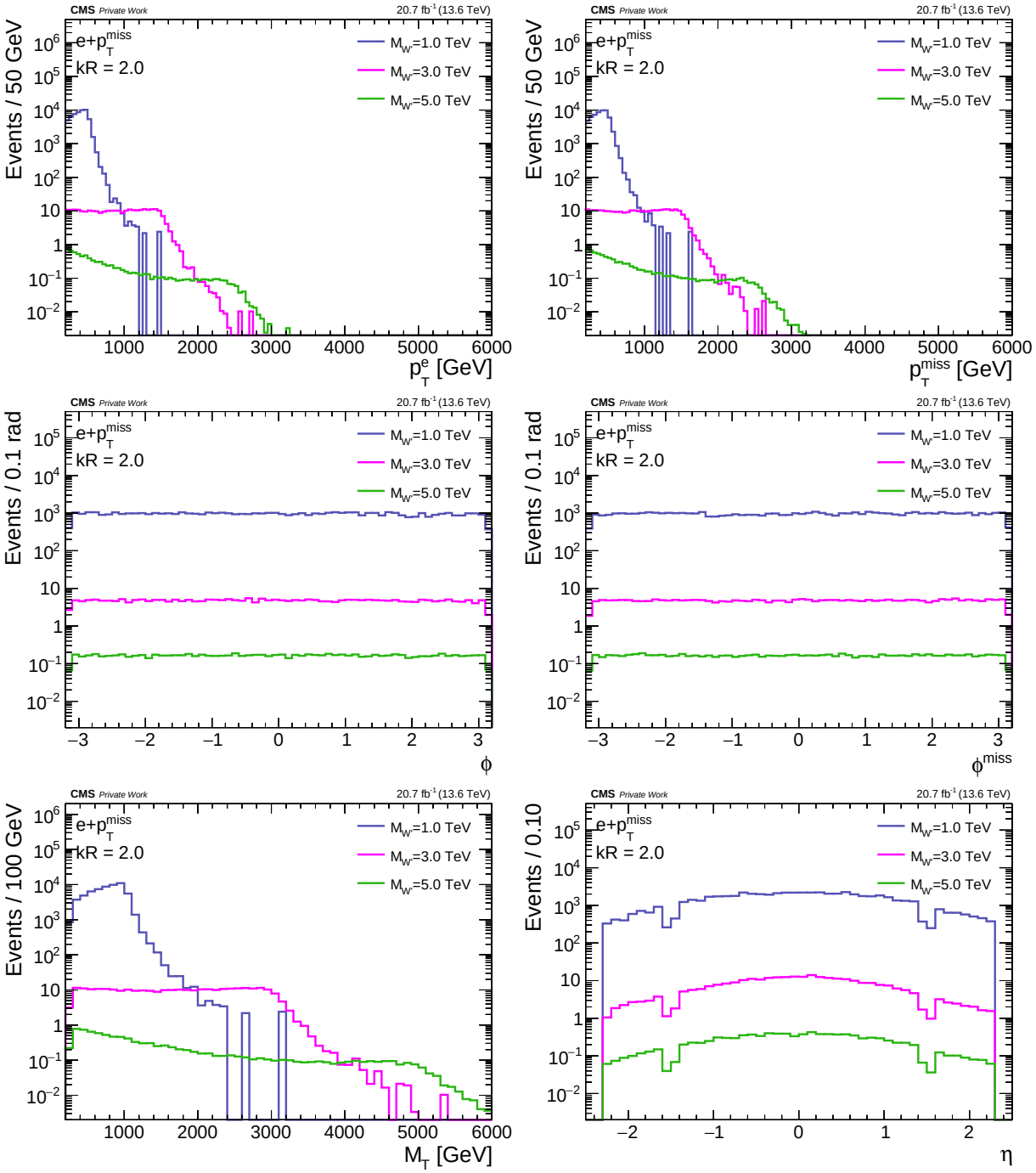

Figure B.12: Distributions for p_T (top left), p_T^{miss} (top right), ϕ (middle left), ϕ^{miss} (middle right), M_T (bottom left), and η (bottom right) at a coupling of 2.0 in the electron channel with 3 different W' signal sample masses (1000 GeV, 3000 GeV, and 5000 GeV).

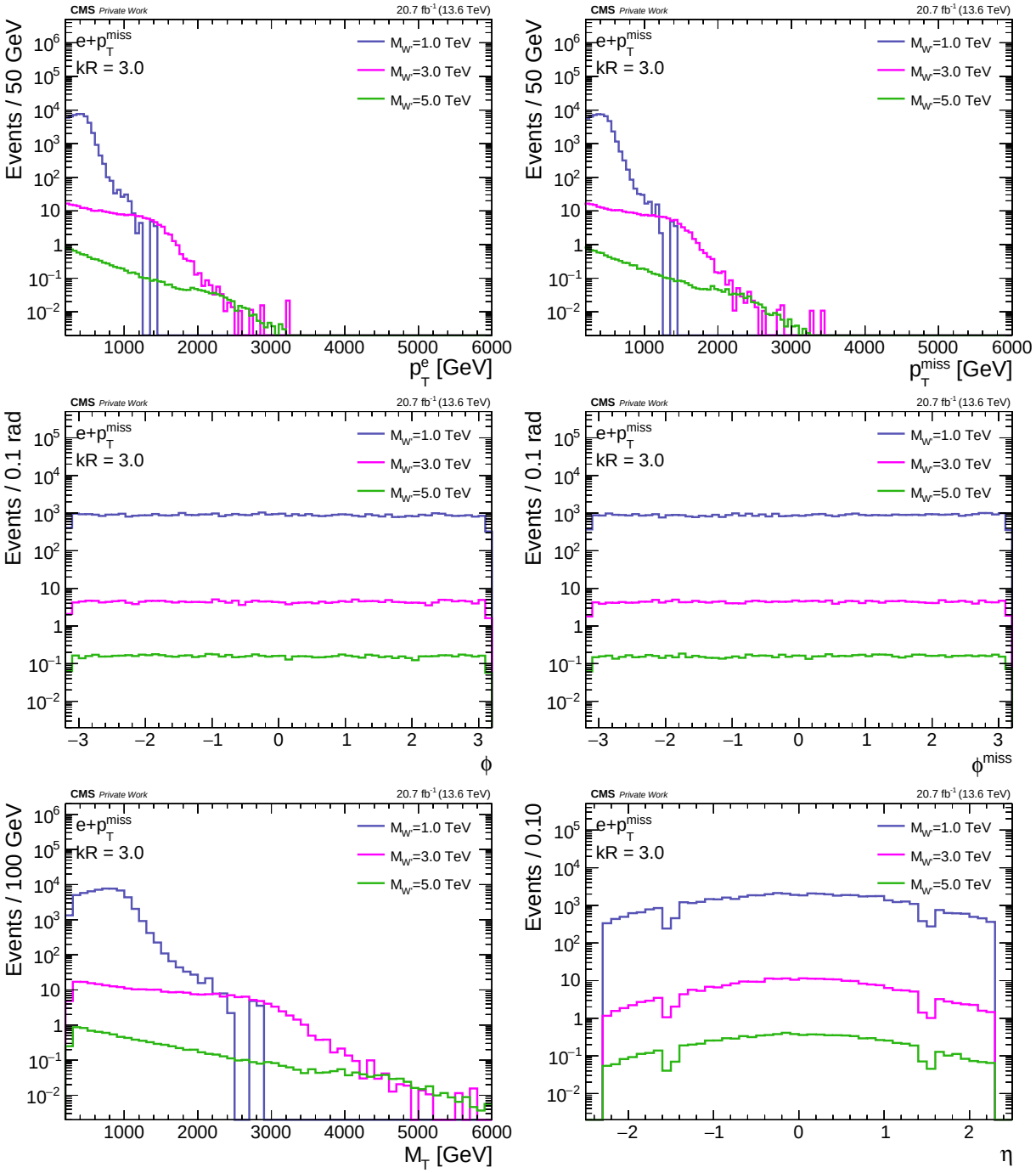

Figure B.13: Distributions for p_T (top left), p_T^{miss} (top right), ϕ (middle left), ϕ^{miss} (middle right), M_T (bottom left), and η (bottom right) at a coupling of 3.0 in the electron channel with 3 different W' signal sample masses (1000 GeV, 3000 GeV, and 5000 GeV).

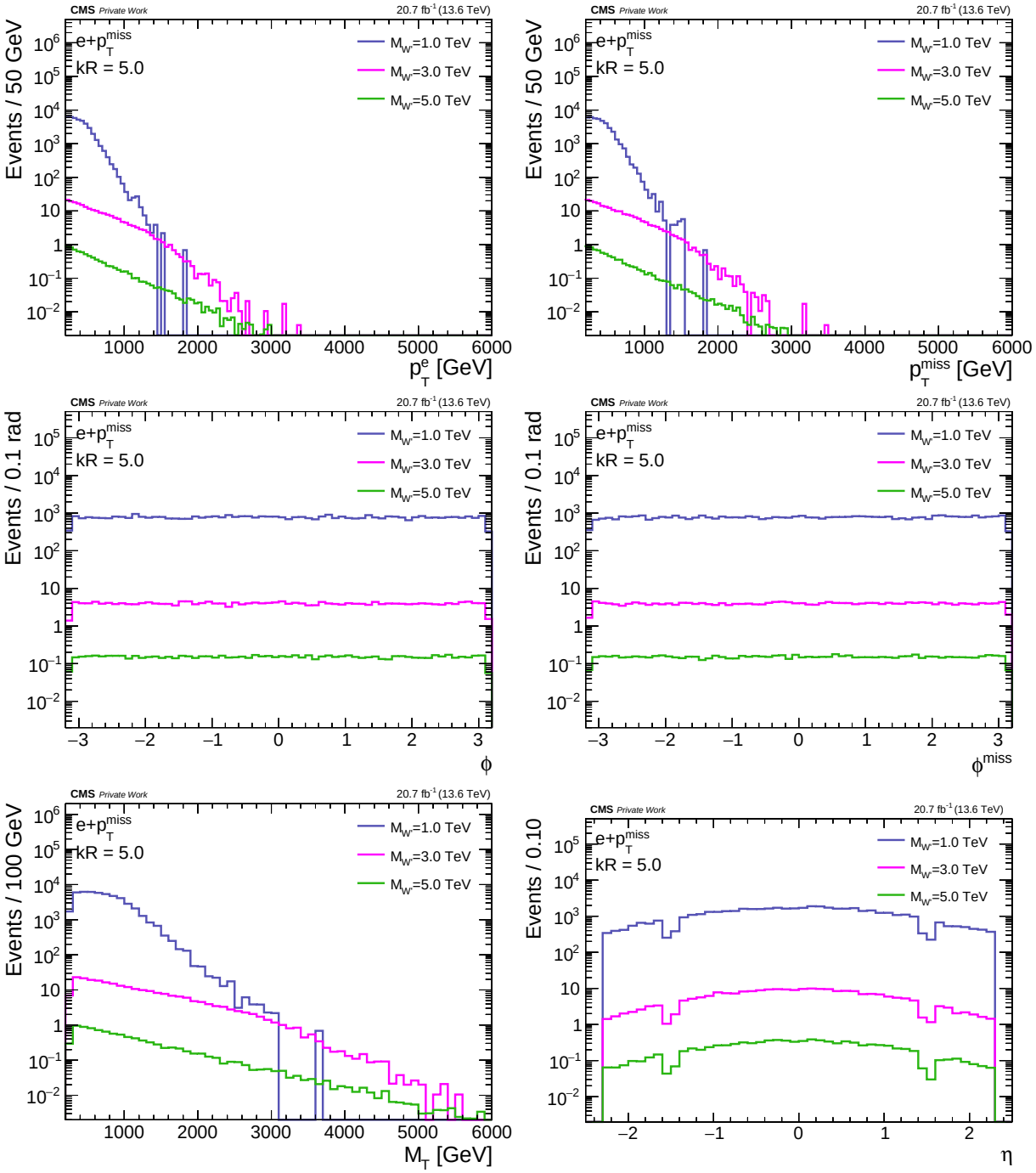

Figure B.14: Distributions for p_T (top left), p_T^{miss} (top right), ϕ (middle left), ϕ^{miss} (middle right), M_T (bottom left), and η (bottom right) at a coupling of 5.0 in the electron channel with 3 different W' signal sample masses (1000 GeV, 3000 GeV, and 5000 GeV).

Bibliography

[1] **Super-Kamiokande Collaboration** Collaboration, Y. e. a. Fukuda, "Evidence for oscillation of atmospheric neutrinos", *Phys. Rev. Lett.* **81** (Aug, 1998) 1562–1567. https://link.aps.org/doi/10.1103/PhysRevLett.81.1562.

[2] The CMS Collaboration, "TWiki>CMS Web>PhysicsPerfomanceDatasetHome>PdmV>PdmVRun3Analysis." https://twiki.cern.ch/twiki/bin/view/CMS/PdmVRun3Analysis. (accessed 25-September-2023).

[3] The CMS Collaboration, "Search for a heavy gauge boson w' in the final state with an electron and large missing transverse energy in pp collisions at sqrt(s) = 7 tev", *Physics Letters B* **698** no. 1, (Mar, 2011) 21–39. https://doi.org/10.1016%2Fj.physletb.2011.02.048.

[4] CMS Collaboration, "Search for physics beyond the standard model in final states with a lepton and missing transverse energy in proton proton collisions at sqrt(s) = 8 TeV", *arXiv e-prints* (Aug, 2014) arXiv:1408.2745, arXiv:1408.2745 [hep-ex].

[5] The CMS Collaboration, "Search for heavy gauge w' bosons in events with an energetic lepton and large missing transverse momentum at sqrt(s)=13 tev", *Physics Letters B* **770** (2017) 278–301. https://www.sciencedirect.com/science/article/pii/S0370269317303179.

[6] The CMS Collaboration, "Search for high-mass resonances in final states with a lepton and missing transverse momentum at sqrt(s) = 13 TeV", *Journal of High Energy Physics* **2018** no. 6, (Jun, 2018) . https://doi.org/10.1007%2Fjhep06%282018%29128.

[7] HandWiki, "Physics:Sequential Standard Model — HandWiki", 2022. https://handwiki.org/wiki/index.php?title=Physics:Sequential_Standard_Model&oldid=943578. (accessed 25-September-2023).

[8] Griffiths, D. J., *Elementary Particle Dynamics*, pp. 1–383. John Wiley & Sons, Ltd, 1987. https://onlinelibrary.wiley.com/doi/pdf/10.1002/9783527618460.ch2. https://onlinelibrary.wiley.com/doi/abs/10.1002/9783527618460.ch2.

[9] **Particle Data Group** Collaboration, R. L. Workman and Others, "Review of Particle Physics", *PTEP* **2022** (2022) 083C01.

[10] A. Einstein, "Die grundlage der allgemeinen relativitätstheorie", *Annalen der Physik* **354** no. 7, (1916) 769–822, https://onlinelibrary.wiley.com/doi/pdf/10.1002/andp.19163540702. https://onlinelibrary.wiley.com/doi/abs/10.1002/andp.19163540702.

[11] S. Chatrchyan et al., "Observation of a new boson at a mass of 125 gev with the cms experiment at the lhc", *Physics Letters B* **716** no. 1, (2012) 30–61. https://www.sciencedirect.com/science/article/pii/S0370269312008581.

[12] G. Altarelli, B. Mele, and M. Ruiz-Altaba, "Searching for new heavy vector bosons in $p\bar{p}$ colliders", *Zeitschrift für Physik C Particles and Fields* **47** no. 4, (1990) 676–676. https://doi.org/10.1007/BF01552335.

[13] M. Bargiotti et al., "Present knowledge of the Cabibbo-Kobayashi-Maskawa matrix", *La Rivista del Nuovo Cimento* **23** no. 3, (Mar, 2000) 1–71. https://doi.org/10.1007%2Fbf03548883.

[14] F. Landua, "The CERN accelerator complex layout in 2022. Complexe des accélérateurs du CERN en janvier 2022", 2022. https://cds.cern.ch/record/2813716. General Photo.

[15] The CMS Collaboration, "TWiki>CMSPublic Web>PhysicsResults>LumiPublicResults." https://twiki.cern.ch/twiki/bin/view/CMSPublic/LumiPublicResults. (accessed 25-September-2023).

[16] ATLAS Collaboration, "The atlas experiment at the cern large hadron collider: A description of the detector configuration for run 3", 2023.

[17] The CMS Collaboration, "Cms detector design." https://cms.cern/news/cms-detector-design. (accessed 25-September-2023).

[18] The CMS Collaboration, "The cms experiment at the cern lhc", *Journal of Instrumentation* **3** no. 08, (Aug, 2008) S08004. https://dx.doi.org/10.1088/1748-0221/3/08/S08004.

[19] **CMS** Collaboration, S. Morović, "Cms detector: Run 3 status and plans for phase-2", tech. rep., CERN LHC; CMS, 2023. arXiv:2309.02256. https://cds.cern.ch/record/2869746. DIS2023.

[20] CMS Collaboration, "Performance of the CMS level-1 trigger in proton-proton collisions at $\sqrt{s}$ = 13 TeV", *Journal of Instrumentation* **15** no. 10, (Oct, 2020) P10017–P10017. https://doi.org/10.1088%2F1748-0221%2F15%2F10%2Fp10017.

[21] **CMS** Collaboration, C. Collaboration], "Performance of Level-1 EGamma Trigger On 2022 pp Collisions at 13.6 TeV", (2023) . https://cds.cern.ch/record/2860208.

[22] **CMS** Collaboration, C. Collaboration], "Performances of Muons, Jets and MET Level 1 trigger algorithms in Run 3", (2023) . https://cds.cern.ch/record/2853675.

[23] CMS Collaboration, "Particle-flow reconstruction and global event description with the CMS detector", *Journal of Instrumentation* **12** no. 10, (Oct, 2017) P10003–P10003. https://doi.org/10.1088%2F1748-0221%2F12%2F10%2Fp10003.

[24] CMS Collaboration, "Performance of missing transverse momentum reconstruction in proton-proton collisions at $\sqrt{s}$ = 13 TeV using the CMS detector", *Journal of Instrumentation* **14** no. 07, (Jul, 2019) P07004–P07004. https://doi.org/10.1088%2F1748-0221%2F14%2F07%2Fp07004.

[25] The CMS Collaboration, "TWiki>CMSPublic Web>SWGuide>WorkBook>WorkBookPrintable>WorkBookTheWholeWorkBook>WorkBookChapter2." https://twiki.cern.ch/twiki/bin/view/CMSPublic/WorkBookChapter2. (accessed 25-September-2023).

[26] The CMS Collaboration, "TWiki>CMSPublic Web>SWGuide>WorkBook>WorkBookDataFormats." https://twiki.cern.ch/twiki/bin/view/CMSPublic/WorkBookDataFormats. (accessed 25-September-2023).

[27] Wunsch, Stefan, "Using cms open data for education, outreach and software development", *EPJ Web Conf.* **245** (2020) 08006. https://doi.org/10.1051/epjconf/202024508006.

[28] The CMS Collaboration, "TWiki>CMSPublic Web>SWGuide>WorkBook>WorkBookMiniAOD>WorkBookMiniAOD2017." https://twiki.cern.ch/twiki/bin/view/CMSPublic/WorkBookMiniAOD2017. (accessed 25-September-2023).

[29] The CMS Collaboration, "TWiki>CMSPublic Web>SWGuide>WorkBook>WorkBookNanoAOD." https://twiki.cern.ch/twiki/bin/view/CMSPublic/WorkBookNanoAOD. (accessed 25-September-2023).

[30] The CMS Collaboration, "TWiki>CMS Web>PhysicsPerfomanceDatasetHome>PdmV>PdmVRun3Analysis." https://twiki.cern.ch/twiki/bin/view/CMS/PdmVRun3Analysis#2022_Era_definition. (accessed 25-September-2023).

[31] The CMS Collaboration, "Problems and solutions: the ecal leak story." https://cms.cern/news/problems-and-solutions-ecal-leak-story. (accessed 25-September-2023).

[32] The CMS Collaboration, "Data Aggregation System (DAS)." https://cmsweb.cern.ch/das/. (accessed 25-September-2023).

[33] DQMDC Team, "Golden json files." https://cms-service-dqmdc.web.cern.ch/CAF/certification/Collisions22/Cert_Collisions2022_355100_362760_Golden.json. (accessed 25-September-2023).

[34] DQMDC Team, "TWiki>CMS Web>DQMDataCertification>DataCertification." https://twiki.cern.ch/twiki/bin/view/CMS/DataCertification. (accessed 25-September-2023).

[35] DQMDC Team, "TWiki>CMS Web>DQM." https://twiki.cern.ch/twiki/bin/view/CMS/DQM. (accessed 25-September-2023).

[36] S. Agostinelli et al., "Geant4—a simulation toolkit", *Nuclear Instruments and Methods in Physics Research Section A: Accelerators, Spectrometers, Detectors and Associated Equipment* **506** no. 3, (2003) 250–303. https://www.sciencedirect.com/science/article/pii/S0168900203013688.

[37] Torbjörn Sjöstrand et al., "An introduction to PYTHIA 8.2", *Computer Physics Communications* **191** (Jun, 2015) 159–177. https://doi.org/10.1016%2Fj.cpc.2015.01.024.

[38] R. Frederix and S. Frixione, "Merging meets matching in MC@NLO", *Journal of High Energy Physics* **2012** no. 12, (Dec, 2012) . https://doi.org/10.1007%2Fjhep12%282012%29061.

[39] S. Frixione, P. Nason, and C. Oleari, "Matching NLO QCD computations with parton shower simulations: the POWHEG method", *Journal of High Energy Physics* **2007** no. 11, (Nov, 2007) 070–070. https://doi.org/10.1088%2F1126-6708%2F2007%2F11%2F070.

[40] S. Alioli, P. Nason, C. Oleari, and E. Re, "A general framework for implementing NLO calculations in shower monte carlo programs: the POWHEG BOX", *Journal of High Energy Physics* **2010** no. 6, (Jun, 2010) . https://doi.org/10.1007%2Fjhep06%282010%29043.

[41] J. Alwall, M. Herquet, F. Maltoni, O. Mattelaer, and T. Stelzer, "MadGraph 5: going beyond", *Journal of High Energy Physics* **2011** no. 6, (Jun, 2011) . https://doi.org/10.1007%2Fjhep06%282011%29128.

[42] **CMS** Collaboration, S. et al., "Extraction and validation of a new set of CMS PYTHIA8 tunes from underlying-event measurements", *Eur. Phys. J. C* **80** no. 1, (2020) 4, arXiv:1903.12179. https://cds.cern.ch/record/2669320. All the figures and tables can be found atb http://cms-results.web.cern.ch/cms-results/public-result/publications/GEN-17-001 (CMS Public Pages).

[43] Richard D. Ball et al., "Parton distributions from high-precision collider data", *The European Physical Journal C* **77** no. 10, (Oct, 2017) . https://doi.org/10.1140%2Fepjc%2Fs10052-017-5199-5.

[44] W' group, "Cross sections of background samples." https://docs.google.com/spreadsheets/d/1hwdV74YrijKCRAGSFgKptHowoTl7hKuOhYuaFSDx8L0/edit. (accessed 25-September-2023).

[45] Richard D. Ball et al., "Parton distributions from high-precision collider data", *The European Physical Journal C* **77** no. 10, (Oct, 2017) . https://doi.org/10.1140%2Fepjc%2Fs10052-017-5199-5.

[46] The CMS Collaboration, "TWiki>CMS Web>EXOTICA>ExoticaNonResonant>ExoticaWprime>ExoticaWprime2022." https://twiki.cern.ch/twiki/bin/viewauth/CMS/ExoticaWprime2022. (accessed 25-September-2023).

[47] The CMS Collaboration, "TWiki>CMS Web>WebPreferences>FEWZ." https://twiki.cern.ch/twiki/bin/view/CMS/FEWZ. (accessed 25-September-2023).

[48] Coenen, Steffen, *Search for a new boson W' in the electron plus missing transverse momentum final state using 2017 CMS data at sqrt(s) = 13 TeV*. Bachelor thesis, RWTH Aachen, Aachen, 2018. https://web.physik.rwth-aachen.de/user/hebbeker/theses.html.

[49] Wprime groups, "Search for new physics in $l + pT^{miss}$ channel with the complete run-2 dataset." (accessed 25-September-2023, internal CMS Analysis Note).

[50] "Documentation for mc124Xrun3_NANO.root." https://cms-nanoaod-integration.web.cern.ch/integration/cms-swmaster/mc124Xrun3_doc.html. (accessed 25-September-2023).

[51] The CMS Collaboration, "TWiki>CMS Web>EgammaPOG>EgammaIDRecipesRun2>HEEPElectronIdentificationRun2." https://twiki.cern.ch/twiki/bin/view/CMS/HEEPElectronIdentificationRun2. (accessed 25-September-2023).

[52] Jeongeun Lee, "High-pt e/gamma trigger performance in run 3." https://indico.cern.ch/event/1312151/#6-high-pt-egamma-trigger-perfo. (accessed 25-September-2023).

[53] The CMS Collaboration, "TWiki>CMS Web>EgammaPOG>EgHLTRunIIISummary." https://twiki.cern.ch/twiki/bin/viewauth/CMS/EgHLTRunIIISummary. (accessed 25-September-2023).

[54] Wprime groups, "Search for new physics in l+met channel with 2016 data." (accessed 25-September-2023, internal CMS Analysis Note).

[55] BTV POG, "SF Campaigns." https://btv-wiki.docs.cern.ch/ScaleFactors/Run3Summer22EE/. (accessed 25-September-2023).

[56] The CMS Collaboration, "TWiki>CMSPublic Web>SWGuide>SWGuideTrackReco>SWGuideFinalTrackSelectors." https://twiki.cern.ch/twiki/bin/view/CMSPublic/SWGuideFinalTrackSelectors#5_X_X_values_for_selection_crite. (accessed 25-September-2023).

[57] The CMS Collaboration, "TWiki>CMS Web>MuonWikiHome>MuonPOG>SWGuideMuonIdRun2." https://twiki.cern.ch/twiki/bin/view/CMS/SWGuideMuonIdRun2#HighPt_Muon. (accessed 25-September-2023).

[58] Oscar Gonzalez Lopez, "High-pt muon trigger performance in 2023." https://indico.cern.ch/event/1312151/#5-high-pt-muon-trigger-perform. (accessed 25-September-2023).

[59] The CMS Collaboration, "TWiki>CMS Web>MuonWikiHome>MuonPOG>MuonRun32022." https://twiki.cern.ch/twiki/bin/viewauth/CMS/MuonRun32022. (accessed 25-September-2023).

[60] The CMS Collaboration, "TWiki>CMS Web>EXOTICA>ExoticaNonResonant>ExoticaWprime>ExoticaWprime2022>Run3Summer22MC." https://twiki.cern.ch/twiki/bin/view/CMS/Run3Summer22MC. (accessed 25-September-2023).

[61] Bongho Tae, "Run 3 W' Search." https://indico.cern.ch/event/1321849/#2-run-3-w-search. (accessed 25-September-2023).

[62] M. Olschewski, *Search for new physics in proton-proton collision events with a lepton and missing transverse energy*. Dissertation, RWTH Aachen, Aachen, 2016. https://publications.rwth-aachen.de/record/572409. Veröffentlicht auf dem Publikationsserver der RWTH Aachen University; Dissertation, RWTH Aachen, 2016.

[63] P. Schmüser, *Feynman-Graphen und Eichtheorien für Experimentalphysiker*. Lecture Notes in Physics. Springer Berlin Heidelberg, 1988. https://books.google.de/books?id=GfXvAAAAMAAJ.

[64] The CMS Collaboration, "TWiki>CMSPublic Web>SWGuide>WorkBook>WorkBookCMSSWFramework." https://twiki.cern.ch/twiki/bin/view/CMSPublic/WorkBookCMSSWFramework. (accessed 25-September-2023).

[65] Aachen 3A group, "Three a physics analysis software." https://gitlab.cern.ch/aachen-3a/tapas. (accessed 25-September-2023).

[66] I. Antcheva el al., "ROOT — A C++ framework for petabyte data storage, statistical analysis and visualization", *Computer Physics Communications* **180** no. 12, (Dec, 2009) 2499–2512. https://doi.org/10.1016%2Fj.cpc.2009.08.005.

[67] Valentina Sarkisovi, "W' search." https://indico.cern.ch/event/1299290/#3-w-search. (accessed 25-September-2023).

[68] The CMS Collaboration, "TWiki>CMS Web>TWikiLUM>LumiRecommendationsRun3." https://twiki.cern.ch/twiki/bin/viewauth/CMS/LumiRecommendationsRun3. (accessed 25-September-2023).

[69] Jet Energy Resolution and Corrections group, "Jet Energy Resolution and Corrections." https://cms-jerc.web.cern.ch/. (accessed 25-September-2023).

[70] The CMS Collaboration, "TWiki>CMS Web>WebPreferences>PhysicsResultsDP2022." https://twiki.cern.ch/twiki/bin/view/CMS/PhysicsResultsDP2022. (accessed 25-September-2023).

[71] The CMS Collaboration, "TWiki>CMS Web>JetMET." https://twiki.cern.ch/twiki/bin/view/CMS/JetMET#Run3_recommendations. (accessed 25-September-2023).

[72] The CMS collaboration, "Performance of CMS muon reconstruction in pp collision events at sqrt(s) = 7 TeV", *Journal of Instrumentation* **7** no. 10, (Oct, 2012) P10002–P10002. https://doi.org/10.1088%2F1748-0221%2F7%2F10%2Fp10002.

[73] The CMS collaboration, "Measurement of the inclusive w and z production cross sections in pp collisions at $ \sqrt {s} = 7 $ TeV with the CMS experiment", *Journal of High Energy Physics* **2011** no. 10, (Oct, 2011) . https://doi.org/10.1007%2Fjhep10%282011%29132.

[74] LUMI POG Group, "Hypernews: Recommended cross section for pile-up reweigthing." https://hypernews.cern.ch/HyperNews/CMS/get/luminosity/613/2/1/1/1.html. (accessed 25-September-2023).

Acknowledgement

Finally, I would like to take the opportunity and thank a few people here. First, and foremost, I would like to thank Prof. Dr. Thomas Hebbeker for allowing me to write my bachelor's thesis at the III. A Institute. I would also like to thank Dr. Kerstin Hoepfner. Without her intensive efforts, I would have not been able to gain this many insights into the work as a physicist and this thesis would have not been in this current form. Furthermore I would like to thank M.Sc. Valentina Sarkisovi, for being a mentor to me and always enduring my questions regarding the analysis framework when some part of the code again showed problems. Furthermore I would like to express my gratitude to Dr. Shawn Zaleski and M.Sc. Francesco Ivone for participating in proofreading this thesis. I would also like to thank Dr. Felipe Torres da Silva de Araujo and M.Sc. Fabian Nowotny for assisting with any physics or programming related topics.
Lastly, I would like to express my gratitude towards my mother, Yasemin Adıgüzel, and my girlfriend, Jessica Kustermann, for their patience and always supporting me in life. I have gained my endurance and strength thanks to them and I would have not been able to come this far without their role in my life.